INSTITUTO SUPERIOR TÉCNICO
Universidade Técnica de Lisboa

Solar Modulation effects on Cosmic Rays

Modelization with Force Field approximation, 1D and 2D numerical approaches and characterization with AMS-02 proton fluxes

Luís Miguel Mina Lopes Batalha

Dissertação para a obtenção do Grau de Mestre em

Engenharia Física Tecnológica

Júri

Presidente: Prof. Doutor Mário João Martins Pimenta
Orientador: Prof. Doutor Fernando José de Carvalho Barão
Vogal: Prof. Doutor Laurent Yves Marie Derôme

Julho 2012

To João, Vitor, Isabel and Catarina.

Resumo

O campo magnético do Sol, transportado pelo vento Solar, é a fonte da maior magnetosfera do Sistema Solar, a Heliosfera, e da consequente modulacão dos raios cósmicos galácticos. A modulação Solar é dominante a baixas energias (abaixo de 10 GeV), afectando não só a intensidade dos raios cósmicos galácticos como também a forma do seu espectro. Para cada espécie de raios cósmicos, o fluxo observado na Terra é deformado em relação ao fluxo interestelar, dependendo da actividade do Sol. A propagação dos raios cósmicos na Heliosfera é descrita pela *Equação de Parker*, formulada nos anos sessenta. A equação incorpora uma série de fenómenos físicos que acontecem no interior da Heliosfera, tais como processos difusivos, convecção, perdas de energia adiabáticas e drifts. Dado que não existe uma solução analítica completa para a *Equação de Parker*, foram tentadas várias abordagens para a resolver, desde aproximações analiticas até soluções numéricas. Na primeira parte deste trabalho, são estudadas as diferentes formas de resolver a equação de transporte e são delineados métodos para a resolução numérica a 1D e 2D. A segunda parte é a caracterização da modulação, usando os fluxos de protões medidos em AMS-02. O detector AMS foi instalado na ISS no ano passado e espera-se que consiga detectar fluxos de raios cósmicos até 1 TeV, de forma contínua durante 10 a 18 anos. A taxa de eventos que chega ao detector - 40 10^6 de eventos por dia - nunca tinha sido alcançada antes, representando assim uma oportunidade única de estudar, numa base diária, a modulação Solar. Finalmente, para alguns dos resultados, é feita uma comparação entre AMS-02 e os monitores de neutrões.

Palavras-Chave: Modulação Solar, AMS-02, Aproximação Force FIeld, Solução 1D, Solução 2D, fluxos de protões.

Abstract

The magnetic field of the Sun, embedded in the Solar Wind, is the source of the biggest of the Solar System magnetospheres, the heliosphere, and of the observed modulation of the galactic cosmic rays. Solar modulation is dominant on low energy particles (below 10 GeV), and affects not only the galactic cosmic ray intensities, but even their spectral shape. For each cosmic ray species, the particle fluxes measured at Earth are deformed with respect to the local interstellar ones, depending on the Solar activity. The propagation of cosmic rays in the heliosphere is described by the so called *Parker Equation*, formulated in the sixties. The equation takes into account several phenomena happening inside the Heliosphere, such as diffusion, convection, adiabatic energy changes and drifts. Since there is no full analytical solution to the *Parker Equation*, several different approaches have been tried, from numerical solutions to analytical approximations. In the first part of this work, the different ways of solving the transport equation are studied and numerical methods (1D and 2D) are outlined. The second part is the characterization of the modulation, using the AMS-02 proton fluxes. The AMS detector was installed last year in the ISS and is expected to gather data from cosmic ray fluxes up to 1 TeV, continuously between 10 to 18 years. The rates of events reaching the detector - 40 10^6 events per day - have never been achieved before, and represent an unique opportunity to systematically study the Solar modulation in a daily basis. Finally, for certain results, a comparison is done between the AMS-02 and the Neutron Monitors.

Keywords: Solar Modulation, AMS-02, Force Field approximation, 1D solution, 2D solution, proton fluxes.

CONTENTS

List of Figures

LIST OF TABLES

ACRONYMS

ACC Anticoincidence Counters.

ACR Anomalous Cosmic Rays.

ADI Alternating Direction Implicit.

AMICA Astro Mapper for Instrument Check of Attitude.

AMS Alpha Magnetic Spectrometer.

CME Coronal Mass Ejections.

CN Cranck Nicholson.

CRs Cosmic Rays.

ECAL Electromagnetic Calorimeter.

GCR Galactic Cosmic Rays.

HCS Heliospheric Current Sheet.

HMF Heliospheric Magnetic Field.

IGRF International Geomagnetic Reference Field.

ISM Interstellar Medium.

ISS International Space Station.

LBM Leaky Box Model.

LIP Laboratório de Instrumentação e Física de Partículas.

LIS Local Interstellar Flux.

MCDM Monte Carlo Diffusion Model.

MDR Maximum Detectable Rigidity.

MHD Magnetohydrodynamic.

NM Neutron Monitors.

PDE Partial Differential Equation.
PMT Photomultipliers.

QLT Quasi-Linear Theory.

RICH Ring Imaging Cerenkov.

SAA South Atlantic Anomaly.
SCR Solar Cosmic Rays.
SEP Solar Energetic Particles.
SIDC Solar Influences Data Analysis Center.
SN Super Nova.
SNe SuperNovae.

TOF Time-of-Flight.
TPE Transport Equation.
TRD Transition Radiation Detector.
TS Termination Shock.

1

INTRODUCTION

Robert Milikan was the first human being to use the term "cosmic rays" in 1925, to describe the flux of particles coming from "the outer cosmos", capable of ionizing the air in Earth's atmosphere.

However, even the birth of the name "cosmic ray" is not a matter of chance, since it is preceded by almost 30 years of questions, research and peculiar experiments.

The story began after the discovery of radioactivity by Henri Bacquerel in 1896, when it was believed that the ionization of the air was due to radiation from radioactive elements in the ground.

The method to test the veracity of the last statement is simple: to measure the ionization of the air at various heights.

The ionization was measured in towers, including the Eiffel Tower, in attempts to figure out what was the penetration power of the radiation coming from the ground. Nevertheless, it was only in 1912, exactly 100 years ago, that Victor Hess flew in a balloon to altitudes of 5 km and discovered that , instead of decreasing, the ionization of the air, strongly increases with altitude. Hess wrote in his book,

> *"a radiation of very high penetrating power enters the atmosphere from above"*

This marked the discovery of Cosmic Rays (CRs) for which Hess received the Nobel prize in 1936.

During the following twenty to thirty years, cosmic ray research concentrated on the high energy properties of the cosmic radiation. CRs were the predecessors of the accelerators as the source of high energy particles. Physicists began to study the curved tracks, produced by cosmic rays in cloud chambers, and new discoveries were made.

In August 1932, Anderson observed particles, identical to electrons, that were curving in the opposite direction in the cloud chamber. These particles were positrons, and represented the first experimental signature of antimatter.

During the golden age of particle accelerators, in the mid twentieth century, there was a mass exodus of CRs's scientists to the accelerator labs.

At the same time there was a significant advance of the field in different directions, mainly in the area now called "Space Physics". The subject was devoted to the study of the Solar System, the magnetic fields in the Heliosphere or the constitution and properties of the Solar Wind. The modulation of CRs when crossing the zone of influence of the Sun - the Heliosphere - became a major field of research.

All these research topics were helped by the space programs of the 60's and the 70's. Satellites were being sent to space at an increasingly high rate, and for the first time in history it was possible to measure CRs's intensities in space and compare them with the intensities measured at Earth, for different Solar cycle epochs and different levels of Solar activity.

With experiments mounted on balloons and satellites it was possible to measure the chemical and isotopic compositions of CRs with higher precision, since the particles were detected before entering the atmosphere.

Figure 1.1: Lunar Module Pilot Edwin 'Buzz' Aldrin unfurls the Swiss Solar Wind Composition Experiment - the only European experiment taken to the Moon by Apollo -, and the first "flag" on the moon.

In the last years, scientists became interested in studying the nature of the highest energy CRs. While in particle accelerators, like the LHC, laboratory energies of 10^8 GeV are being achieved, the big CRs detectors at the ground are measuring particles with energy exceeding 10^{11} GeV. How does Nature accelerate particles to such high energies is one of the big questions, still to be answered.

Cosmic Ray physics is a multidisciplinary field where almost every discovery is made on the edge of different subjects, from Particle Physics to Astronomy, or Astrophysics.

The main purpose of this thesis is to study the effects of the Sun on the flux of galactic cosmic rays. The Solar modulation effects are dominant at low energies (below ~ 10 GeV), and are responsible for the little "bump" on the low energy portion of the cosmic ray spectrum. In order to quantify the effects of the Sun on the galactic fluxes, Parker developed a transport equation in 1964. This equation takes into account several physical phenomena occurring inside the Heliosphere and can only be solved numerically. In the first part of this thesis some approaches of solving the equation will be derived. The second part is devoted to the characterization of the modulation using the data from the AMS-02 spectrometer.

2

COSMIC RAY PHYSICS

2.1 The Spectrum of Cosmic Rays

The Cosmic Ray Spectrum, i.e. the mean number of Cosmic particles, per surface unit, per time unit, per solid angle unit and per energy unit that reach Earth has a couple of unique features. One of the first things that can be noticed in 2.1(a) is that the spectrum has a large extension, not only in energy, covering 12 orders of magnitude, but also in the particle fluxes, sweeping through 10 orders of magnitude.

This enormous variety has a few consequences. The first one is that the detectors used to study the spectrum at 1 GeV are satellites, like the AMS-02, while the detectors used to study particles at 10^{12} GeV are huge surface detectors, as big as 1.2 times the size of Luxembourg, like the Pierre Auger Observatory. The second one is the fact that it gives us the opportunity to explore completely different aspects of astrophysics and particle physics.

The spectrum can be described by a power-law in almost all energies

$$J(E) = \frac{dN}{dE} \propto E^{-\gamma} \tag{2.1}$$

However, the spectral index changes with energy, taking the following approximate values:

- 2.7 below 4×10^{15} eV
- 3.0 between 4×10^{15} eV and 5×10^{18} eV
- 2.8 for energies higher than 5×10^{18} eV

The only energy region where the spectrum is not described by a power-law is the low energy region, around 1 GeV, due to Solar Modulation. The way the Sun models the flux is the main topic of this thesis and will be extensively discussed in the next sections. In 2.1(b) the effect of the Sun and its activity on the proton fluxes are clearly visible.

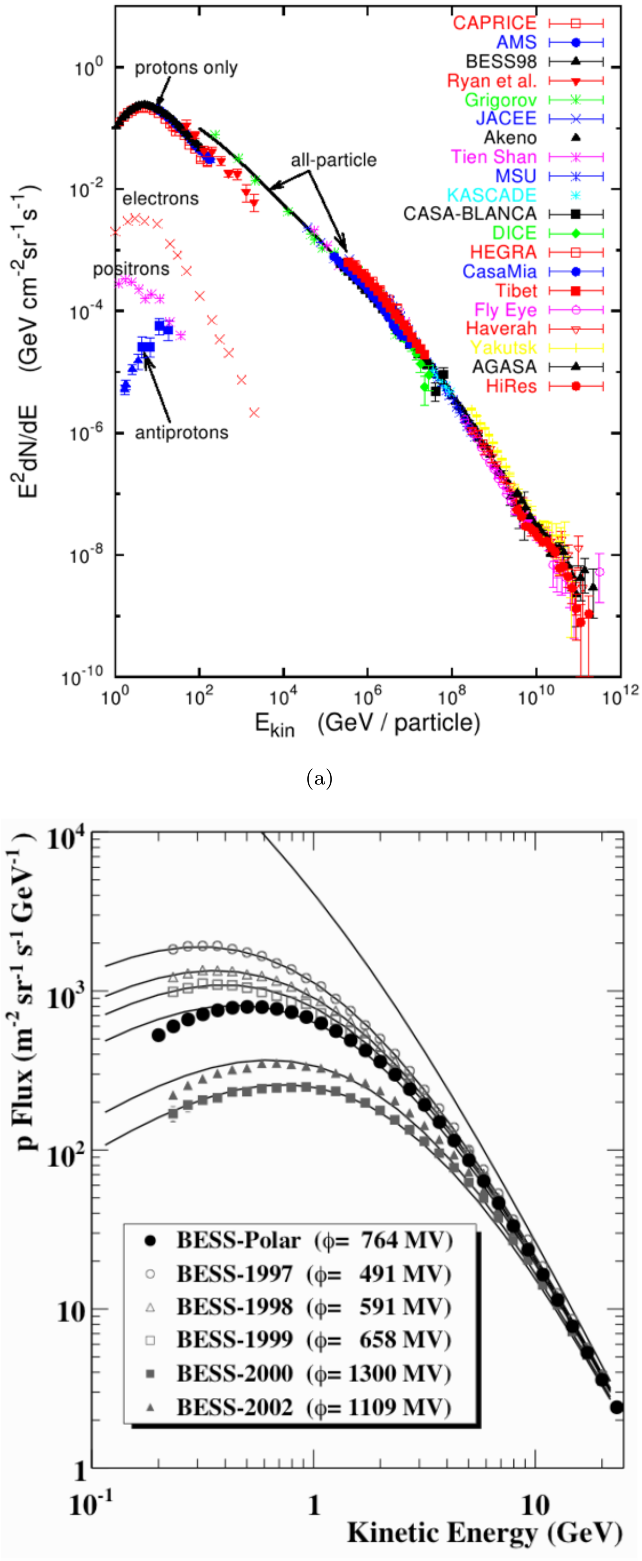

(a)

(b)

Figure 2.1: a) Differential all-particle spectrum of cosmic rays. [1]. b) Effects of solar modulation on the proton fluxes (BESS) [2]

2.2 Chemical Composition and Classification

For energies below 100 TeV the cosmic ray composition is the following

Table 2.1: Cosmic rays' composition

Type of particle	Relative abundance
Protons	86%
Helium	11%
Electrons	2%
Heavier nuclei	1%
Positrons	1%
Antiprotons	1%

It is a curious exercise to take the relative abundance of CRs, depending on the chemical element, and compare it with the abundance of those elements in the Solar System. As can be seen in 2.2, the two curves have a very similar behavior, having peaks in C,N,O and Fe, and in both cases Z-even nuclei are more abundant than Z-odd (because nuclei with Z-even have a larger binding energy). The only difference is on the abundance of elements like Li, Be and B, which are far more abundant in CRs. This is due to the fact that these elements are a product of nuclear interactions between CRs and the Interstellar Medium (ISM), which occur during the propagation through the Galaxy. If the spallation cross sections are known, a measure of secondary/primary abundances can give an indication about the amount of transversed matter. Thus, secondary to primary ratios are sensitive to the propagation in the Galaxy and their measure is widely used in models, so that the propagation parameters can be constrained, reducing the theoretical uncertainties.

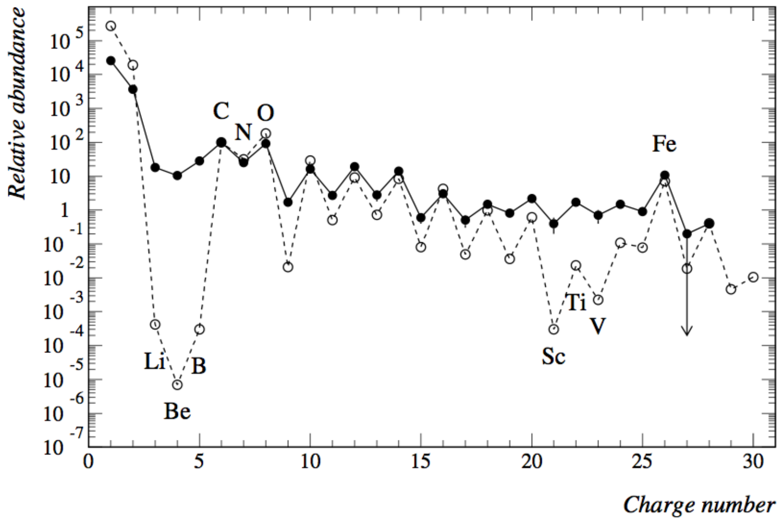

Figure 2.2: Chemical composition of cosmic radiation as measured at 1AU from the Sun compared to the abundances in the Solar System for elements with Z=1-30.Relative abundances are normalized to the Carbon abundance [3].

CRs are classified as *primary*, those that are accelerated at the source, and *secondary*, those that are produced in interactions between primaries and the interstellar gas. Unfortunately, the designations primary and secondary are also used with a different meaning in the context of atmospheric interactions of CRs, where a *primary* is a particle that comes from the outer space, and a *secondary* is a particle that was formed due to the interactions of the *primary* with the atmosphere.

Normally, it is possible to separate CRs in three groups:

1. Galactic Cosmic Rays (GCR), originated from outside the solar system are mainly constituted by protons (7% to 10%), Helium (1%) and heavier elements. The source of the very high energy GCR is not clearly known. The flux of GCR measured at Earth is highly influenced by Sun's activity.

2. Solar Cosmic Rays (SCR) or **Solar Energetic Particles (SEP)** can be created by a Solar flare, a Coronal Mass Ejections (CME) or shocks in the interplanetary medium. SCR energies range from several hundred MeV/nucleon to some GeV/nucleon, and the composition is very similar to GCR's. During a few hours/days after a Solar flare, the intensity of cosmic rays that reach Earth can increase because of the SCR - this is usually called a SEP.

3. Anomalous Cosmic Rays (ACR) arise from interstellar atoms, which are caught by the motion of the Sun in the ISM, and stay inside the heliosphere, where the magnetic field of the Sun dominates. After that, the atoms are ionized at 1-3 AU, either by photoionization by solar UV photons or by collisions with Solar Wind protons. The recently created charged particles, now sensible to the Heliospheric Magnetic Field (HMF), are carried towards the termination shock (during this trip the ions are called pickup ions), where they are accelerated (First-order Fermi acceleration) from Solar Wind energies, of about 1 KeV/nucleon, to tens of MeV/nucleon. The acceleration continues until they have enough energy to escape the shock (some of them diffuse into the inner heliosphere).

2.3 Sources

As mentioned in the last section, the Sun is a source of low-energy CRs, and so it is quite reasonable to think that all the other Sun-like stars in the universe are also a possible source of CRs. However, after calculating the production rate of CRs by Sun-like stars, the obtained numbers are too low to explain the observed GCR intensities. As a consequence, several theories have been proposed to explain the observed fluxes.

One of the proposed sources were SuperNovae (SNe). The principal requirement that a given kind of object must obey in order to be considered a source of CRs is that the total power emitted must be enough to supply the actual cosmic ray density ($\rho \simeq 1.6$ eV/cm^3).

Calculating the volume of the galactic disk as

$$V_D = \pi R^2 d \simeq 4 \times 10^{66} cm^3 \tag{2.2}$$

where $R = 15 \times 10^3$ pc is the galactic radius and $d = 200$ pc is the galactic height.

Now, using the confinement time of a cosmic ray in the galactic disk calculated within the Leaky Box Model (LBM) - $\tau \simeq 6 \times 10^6$ years -, it is easy to estimate the required power of the source

$$P = \frac{\rho V_D}{\tau} \simeq 8 \times 10^{40} erg/s \tag{2.3}$$

Knowing the average energy realesed by a Super Nova (SN) explosion - $E \simeq 1.6 \times 10^{51}$ erg - and the rate of these kind of events in the galaxy - 3 per century - the total power emited by SN explosions is

$$P_{SN} \simeq 3 \times 10^{42} erg/s \tag{2.4}$$

which makes a SN a strong candidate to be a source of GCR [4].

Another point in favor of this hypothesis came in 1970 when it was understood that the type of shock occurring in a SN explosion was adequate to explain the acceleration method required to reproduce a power-law spectra.

Recently, a new hypothesis suggested by Zatsepin and Sokolskaya [5] says that in order to fit the experimental data on proton, helium and other nuclei, there must be three types of sources, each one with a characteristic spectral index and maximum acceleration energy.

The three sources are:

- Stars with mass ranging from 8 to 15 $M_\odot$, that exploded into the ISM;
- Stars with mass greater than 15 $M_\odot$ within their own stellar wind;
- Nova stars that in the explosion produce an expanding shell like a SN;

The first two types of sources are enough to account for the proton and helium spectra above 300 GeV, while the third one is required to reproduce fluxes below 300 GeV.

2.4 Acceleration

In what concerns acceleration of CRs, there is a fairly good knowledge of the mechanisms responsible for the acceleration of particles below 1 TeV, during the propagation. The two processes are named first-order and second-order acceleration.

2.4.1 Second-order Fermi acceleration

This mechanism was proposed by Enrico Fermi in 1949 [6]. In his original paper, Fermi suggests that the source of acceleration of particles are slowly moving magnetic clouds, with density 10 to 100 times higher than the average ISM density and an enhanced "frozen in" magnetic field. If these magnetic clouds were stationary, the particles would just invert its motion, without any energy changes, just like a magnetic trap. However, if the clouds were moving, the particles would lose or gain energy depending on the direction of the cloud.

For a better understanding of the underlying phenomena, let us consider a relativistic particle, with energy E_1, entering a slowly moving magnetic cloud (head-on collision).

In the cloud's reference frame, the energy is calculated using a Lorentz transformation

$$\begin{pmatrix} E_1'/c \\ \vec{p'} \end{pmatrix} = \Lambda \begin{pmatrix} E_1/c \\ \vec{p} \end{pmatrix} \tag{2.5}$$

$$E_1' = \gamma E_1 (1 - \beta \cos\theta_1) \tag{2.6}$$

where θ_1 is is the angle between the moving directions of the particle and the cloud, $\beta = \frac{V}{c}$ and $\gamma = \frac{1}{\sqrt{1-\beta^2}}$ are related to the cloud. Defining E_2' and θ_2' as the energy and angle of the exiting particle in the cloud's frame, it is now possible to apply another Lorentz transformation in order to obtain

$$E_2 = \gamma E_2' (1 + \beta \cos\theta_2') \tag{2.7}$$

Assuming the hypothesis of elastic scattering - $E_2' = E_1'$ (the total energy of the particle is conserved in the frame of the cloud)

$$E_2 = \gamma^2 E_1 (1 - \beta\cos\theta_1)(1 + \beta\cos\theta_2') \tag{2.8}$$

$$\frac{E_2 - E_1}{E_1} \simeq \frac{\Delta E}{E} = \frac{1 + \beta(\cos\theta_2' - \cos\theta_1) - \beta^2 \cos\theta_2' \cos\theta_1}{1 - \beta^2} - 1 \tag{2.9}$$

Now averaging the equation with respect to the two angles θ_1 and θ_2'

$$\left\langle \frac{\Delta E}{E} \right\rangle := \int_{-1}^{1}\int_{-1}^{1} \frac{\Delta E}{E} f_{\theta_1} f_{\theta_2'} d\cos\theta_1 d\cos\theta_2' \tag{2.10}$$

where f_θ the Probability Density Function (PDF) for the angle θ.

Since the particle is scattered many times inside the cloud, its leaving direction is randomized and $\langle\cos\theta_2'\rangle = 0$. The probability of a collision at an angle θ_1 is proportional to the relative velocity between the cloud and the particle $v - V\cos\theta_1$, and so $f_{\theta_1} \propto (v - V\cos\theta_1)$. In the case of a relativistic particle with $v \simeq c$ the probability is proportional to $1 + \left(\frac{V}{c}\right)\cos\theta$. From the last relation, it is possible to deduce that the probability of head-on encounters, $p \propto 1 + \left(\frac{V}{c}\right)\cos\theta_1$ is slightly greater than the probability of following collisions, $p \propto 1 - \left(\frac{V}{c}\right)\cos\theta_1$.

$$\langle\cos\theta_1\rangle = \frac{\int_{-1}^{1}\cos\theta_1 f_{\theta_1}\, d\cos\theta_1}{\int_{-1}^{1} f_{\theta_1}\, d\cos\theta_1} = \frac{\int_{-1}^{1}(x-\beta x^2)dx}{\int_{-1}^{1}(1-\beta x)dx} = -\frac{\beta}{3} \tag{2.11}$$

Substituting the mean value in expression 2.10 and expanding the result ($\beta \ll 1$)

$$\left\langle\frac{\Delta E}{E}\right\rangle = \frac{1+\beta^2/3}{1-\beta^2} - 1 \simeq \frac{4}{3}\beta^2 \tag{2.12}$$

Since the frontal collision is more probable, the final effect for the particles interacting with the cloud is a gain in energy.

2.4.2 First-order Fermi acceleration

As showed independently by Bell (1978) [7] and by Blandford and Ostriker (1978) [8] , a charged particle can be efficiently accelerated by a SN remnant shock.

Let us assume a shock front that moves in the interstellar medium with velocity $-u_1$. As the shock wave travels through the medium all the shocked gas will flow in the opposite direction with velocity u_2 relative to the front ($|u_1| > |u_2|$).

Considering that the gas and shock front velocities are low, the velocity of the shocked gas in the laboratory frame is just the difference between u_2 and u_1: $V = -u_1 + u_2$. From now on, the procedure is exactly identical to the one applied in second-order acceleration. In other words, the formula 2.10 remains valid but V is now the velocity of the shocked gas (downstream) relative to the unshocked gas (upstream). The only difference is in the way the average over θ is done, since the shock front is now planar.

The probability that a particle arriving with an angle θ_1 ($-1 < \cos\theta_1 < 0$) crosses the shock front is proportional to $\cos\theta_1$, since the shock is planar.

Normalizing the probability distribution

$$\int_{-1}^{0} A\cos\theta_1\, d\cos\theta_1 = 1 \Leftrightarrow A = 2 \tag{2.13}$$

$$f_{\theta_1} = 2\cos\theta_1 \tag{2.14}$$

Similarly,

$$f_{\theta_2} = 2\cos\theta_2 \tag{2.15}$$

And so,

$$\langle\cos\theta_1\rangle = \int_{-1}^{0} 2\cos^2\theta_1\, d\cos\theta_1 = -2/3 \tag{2.16}$$

$$\langle\cos\theta_2\rangle = \int_{0}^{1} 2\cos^2\theta_2\, d\cos\theta_2 = 2/3 \tag{2.17}$$

$$\left\langle\frac{\Delta E}{E}\right\rangle = \frac{1+\frac{4}{3}\beta+\frac{4}{9}\beta^2}{1-\beta^2} - 1 \simeq \frac{4}{3}\beta \tag{2.18}$$

As $\beta \ll 1$, the first-order Fermi acceleration is more effective than the second-order. After crossing the shock front, the particle is repeatedly scattered by magnetic field irregularities ahead of the shock, increasing its energy. This mechanism explains the SCR and ACR acceleration.

2.5 The Heliospheric Environment

2.5.1 Sun's Magnetic Field

The Sun lies in the spiral arm of our Galaxy, located at a distance of approximately 8.5 kpc from its center, and about 1 AU from the Earth. As many other stars the Sun has in its interior flowing electric currents. These currents, combined with an high conductivity, form what is called a Magnetohydrodynamic (MHD) dynamo, which is responsible for creating the Sun's magnetic field. The system is self-exciting since the rotation of the Sun enhances the magnetic field.

The field flips its polarity every 11 years, returning to its original configuration every 22 years. The 11 years periodicity is usually referred to as the *Solar Activity Cycle.*The details of the mechanism are still very controversial, but it is well established that the sunspot number and the 11 years sunspot periodicity are a direct manifestation of the ropes of the magnetic field lines emerging onto the Sun's photosphere.

The Sun doesn't rotate as a rigid body, it possesses a differential rotation, which means that the equator rotates faster than the poles. The consequence is that the Sun's overall magnetic field becomes distorted and twisted over time. The twisted field lines eventually come through the photosphere, showing their presence as *sunspots* (as depicted in figures 2.3 and 2.4).

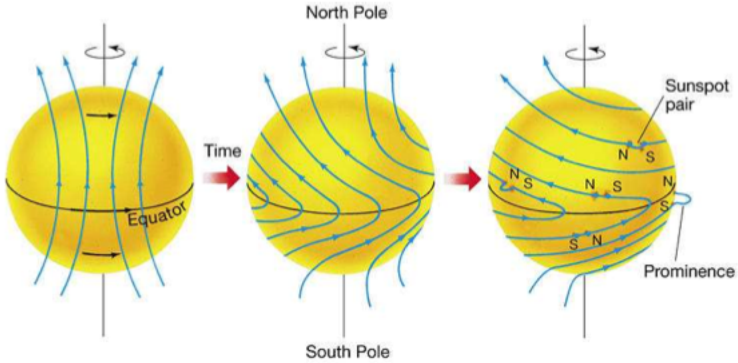

Copyright © 2005 Pearson Prentice Hall, Inc.

Figure 2.3: Sunspot formation.

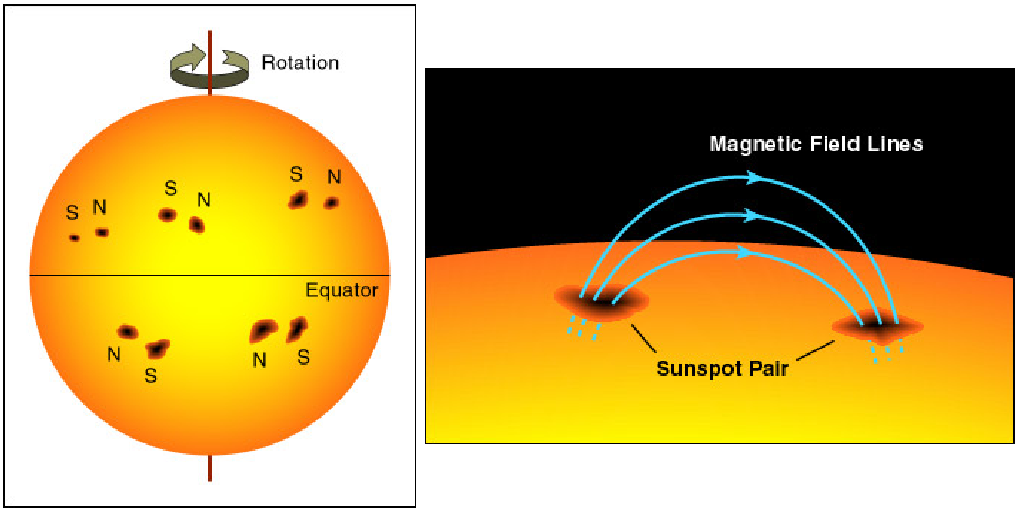

Figure 2.4: Sunspots are regions of the solar surface cooler than the others and visible on the photosphere as dark areas of irregular shape

The sunspot number is a good natural monitor of Sun's activity: when activity reaches its maximum the sunspot number also reaches its maximum and vice versa.

Experimental observations indicate that, during a solar minimum period, the magnetic field is approximately dipole-like, with a magnetic dipole axis almost aligned with the solar rotation axis, while during the declining phase of the solar cycle the dipole is more tilted. The angle between the rotation axis and the magnetic axis is known as the **tilt angle** α.

Even though the Sun has a complex magnetic field, the dipole term nearly always dominates the magnetic field. As the Solar activity approaches its maximum, when the polarity reversing happens, the dipolar shape seems to be no more representative of the solar magnetic field. Depending on whether the dipole is oriented parallel or anti-parallel relatively to the rotation axis, the solar magnetic epoch is referred to as $\mathbf{A > 0}$ or $\mathbf{A < 0}$ (figure 2.5).

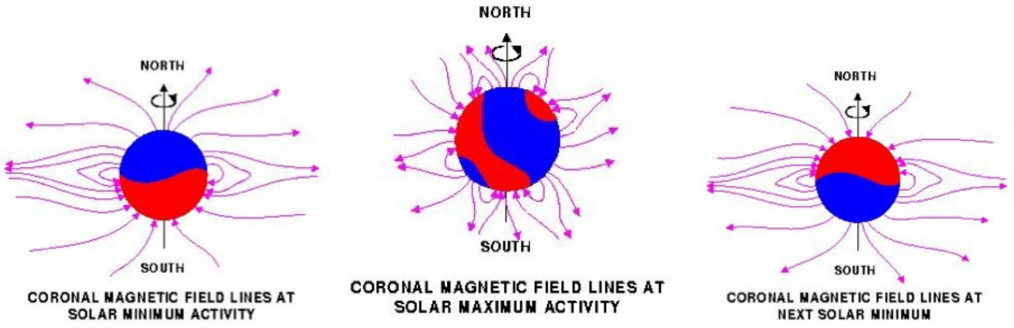

(a) $A > 0$ **(b)** **(c)** $A < 0$

Figure 2.5: Sun's magnetic field in several periods.

The link between solar activity and the modulation in intensity of the GCR is evident from the Neutron Monitors (NM) measurements, available in the last decades. The NM are a worldwide network of detectors that measure the number of neutrons reaching Earth's surface, as a function of time. The surface neutrons come from the hadronic showers, produced by the interaction of the primary particle with the atmosphere. There are basically two contributions to the total rate of neutrons. The first one N_0 ($\sim$ 5500 counts/min) , is approximately constant in time, and comes from the interaction of high energy particles ($\sim$100 GeV) with the atmosphere. The second term $N(t)$ ($\sim$ 500 counts/min), comes from the interaction of the low energy particles ($\sim$10 GeV) with the atmosphere. This low energy contribution varies with time and depends on the activity of the Sun. Figure 2.6 shows the Oulu NM counting rate as a function of time (top plot), and the sunspot number (bottom plot). The clear anti-correlation between the NM counting rate and the sunspot number indicates that the Solar activity has an influence on GCR : at solar maximum there is a minimum of the GCR intensity, while at solar minimum there is a maximum of the GCR intensity. The flux on the top of the atmosphere can be calculated using the NM counting rates, if the yield function of the NM station is known. The yield function depends on the average depth of atmosphere and cut-off rigidity (see 2.5.4) for the position of the NM station. After calculating the flux at the top of the atmosphere it is possible to extract the Solar modulation parameter (the meaning of this parameter will be discussed in Chapter 4).

Indeed, it is well established that GCR modulation is due to the fact that CRs enter the heliosphere and undergo processes such as scattering by the irregularities of the magnetic field, convection and adiabatic deceleration in the expanding Solar Wind. The physical mechanisms of the modulation will be studied in the next sections. Here it is described the structures of the heliosphere that are relevant to the comprehension of what follows.

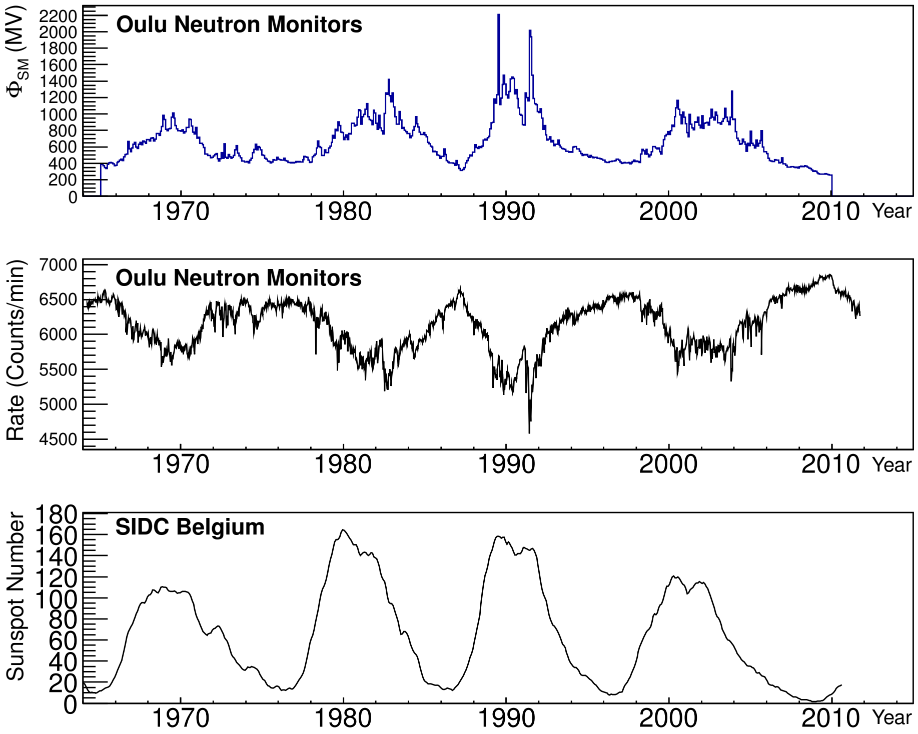

Figure 2.6: Solar modulation parameter from NM network data [46] . Sunspot Number (SIDC Belgium)[9] and neutron rates as measured by Oulu NM station. The anticorrelation between the neutron counting rates and the sunspot number is evident.

2.5.2 Solar Wind and the Heliospheric Magnetic Field

The temperature of the ionized gas inside Sun's corona is so high that it is not gravitationally bound to the star and constantly blows away from Sun's surface to maintain the hydrostatic equilibrium [10] . The supersonic solar plasma expanding into space is called *Solar Wind*: it consists of a fully ionized gas, basically composed of low energy electrons and protons ($E \simeq 0.5 MeV$), pushed radially out of Sun's corona.

Due to the high conductivity of the plasma, the magnetic field of the Sun is frozen into the Solar Wind[1]. As the Sun rotates in approximately 27 days, the magnetic field lines, transported by the Solar Wind, get wrapped into an Archimedean spiral in the Sun's equatorial plane and in helices out of the equator (figure 2.7). Variations in the Sun's magnetic field are consequently carried outward by the Solar Wind.

The *heliosphere* can be defined as the region in space where the Solar Wind dominates (figure 2.8). The plasma pressure fades out with distance until a boundary layer called *heliopause*, where there is a pressure balance with the ISM. The point where the Solar Wind slows down and becomes subsonic is called Termination Shock (TS). On the other side, the point where the ISM, traveling in the opposite direction, becomes subsonic as it collides with the heliosphere is called *bow shock.* In December 2004, the Voyager 1 spacecraft found the termination shock at a distance of approximately 94 AU from the Sun.

---

[1] see Appendix A for a proof of this effect

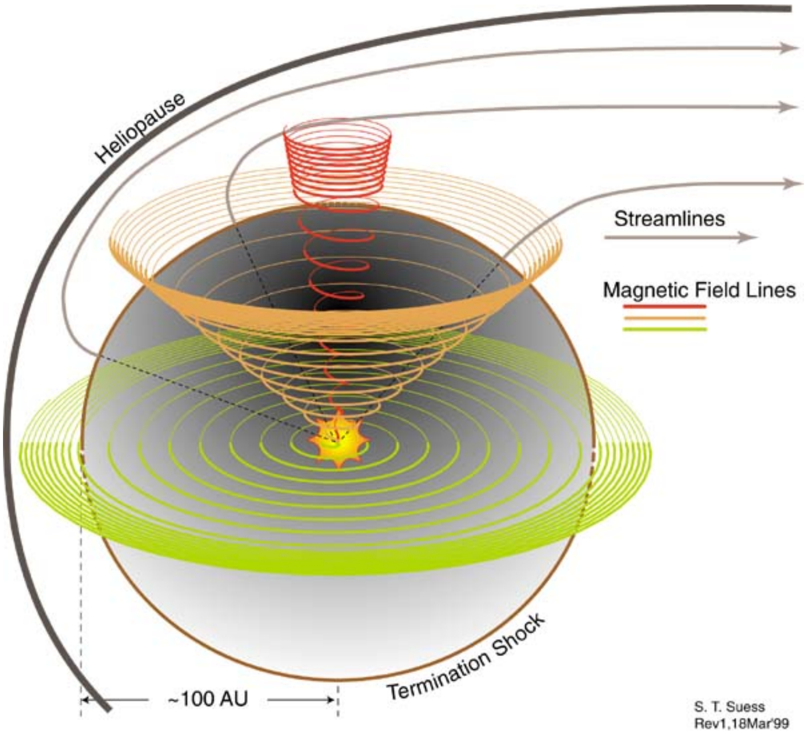

Figure 2.7: The effect of Sun's rotation on the magnetic field lines,that bent into Archimedean spirals. They are drawn here at Solar latitudes of 6, 45 and 84 degree respectively [11].

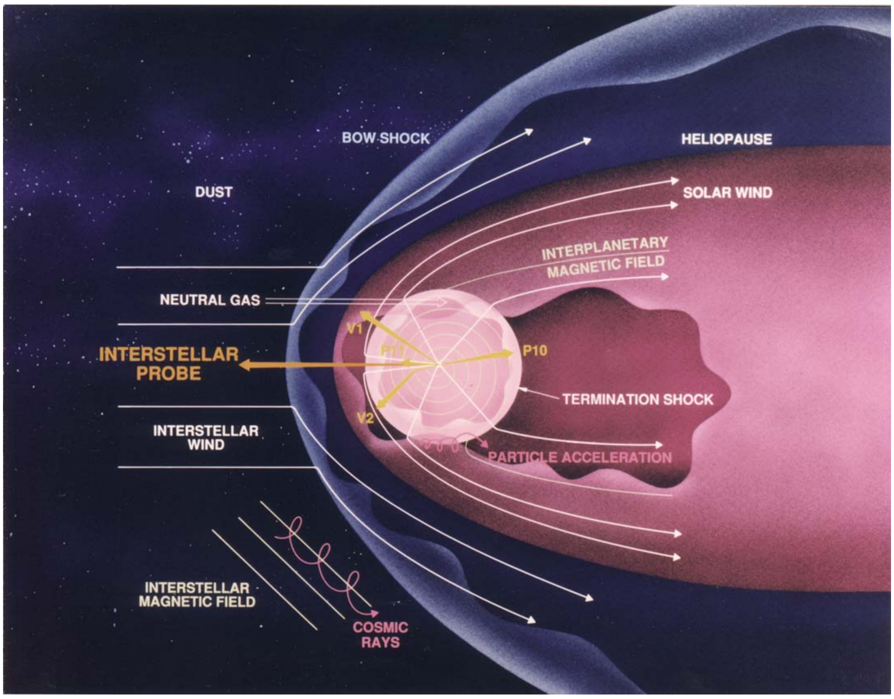

Figure 2.8: The heliosphere, where is clearly visible the Bow Shock, the Heliopause and the Termination Shock.

In a frame with origin at the Sun, the HMF has the following expression in spherical coordinates[2]

$$\vec{B} = \frac{A}{r^2}(\vec{e_r} - \tan\Psi\vec{e_\phi})\left[1 - 2H\left(\theta - \frac{\pi}{2}\right)\right] \tag{2.19}$$

where Ψ is the angle between the radial and azimuthal components of the HMF,H is the Heaviside step function and A is a constant. The two heliospheric hemispheres are separated by a flat surface ($\theta = \pi/2$) - the Heliospheric Current Sheet (HCS) - which is effectively the extension of the solar magnetic equator into the Solar Wind. Above $\pi/2$, the field points in one direction and below $\pi/2$ the field reverses its direction. This expression is only valid for periods when the dipole and rotation axis are aligned (during Solar minimum). When the magnetic and rotation axes are not aligned, the flat current heliosheet turns into a wavy one - the so called ballerina skirt (figure 2.10).

The angle between the rotation and magnetic axes (tilt angle) is of course proportional to the latitudinal extent of the HCS, in other words, large tilt angles correspond to a more undulated HCS.

As a consequence of the wavy character of the HCS, expression 2.19 must be corrected. The division between the two heliospheric hemispheres, which was previously a flat surface ($\theta = \pi/2$), is now a complex wavy structure.

The derivation of the HCS expression is an easy trigonometrical exercise, that can be done by considering two planes tilted at an angle α relative to each other (fig. 2.9).

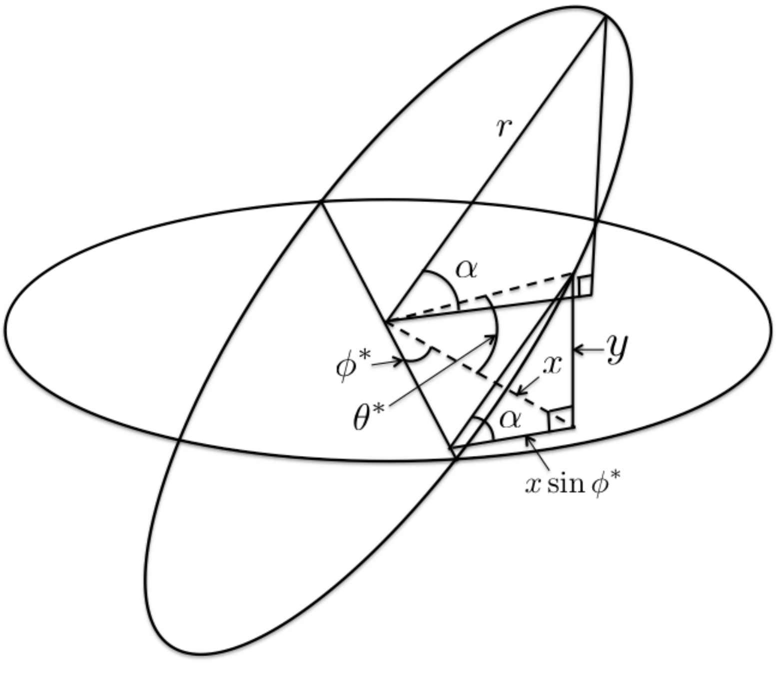

Figure 2.9: Two planes tilted at an angle α relative to each other.

According to the figure

$$\frac{y}{x} = \tan\theta^* \tag{2.20}$$

$$\frac{y}{x\sin\phi^*} = \tan\alpha \tag{2.21}$$

Plugging these two last expressions together

$$\tan\theta^* = \sin\phi^*\tan\alpha \tag{2.22}$$

---

[2] as deduced in Appendix B and depicted in 2.7

Now, if the plane with ϕ^* is assumed to be at $\pi/2$, then the angle $\theta^{'}$ can be defined as $\theta^{'} = \pi/2 - \theta^*$. Therefore

$$\tan(\pi/2 - \theta^{'}) = \sin\phi^* \tan\alpha = \xi \tag{2.23}$$

And so,

$$\theta^{'} = \pi/2 - \tan^{-1}(\tan\alpha \sin\phi^*) \tag{2.24}$$

The last step is just the substitution of the expression for $\phi^* = \Omega\frac{r-r_0}{V} + \phi_0$, which can be easily derived using the first two equations of Appendix B, in equation 2.24.

The final expression for the HCS (as depicted in figure 2.10(b))is

$$\theta^{'} = \pi/2 - \tan^{-1}\left[\tan\alpha \sin\left(\Omega\frac{r-r_0}{V} + \phi_0\right)\right] \tag{2.25}$$

and the correct expression for the HMF is

$$\vec{B} = \frac{A}{r^2}(\vec{e_r} - \tan\Psi\vec{e_\phi})\left[1 - 2H(\theta - \theta^{'})\right] \tag{2.26}$$

During one solar rotation, the HCS fills a region lying between $\pi/2 - \alpha \le \theta^{'} \le \pi/2 + \alpha$. The frequency of the HCS depends on the angular velocity of the Sun Ω, and the Solar Wind velocity V, while the phase is given by ϕ_0, V and r_0, the radius of the Sun.

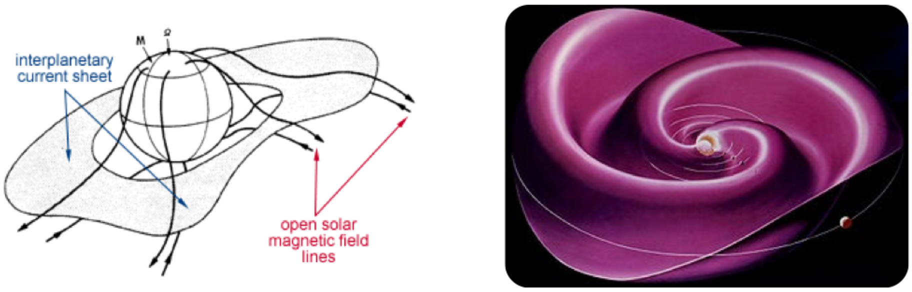

(a)

(b)

Figure 2.10: a) HCS. Note that the current sheet separates zones with different magnetic polarities. b) Drawing of the wavy neutral current heliosheet

The Solar magnetic polarity and the structures of the HMF are related to the modulation of GCR depending on the charge-sign of the particle (the HCS is responsible for some of the drift terms that appear in the transport equation of cosmic rays [12]). Actual observations and theories about charge-dependent GCR modulation link together the solar magnetic polarity and the structures of the magnetic field, as they result in different drift patterns for different charges in the heliosphere.

This last fact is visible in NM data of figure 2.6. It shows, in addition to the 11 years periodicity,the existance of a profile that can be referred to the HMF polarity: the shape of sucessive maxima alternates between a broad flat and a more narrow peaked one.

This kind of observation is very important and constitutes the first evidence that the solar modulation has a 22 years periodicity and that the orientation of the solar magnetic dipole has an effect on GCR propagation. This periodicity is seen in the NM counting rates but not in the Sunspot number, which indicates that it might not be the best proxy for the solar modulation of GCR's. It also means that it is not the status of the Sun that directly guides the transport of the GCR's, but rather the status of the heliosphere they move through.

2.5.3 Propagation in the Heliosphere: Parker Model

This model was proposed by Parker in 1964 [13], and it is based on the assumption that the GCR reach the heliophere isotropically, and after entering it, face an outward Solar Wind and the HMF.

The HMF can be divided in two parts:

1. The large scale HMF responsible for the drifts and curvatures of the guiding centres of the particles
2. Small scale irregularities

The inclusion of these small scale irregularities by Parker was based in the measurements done by *Explorer XVIII*, that registred small fluctuations in the HMF of about 10^5 km -10^7 km. These fluctuations play a very important role in the propagation of the GCR inside the Solar cavity, since they are responsible for the *diffusion* of low energy particles. Another aspect that will help the diffusive character of the transport is the very low density of cosmic rays when compared with the density of Solar Wind particles.

To better understand the underlying phenomenon, consider a particle with a gyroradius much grater than the scale of the fluctuations in the magnetic field. This particle will follow its trajectory without noticing the presence of the magnetic field irregularities.

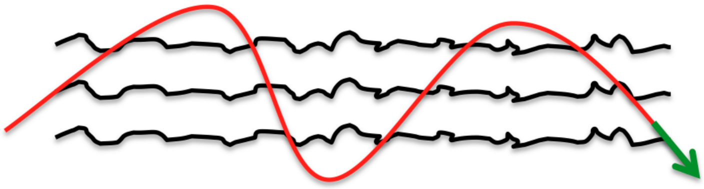

Figure 2.11: Dynamics of a charged particle in a magnetic field when the dimension of the irregularities is smaller than the gyroradius

However, if the fluctuations have the same scale as the gyroradius of the particles, there is a significant amount of scattering. The scattering of the particles by random superposition of these fluctuations leads to stochastic changes (random walk) in the pitch angle of the particles (angle between $\vec{v}$ and $\vec{B}$). The result is a *diffusive phenomenon.*

Knowing the dimensions of the fluctuations, it is easy to calculate the magnetic rigidity R, at which the magnetic fluctuations are important in scattering the particles[3].The gyroradius of a particle in terms of its magnetic rigidity is:

$$r_g = \frac{pc}{Ze} \cdot \frac{1}{Bc} = \frac{R}{Bc} \tag{2.27}$$

where it has been assumed $\vec{B} \perp \vec{v}$ (pitch angle of 90°). Equating this gyroradius to the wavelenght at which there is more power in the power spectrum of the magnetic irregularities - 10^9m (assuming an average HMF of 3nT)

$$R = 3nT \cdot c \cdot 10^9 m \approx 1GV \tag{2.28}$$

This rigidity is remarkably similar to that at which the spectra of GCR protons and nuclei become strongly influenced by Solar modulation 2.1(b). The important assumption is that the magnetic field irregularities are random.

This diffusive transport is described by a diffusion coefficient, in this case a tensor K_{ij}. The motion is brownian and does not preserve the memory of the past, meaning that each increment is independent of the previous one.

---

[3] notice that particles with different masses and charges, but with the same magnetic rigidity have the same dynamics under any magnetic field distribution

Introducing the classic particle distribution probability $W(x_i, t)$ (number of particles per unit volume) it is easy to see that the quantity $-K_{ij}\frac{\partial W}{\partial x_j}$ is just the flux of particles in the frame comoving with the magnetic irregularities responsible for the scattering. The irregularities are also moving with velocity equal to the solar wind velocity V_{SW} , and so giving rise to a convective flux of the form $V_{SWi}W$.

Applying the continuity equation it is possible to write the diffusion equation or Fokker-Planck equation as:

$$\frac{\partial W}{\partial t} + \frac{\partial}{\partial x_i}(V_{SWi}W) - \frac{\partial}{\partial x_i}(K_{ij}\frac{\partial W}{\partial x_j}) = 0 \tag{2.29}$$

or

$$\frac{\partial W}{\partial t} + \nabla \cdot \vec{S} = 0 \tag{2.30}$$

$$S_i = V_{SWi}W - K_{ij}\frac{\partial W}{\partial x_j} \tag{2.31}$$

where $\vec{S}$ is the flux vector containing the diffusive and convective terms.

Now, while the energetic particle is riding along with the fields in the wind, the magnetic field itself is expanding because of the divergence of the wind, which makes the particle lose energy - **adiabatic cooling**.

To prove the last statement, consider two frames of reference:

- O fixed;
- O' moving with the Solar Wind velocity V;

If the velocities involved are non-relativistic[3] :

$$\vec{v'} = \vec{v} - \vec{V} \tag{2.32}$$

$$\vec{p'} = \vec{p} - m\vec{V} \tag{2.33}$$

If the electric field is negligible, when compared to the average magnetic field, the force applied in a particle of charge q is

$$\frac{d\vec{p}}{dt} = q(\vec{v} - \vec{V}) \times \vec{B} \tag{2.34}$$

In the moving frame, $\vec{p'}$ is a function of x_i, $\vec{p}$ and t and so

$$\frac{d\vec{p'}}{dt} = \frac{\partial\vec{p'}}{\partial t} + \vec{v}\cdot\frac{\partial\vec{p'}}{\partial x_i} + \frac{d\vec{p}}{dt}\cdot\frac{\partial\vec{p'}}{\partial\vec{p}} \tag{2.35}$$

Deriving the expression 2.33 with respect to t, x_i and $\vec{p}$

$$\frac{\partial\vec{p'}}{\partial t} = -m\frac{\partial\vec{V}}{\partial t} \tag{2.36}$$

$$\frac{\partial\vec{p'}}{\partial x_i} = -m\frac{\partial\vec{V}}{\partial x_i} \tag{2.37}$$

$$\frac{\partial\vec{p'}}{\partial\vec{p}} = \mathbb{I} \tag{2.38}$$

---

[3] The relativistic case is very similar and straightforward. The Galilean Transformation is replaced by the Lorentz formula for adding velocities : $v' = \frac{v-V}{1-\frac{v\cdot V}{c^2}}$

Substituting 2.32 into 2.34

$$\frac{d\vec{p}}{dt} = q\vec{v'} \times \vec{B} \tag{2.39}$$

Now, having all the terms, eq. 2.35 can be rewritten as

$$\frac{d\vec{p'}}{dt} = -m\frac{\partial \vec{V}}{\partial t} - mv \cdot \frac{\partial \vec{V}}{\partial x_i} + q\vec{v'} \times \vec{B} \tag{2.40}$$

The variation of the magnitude of the momentum - $\frac{dp'}{dt}$ - can be obtained by deriving the expression $p'^2 = \vec{p'} \cdot \vec{p'}$

$$\frac{dp'}{dt} = \frac{\vec{p'}}{p'} \cdot \frac{d\vec{p'}}{dt} \tag{2.41}$$

And finally

$$\frac{dp'}{dt} = -\frac{\vec{p'}}{p'} \cdot \left[m\frac{\partial \vec{V}}{\partial t} + (\vec{p'} + m\vec{V}) \cdot \frac{\partial \vec{V}}{\partial x_i} \right] \tag{2.42}$$

where $\vec{p'} \cdot (\vec{v'} \times \vec{B}) = 0$ was used.

The average $\frac{dp'}{dt} \equiv \langle \dot{p'} \rangle$ for a group of particles, all with the same momentum magnitude p' but with different directions is:

$$\langle \dot{p\prime} \rangle = \frac{\int_{\Omega'} \frac{dp\prime}{dt} F d\Omega'}{\int_{\Omega'} F\, d\Omega'} \tag{2.43}$$

where $d\Omega'$ is the infinitesimal solid angle interval.

Assuming an isotropic momentum distribution $F(r, p', t)$

$$\textstyle\int_{\Omega'} d\Omega' = 4\pi; \quad \int_{\Omega'} \vec{p'} d\Omega' = 0; \quad \int_{\Omega'} \vec{p'}\vec{p'} d\Omega' = \frac{4\pi p'^2}{3}\mathbb{I}; \tag{2.44}$$

expression 2.43 can be written in the following form

$$\langle \dot{p'} \rangle = -\frac{p'}{3} \nabla \cdot \vec{V} \tag{2.45}$$

or in terms of kinetic energy T'

$$\frac{1}{p'} \langle \dot{p'} \rangle = \frac{1}{p'}\frac{dp'}{dT'} \left\langle \dot{T'} \right\rangle = \frac{E'}{p'^2} \left\langle \dot{T'} \right\rangle = \frac{T' + m}{T'(T' + 2m)} \left\langle \dot{T'} \right\rangle = \frac{1}{T'\alpha(T')} \left\langle \dot{T'} \right\rangle$$

$$\left\langle \dot{T'} \right\rangle = -\alpha(T')\frac{T'}{3} \nabla \cdot \vec{V} \tag{2.46}$$

where $\alpha(T') = \frac{T'+2m}{T'+m}$. This means $\alpha(T') = 2$ for nonrelativistic particles and $\alpha(T') = 1$ for extreme relativistic particles.

This result is very important and tells that particles will lose energy, regardless of the choice of the scattering model.

Since particles will change their energy due to the movement of the Solar Wind it is more interesting to work with the phase space density $U_p(x_i, p, t)$ instead of working only with space density $W(x_i, t)$.

$$W(x_i, t) = \int_0^\infty U_p(x_i, p, t) dp \tag{2.47}$$

Now, it is possible to apply the continuity equation not to a simple 3-dimensional volume, where the 3 coordinates correspond to x, y, z but to a 4-dimensional volume, adding the momentum as the fourth coordinate

$$\frac{dU_p(x_i, p, t)}{dt} = -\frac{\partial \Phi_{x_i}}{\partial x_i} - \frac{\partial \Phi_p}{\partial p} \tag{2.48}$$

where Φ_p is the number of particles that pass through the momentum boundary per unit of time and Φ_{x_i} is the number of particles that pass through the space boundaries per unit of time.

$$U_p(x_i, p, t)\frac{dp}{dt} = \Phi_p \tag{2.49}$$

then the Fokker-Planck equation for U_p is

$$\frac{\partial U_p}{\partial t} + \frac{\partial}{\partial x_i}(U_p V_{SWi}) + \frac{\partial}{\partial p}\left(U_p \frac{dp}{dt}\right) - \frac{\partial}{\partial x_i}\left(K_{ij}\frac{\partial U_p}{\partial x_j}\right) = 0 \tag{2.50}$$

or using 2.45

$$\frac{\partial U_p}{\partial t} + \overbrace{\frac{\partial}{\partial x_i}(U_p V_{SWi})}^{convection} - \overbrace{\frac{1}{3}\nabla \cdot \vec{V}_{SW}\frac{\partial}{\partial p}(U_p p)}^{adiabatic\ losses} - \overbrace{\frac{\partial}{\partial x_i}\left(K_{ij}\frac{\partial U_p}{\partial x_j}\right)}^{diffusion\ and\ drifts} = 0 \tag{2.51}$$

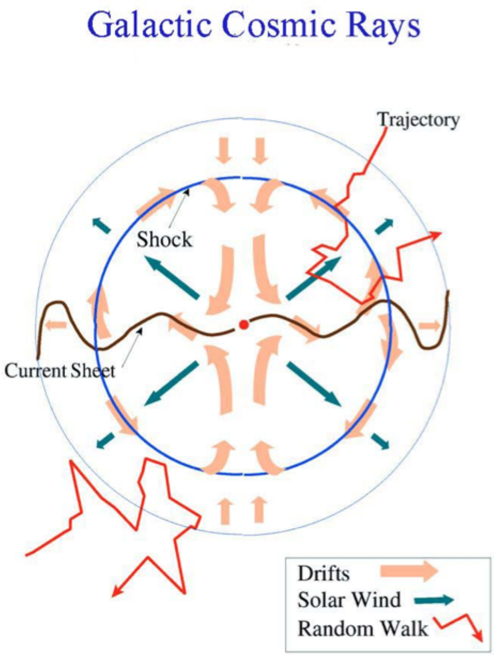

Figure 2.12: Illustration showing the several contributions to the propagation of GCR's inside the Heliosphere.

Now that the transport equation has been derived, the reader may have noticed that the same equation could have been deduced using another density function, the cosmic ray number density per unit of kinetic energy - U_T -, instead of the cosmic ray number density per unit of momentum -U_p.

$$[U_T] = \frac{particles}{m^3 \cdot T} \qquad [U_p] = \frac{particles}{m^3 \cdot p} \tag{2.52}$$

The derivation of the transport equation in terms of U_T is very similar, but using 2.46 instead of 2.45

$$\frac{\partial U_T}{\partial t} + \frac{\partial}{\partial x_i}(U_T V_{SWi}) - \frac{1}{3}\nabla \cdot \vec{V}_{SW}\frac{\partial}{\partial T}(\alpha(T) U_T T) - \frac{\partial}{\partial x_i}\left(K_{ij}\frac{\partial U_T}{\partial x_j}\right) = 0 \tag{2.53}$$

Indeed, there is also an additional third way of writing the transport equation in terms of the omnidirectional cosmic ray distribution function f_0, a function of cosmic ray position and momentum at time t.

$$[f_0] = \frac{particles}{m^3\, p^3} \tag{2.54}$$

In this case the transport equation is given by[4]

$$\frac{\partial f_0}{\partial t} = -\nabla \cdot \vec{S} + \frac{1}{3}\nabla \cdot V_{SW} \frac{\partial f_0}{\partial \ln p} \tag{2.55}$$

where

$$\vec{S} = 4\pi p^2 (C V_{SW} - K \cdot \nabla f_0) \tag{2.56}$$

is the differential current density, and

$$C = -\frac{1}{3}\frac{\partial f_0}{\partial \ln p} \tag{2.57}$$

is the Compton-Getting coefficient,i.e., one third of the spectral index of a power law spectrum in momentum space.

Substituting $\vec{S}$ in equation 2.55

$$\frac{\partial f_0}{\partial t} = \nabla \cdot (K \cdot \nabla f_0) - V_{SW} \cdot \nabla f_0 + \frac{1}{3}\nabla \cdot V_{SW} p \frac{\partial f_0}{\partial p} \tag{2.58}$$

Having 3 ways of writing the same equation it is natural to study the relation between the different number densities -U_T, U_p- and the omnidirectional distribution function -f_0. To begin the study, it is firstly assumed that the cosmic ray distribution function $f(r,p,t)$ can be written as ([14],[15],[16])

$$f(r,p,t) = f_0(r,p,t) + \frac{3\vec{p} \cdot \vec{f_1}}{p} \tag{2.59}$$

where the component f_0, the omnidirectional distribution function, is a scalar that does not depend on the direction in space, and f_1 is a vectorial quantity that depends on the direction.

By definition

$$U_p(r,p,t) = p^2 \int_{\Omega} f(r,p,t)\, d\Omega \tag{2.60}$$

Assuming that f_1 is constant in magnitude and along the x-direction

$$U_p(r,p,t) = p^2 \int_0^{\pi} \int_0^{2\pi} (f_0 + 3 f_1 \sin\theta \cos\phi) \sin\theta\, d\theta\, d\phi = 4\pi p^2 f_0 \tag{2.61}$$

The goal is to relate all the number densities and the distribution function with a measured quantity: the differential intensity.

The definition of differential intensity is just the number of particles dN that cross a differential area element dA, perpendicular to momentum vector $\vec{p}$ in the interval $[p, p+dp]$ within $d\Omega$, in interval dt.

$$dN = J_P\, dA_{\perp}\, dt\, d\Omega\, dp \tag{2.62}$$

---

[4] a careful derivation of this equation can be found in Webb and Gleeson [1979] [13]

All particles crossing the above mentioned surface must have come from a cylinder with length vdt and cross sectional area $dA_\perp$, implying that there were

$$dN = f\,v\,dt\,d^3p\,dA_\perp = v\,f\,p^2\,dt\,dp\,d\Omega\,dA_\perp \tag{2.63}$$

and so

$$J_P = vp^2 f(x,p,t) \tag{2.64}$$

The mean value of J_P: $\langle J_P\rangle$ is the omnidirectional differential intensity

$$\langle J_P\rangle = \frac{\int_\Omega J_P d\Omega}{\int_\Omega d\Omega} = \frac{1}{4\pi}\int_\Omega J_P d\Omega = \frac{vU_P}{4\pi} = vp^2 f_0 \tag{2.65}$$

$$[J_P] = \frac{\text{particles}}{\text{m}^2\, s\, p\, \text{sr}} \text{ with momentum in d}^3\text{p about p}$$

$$[\langle J_P\rangle] = \frac{\text{particles}}{\text{m}^2\,\text{s p sr}} \text{ with all the possible momentum in the interval [p,p+dp]}$$

Geometrically, this means that $\langle J_P\rangle$ is the algebraic sum of J_P, normalized to the unit solid angle. It is also possible to calculate the differential intensity per unit of energy

$$J_P = \frac{dT}{dp} J_T = vJ_T \tag{2.66}$$

2.5.4 Earth's Magnetic Field

Before reaching Earth, a charged particle has to face the opposition of the geomagnetic field, which will curve its trajectory and consequently sets an energy limit below which, the particle cannot pass the magnetic barrier. The Geomagnetic Field is, in first approximation, a magnetic dipole located a few kilometers from the center of the Earth and roughly pointing south.

The Geomagnetic Coordinate System (figure 2.14(a)) is defined so that its Z-axis is parallel to the magnetic dipole axis. The angles are defined somehow differently from those conventionally used in physics: the geomagnetic latitude λ is the angle measured from the geomagnetic equator, defined as the plane normal to the dipole axis, to the point considered and containing Earth's center.

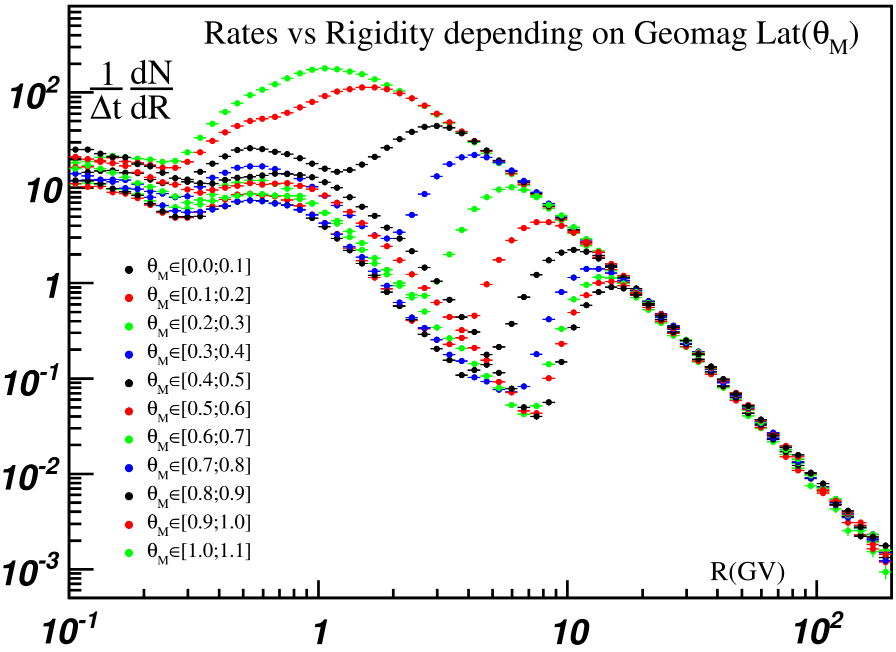

Figure 2.13: Rates measured by the AMS-02 detector at different geomagnetic latitudes (in radians). Note that, as the latitude increases, the rigidity cut-off decreases.

The geomagnetic cut-off was derived by Stöermer in the mid-twentieth century, and represents the minimal rigidity a charged particle must have to reach a point located at an altitude h above the surface, and at the the geomagnetic latitude λ.

This cut-off also depends on the East-West angle α (figure 2.14(b)), corresponding to the angle between the velocity of the particle and the East-West direction.

The expression for the cut-off is

$$R_{cut} = \frac{60}{\left(1+\frac{h}{r_e}\right)^2} \frac{\cos^4\lambda}{\left[\sqrt{1+\cos\alpha\cos^3\lambda}+1\right]^2} \text{ [GV]} \tag{2.67}$$

The cut-off rigidity is higher in the equator and lower in the poles,as can be seen in figure 2.13, allowing that an higher number of CRs reach the poles.

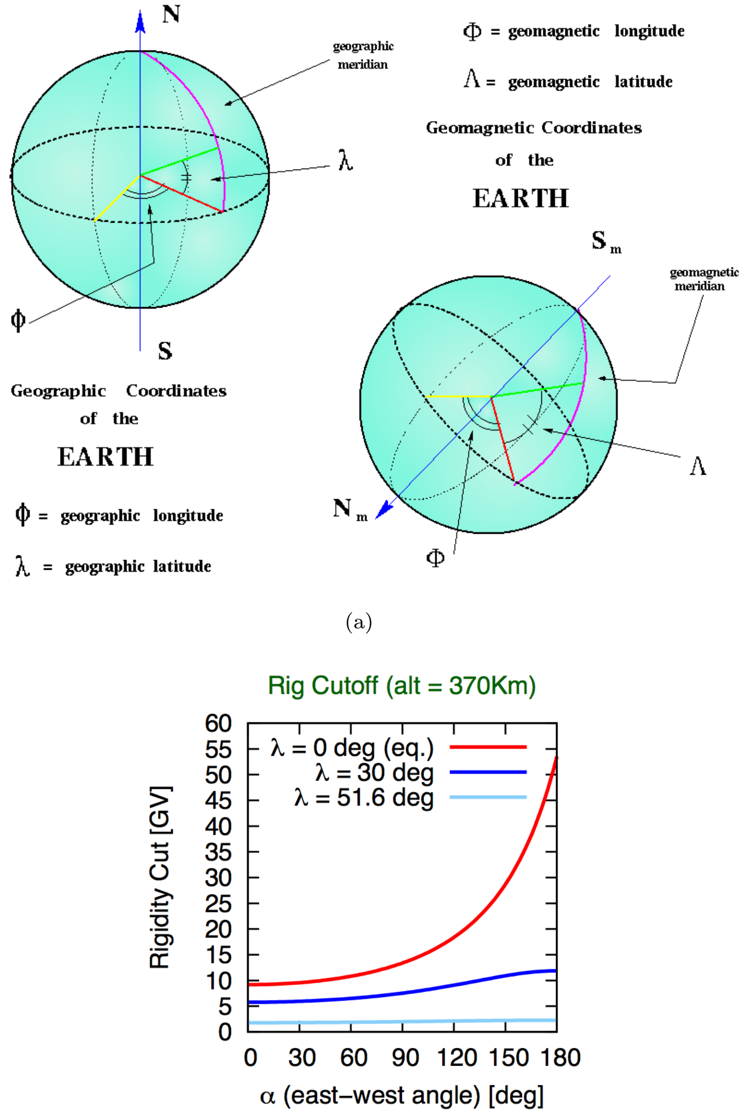

(a)

(b)

Figure 2.14: a) Geographic and Geomagnetic Coordinates. [17]. b) The Rigidity Cut-off as a function of the geomagnetic latitude [18]

3

THE AMS-02 EXPERIMENT

Alpha Magnetic Spectrometer (AMS) is an international collaboration involving hundreds of researchers from 56 institutes and 16 countries. The main goal of the collaboration was to take a particle spectrometer to space.

This task was divided in two parts: the first one (AMS-01) took place in June 1998, when a preliminary detector flew aboard the Space Shuttle with the objective of testing the AMS concept; the second one (AMS-02) occurred in May 2011, when the final detector was installed aboard the International Space Station (ISS) , where it is expected to operate continuously between 10 to 18 years.

Figure 3.1: The AMS-02 detector aboard the ISS [39].

3.1 Scientific goals of AMS-02

The physics aims of AMS-02 are:

- Measurement of cosmic ray spectra from a few hundred MeV up to 1 TeV, in particular:
  - Hydrogen, helium and beryllium isotopes (D/p,^{3}He/^{4}He,^{10}Be/^{9}Be);
  - Secondary to primary spectrum (B/C, sub-Fe/Fe);
  - Cosmic gamma-ray spectrum;
- Search for indirect signals of non-baryonic dark-matter through the detection of annihilation products appearing as anomalies of the cosmic-ray spectra (e^{+}, $\bar{p}$, γ and $\bar{D}$);
- Search for cosmological antimatter through the detection of antinuclei with |Z|>2;

3.2 Detector Description

AMS-02 is the first large magnetic spectrometer in space, and it is able to measure, with unprecedented accuracy, fluxes of CRs above Earth's atmosphere. The spectrometer is composed of several subdetectors:

- a Transition Radiation Detector (TRD)
- a Time-of-Flight (TOF) detector
- a Silicon Tracker
- a set of Anticoincidence Counters (ACC)
- a Ring Imaging Cerenkov (RICH) detector
- an Electromagnetic Calorimeter (ECAL).

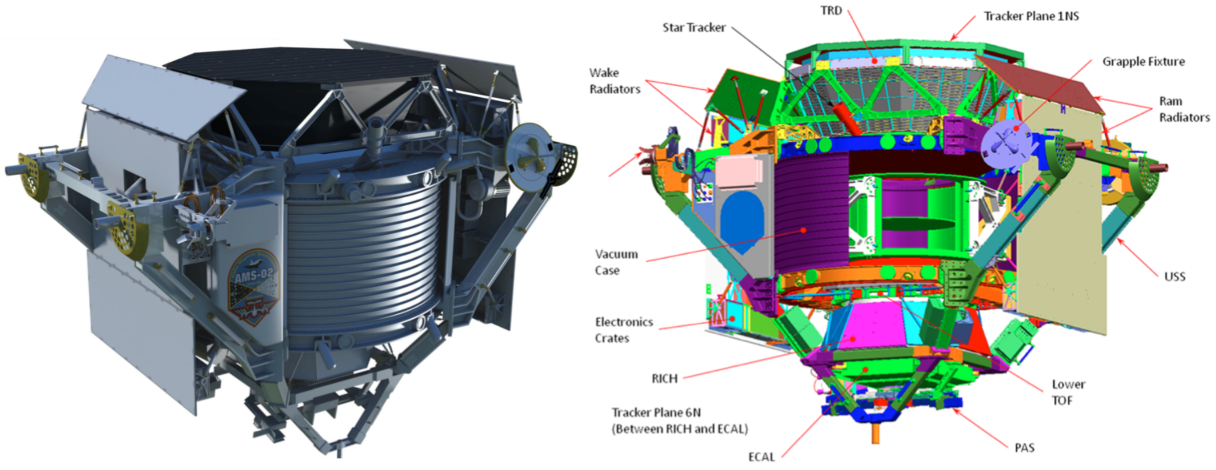

Figure 3.2: The AMS-02 detector [39].

The permanent magnet

The AMS-02 permanent magnet was already used in the AMS-01 flight and it is a cylinder of 1m diameter and 1m height, made of 6000 Neodimium-Iron-Boron blocks. It creates a magnetic field of 0.15 T (bending power is BL^2 =0.15Tm^2), uniform along the x axis, and with negligible dipole moment.

Transition Radiation Detector (TRD)

The TRD is the first subdetector that the majority of the particles face when entering the spectrometer. The working principle of the TRD is based on the emission of transition radiation by the particles that cross it.

Transition radiation is a particular type of electromagnetic radiation in the X-ray region (1 - 50 KeV), emmited when a charged particle crosses the boundary between two media with different dielectric constants. The energy of the transition radiation photons is proportional to $\gamma = E/m$, and has a threshold of $\gamma \approx 500$, making low mass particles, such as positrons or electrons, likely emitters of transition radiation energy. This allows a separation between low mass and high mass particles (for protons with momentum between 10 - 300 GeV the rejection factor is 10^2 - 10^3).

Since the emission probability of a single interface is very low ($\sim 10^{-2}$), the subdetector is made in a multilayer structure (20 layers supported by an octogonal pyramidal structure),allowing for hundreds of transitions when a particle crosses the TRD. The building blocks of the 20 layers are 328 modules, each having a fleece radiator with thickness of 20 mm and straw tube proportional wire chambers filled with a Xe/CO_2 (80%:20%) mixture.

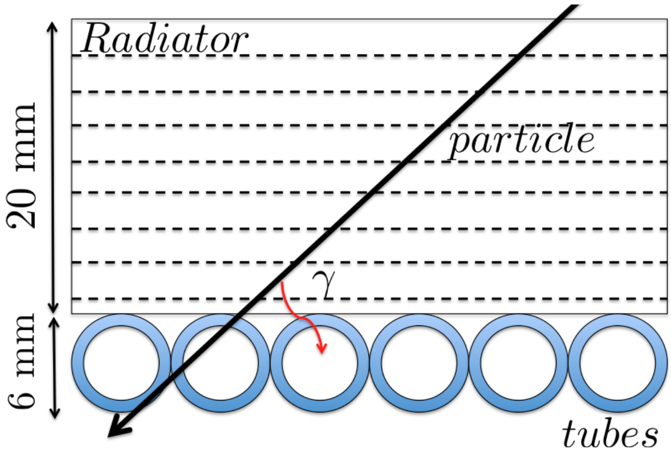

Figure 3.3: TRD module.

Time-of-Flight (TOF)

The TOF is the subdetector responsible for fast triggering the particles that reach the detector, distinguishing between upward and downward particles, measuring the velocity (σ_β=3% for protons), and estimating the value of the charge up to $Z \approx 20$. The TOF system consists of four planes with 8,8,10 and 8 plastic scintillator counters each. The planes are roughly circular with 12 cm wide scintillator paddles, one pair of planes above the magnet called the upper TOF and the other below the magnet TOF, called the lower TOF.The quality of the measurements is increased by having perpendicular paddle orientations in both pairs of planes.

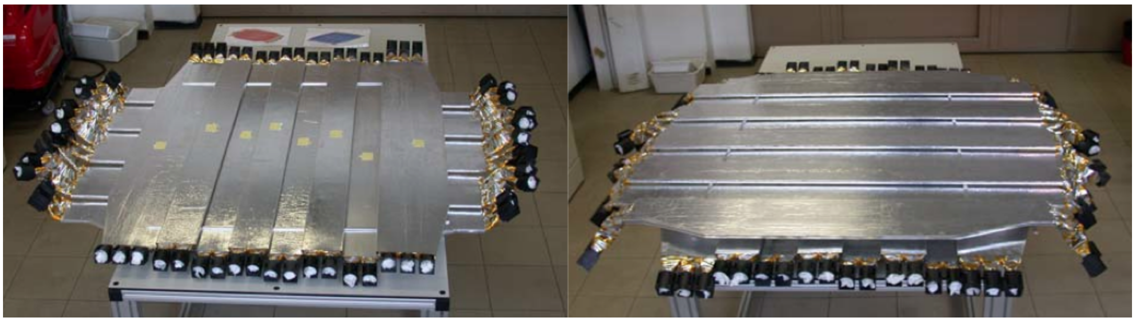

Figure 3.4: TOF planes.

Silicon Tracker

The Silicon Tracker is responsible for making measurements of particle positions with a precision of $\sim 10\mu m$ along the bending plane (yOz), and $\sim 30\mu m$ on the transverse direction. By finding the trajectory of the particle inside the magnetic cavity, it is possible to calculate the particle rigidity with a precision of 2% at a few GV (for protons, the Maximum Detectable Rigidity (MDR) is around 1.3 TeV). The silicon tracker is also capable of measuring the charge of the particle up to $Z \approx 26$.

The tracking system is composed of 9 layers: 1 above the TRD, 1 above the ECAL, and the other set of 7 in the central region (inner tracker). The layers are made of $\sim$ 2500 double-sided silicon microship sensors arranged on 192 ladders.

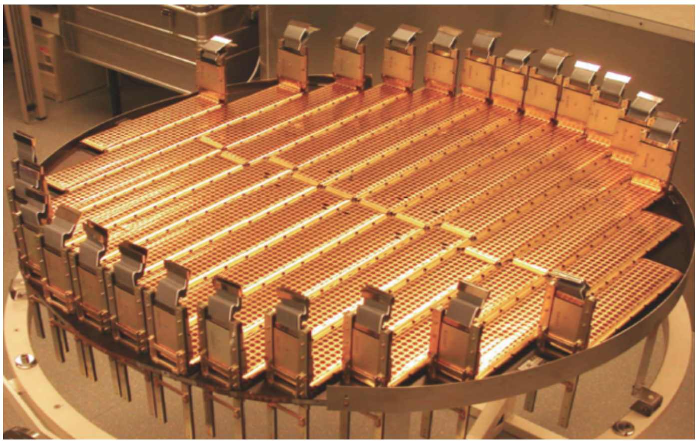

Figure 3.5: Tracker plane.

The Anti-Coincidence Counters (ACC)

The ACC are made of scintillators, surrounding the silicon tracker, and fitted tightly inside the inner bore of the detector's magnet. The purpose of the ACC is to detect particles entering the Tracker laterally, outside the main acceptance, which may create signals in the detector leading to bad event reconstruction.

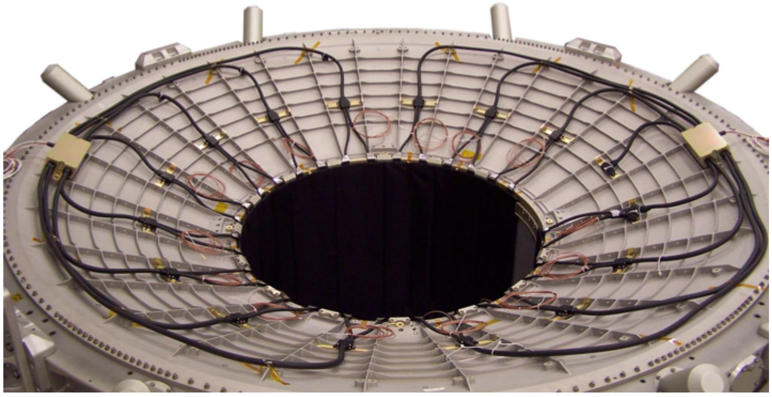

Figure 3.6: ACC view.

The Ring Imaging Cerenkov Detector (RICH)

The RICH is responsible for measuring, with high precision, the velocity of particles that emmit a Cerenkov cone when transversing it. The opening angle of the cone depends on the velocity and on the refractive index of the material. By measuring the number of emitted photons, it is possible to compute the charge of the particle.

It consists of a radiator plane, a conical mirror and a photon detection plane. The radiator has two regions: the outer region, made of thick aerogel tiles ($n \approx 1.03 - 1.05$) and the central region, composed of thick sodium fluoride (NaF) radiator ($n \approx 1.33$). The detector plane is made of 680 4×4-multi-anode Photomultipliers (PMT) (gain 106 at 800 V).

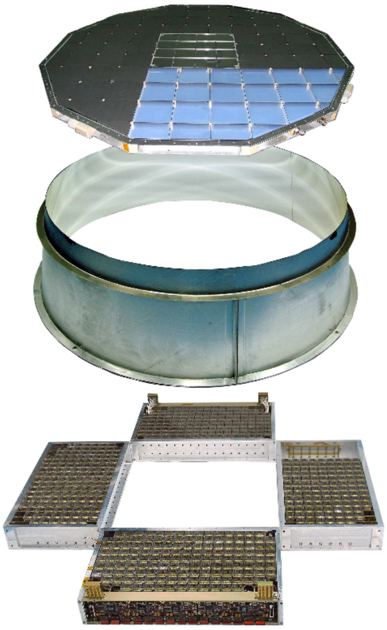

Figure 3.7: RICH exploded view.

The Electromagnetic Calorimeter (ECAL)

The ECAL, placed at the bottom of the detector, is a fine grained lead-scintillating fiber sampling calorimeter,with an active area of 648 × 648 mm^2 and a thickness of 166.5 mm. It provides an accurate 3-D imaging of the longitudinal and lateral shower development and a precise value of the shower energy. Additionally, It serves as a powerful tool to distinguish hadrons from electrons or positrons, as the type of shower developed inside the detector is completely different.

It is also worth noting that the ECAL is able to detect gamma-rays, either by measuring the interaction of the photon inside the detector, or through the identification of a particle-antiparticle pair produced in the matter preceding it.

The AMICA Star Tracker

The Astro Mapper for Instrument Check of Attitude (AMICA) consists of a pair of small optical telescopes instaled near the Silicon Tracker structure. It serves the purpose of measuring the orientation of the detector, allowing for the identification of γ ray sources .

3.3 AMS in the International Space Station

Since 19^{th} May 2011, AMS is orbiting around Earth every 90 minutes, at an altitude of around 400 Km and is collecting around 40 million of events a day. When a particle triggers the AMS detector, a signal is sent to all sub-detectors and its raw data is gathered in JMDC, the main AMS board computer. Framed data is then downloaded to the AMS laptop computer and is sent to Earth through the High Rate Data Link (HDRL), which uses satellites ku-band. At Earth, data is received at the Marshall Space Center and redirected to CERN where it is stored on hard drives and processed. More than 2 10^{10} events have been processed up to the present day. As output of the event processing, root tuples are produced, storing the reconstructed information event by event. In addition, detector calibration is also stored.

The detector is operated and its conditions are continuously monitored from a Payload Operation and Scientific Center installed at CERN, in Geneva. A team of people performs daily 24h shifts, in order to monitor the operative conditions of the different subdetectors (temperature, TRD gas pressure, noise, power consumption).

Subdetector	Size in bytes
Tracker	1100
RICH	250
TOF	500
ECAL	300
TRD	600
Total	$\sim$ 2.8 KB

a)

b)

Figure 3.8: a) Average event size in bytes. b) AMS POCC at CERN

3.4 The analysis software chain

The root tuples with the event information are stored at CERN, using the CASTOR system. To analyze the information stored in the root tuples, a set of AMS C++ classes developed by the collaboration are used. These classes allow to read every detector information before and after data reconstruction. In addition, the Laboratório de Instrumentação e Física de Partículas (LIP) group together with the french laboratory of Grenoble (LPSC) and later on Annecy (LAPP) developed a software structure, named **LxSoft**, where additional user C++ classes were implemented. This classes serve the purpose of making the analysis of the root tuples easier, creates a shareable set of analysis tools and implements specific particle and detector selections.

The development of the **LxSoft** software tool, followed the following ideas:

- simplify the event analysis
- be able to access data on different locations: CERN castor data center, Lyon data center and local data
- implement solar modulation models: force- field, numerical solutions for 1D and 2D
- implement particle reconstruction and identification, specifically to different subdetectors
- calculate the exposure time
- back-trace particles in the geomagnetic field
- implement transformations between different coordinate systems
- determine the geomagnetic cut-off and geomagnetic coordinates

4

Solutions to the transport equation

The main objective of this chapter is to explore the several approaches to solve the Transport Equation (TPE), from the Force Field Solution to the 1D and 2D numerical models

The transport equation 2.58 can be written in a spherical coordinate system rotating with the Sun [19], as

$$\begin{aligned}
\frac{\partial f}{\partial t} &= \left[\frac{1}{r^2}\frac{\partial}{\partial r}(r^2 K_{rr}) + \frac{1}{r\sin\theta}\frac{\partial}{\partial\theta}(K_{\theta r}\sin\theta) + \frac{1}{r\sin\theta}\frac{\partial K_{\phi r}}{\partial\phi} - V\right]\frac{\partial f}{\partial r} \\
&+ \left[\frac{1}{r^2}\frac{\partial}{\partial r}(rK_{r\theta}) + \frac{1}{r^2\sin\theta}\frac{\partial}{\partial\theta}(K_{\theta\theta}\sin\theta) + \frac{1}{r^2\sin\theta}\frac{\partial K_{\phi\theta}}{\partial\phi}\right]\frac{\partial f}{\partial\theta} \\
&+ \left[\frac{1}{r^2\sin\theta}\frac{\partial}{\partial r}(rK_{r\phi}) + \frac{1}{r^2\sin\theta}\frac{\partial}{\partial\theta}(K_{\theta\phi}) + \frac{1}{r^2\sin^2\theta}\frac{\partial K_{\phi\phi}}{\partial\phi}\right]\frac{\partial f}{\partial\phi} \\
&+ K_{rr}\frac{\partial^2 f}{\partial r^2} + \frac{K_{\theta\theta}}{r^2}\frac{\partial^2 f}{\partial\theta^2} + \frac{K_{\phi\phi}}{r^2\sin^2\theta}\frac{\partial^2 f}{\partial\phi^2} + \frac{2K_{r\phi}}{r\sin\theta}\frac{\partial^2 f}{\partial r\partial\phi} \\
&+ \frac{1}{3r^2}\frac{1}{\partial r}(r^2 V)\frac{\partial f}{\partial\ln p}
\end{aligned} \tag{4.1}$$

with V, the radial Solar Wind velocity, and K_{ij} the diffusion tensor in spherical coordinates.

4.1 The Diffusion Tensor and Drifts

As seen in Chapter 2, diffusion is a stochastic process, resulting from pitch-angle scattering of charged particles at magnetic field irregularities.

When a spiraling charged particle encounters an irregularity in a magnetic field line - which has a size similar to the gyroradius of the particle - then the trajectory of the particle depends strongly on the phase of the gyromotion during the interaction. As can be seen in figure 4.1 Some particles will pass through the irregularity (e), others will be reflected back along the field line (f), while still others will effectively "get stuck" in the vicinity of the the irregularity (g). This basically means that the pitch angle of the particle is randomly scattered.

However, when charged particles encounter magnetic field irregularities, there is an additional variable that can change (besides the pitch angle) : the gyrophase. Physically this happens because the gyroradius is "squeezed" when the field is suddenly stronger, or enlarged when the field is weaker. The global effect of this phenomenon is that the particle will attach itself to a neighboring field line (h). Since this is also a random process, it leads to a diffusive flux perpendicular to the background magnetic field.

The diffusive flux has now a component parallel to the background magnetic field, with diffusion tensor $K_{\parallel}$, and one perpendicular, with diffusion tensor $K_{\perp}$ (in the heliosphere the weak-scattering limit is valid - $K_{\perp} << K_{\parallel}$) .

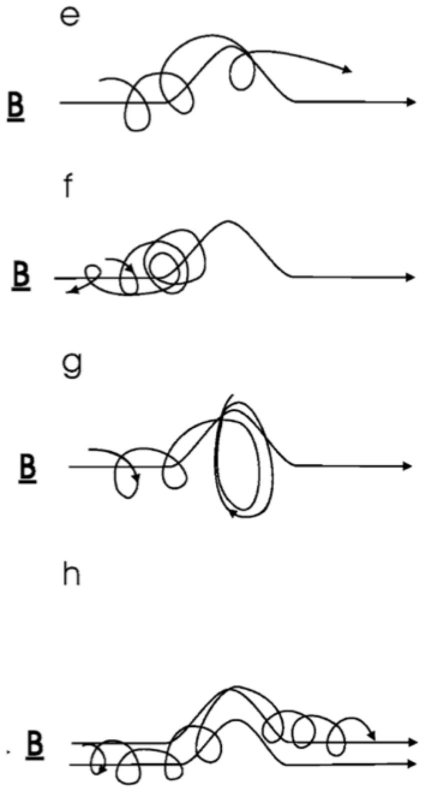

Figure 4.1: Charged Particle Motion in magnetic field (adapted from [20])

The theory of scattering parallel to the background magnetic field is fairly well understood in terms of the so-called Quasi-Linear Theory (QLT) of scattering, developed by Jokipii in 1966 [21]. QLT holds for weak fluctuations, when $\delta B^2/B^2 << 1$, and the parallel diffusion coefficient can be calculated if the power spectrum of the fluctuations in the magnetic field, δB^2, is known. By measuring the spectrum throughout the heliosphere it is possible to determinate a diffusion coefficient depending on the momentum of the particle and on space position.

Potgieter and Le Roux [22] suggested that the parallel diffusion coefficient is given by the following expression

$$K_{\parallel} \approx \beta k_1(r) k_R(R) \frac{B_0}{3B} \tag{4.2}$$

with β, the velocity of the particle divided by c, $k_1(r)$, the term that accounts for the dependence in position, $k_R(R)$, the rigidity dependent term, B the magnitude of the large scale HMF and B_0 the value of the HMF at Earth's orbit. The term k_R is usually expressed in GV and, to a first approximation, can be written as

$$k_R \approx R \tag{4.3}$$

The theory of perpendicular diffusion is much more complicated, and remains one of the biggest theoretical problems in cosmic ray modulation theory. The current theory is non-linear in nature, and was introduced by Mathhaeus et al. (2003) [23].

Due to the absence of a precise theory, the normal procedure when dealing with the perpendicular diffusion coefficient is to scale it relatively to $K_{\parallel}$. Usually

$$K_{\perp} = \rho K_{\parallel} \tag{4.4}$$

with $\rho \approx 0.05$.

The last paragraphs show that the presence of a large-scale magnetic field forces the diffusion to become anisotropic and a diffusion tensor K_{ij} must be used.

In a reference system with the third coordinate along the average magnetic field, the symmetric part of the diffusion tensor, for isotropic perpendicular diffusion, includes both the transverse - $K_{\parallel}$ - and perpendicular -$K_{\perp}$ - components [24].

$$K^S_{i,j} = \begin{pmatrix} K_{\parallel} & 0 & 0 \\ 0 & K_{\perp} & 0 \\ 0 & 0 & K_{\perp} \end{pmatrix} \tag{4.5}$$

Another effect of the presence of a large-scale magnetic field, that contributes to the transport of particles, is the existence of curvature and gradient drifts. Curvature drifts result from the centrifugal force a particle experiences when traveling along a curved magnetic field. Gradient drifts are a consequence of changes in the particle gyroradius during one gyration, due to changes in the magnetic field strength. As shown by Parker [1957][25], for an isotropic particle distribution, or for one with at most a first-order anisotropy (i.e. weakly anistropic), the combined gradient and curvature drift velocity of the distribution is given by

$$\langle \vec{v_{dr}} \rangle = \frac{\beta R}{3} \nabla \times \frac{\vec{B}}{B^2} \tag{4.6}$$

A further simplification results from a mathematical trick, which consists in formulating the drift term as an antisymmetric element of the diffusion tensor. Defining the drift coefficient

$$K_A = \frac{\beta R}{3B} \tag{4.7}$$

so that

$$\langle \vec{v_{dr}} \rangle = \nabla \times (K_A e_B) \tag{4.8}$$

with $e_B = \frac{\vec{B}}{B}$ and B the HMF expression.

Then, the combined diffusion tensor is

$$K_{i,j} = K^S_{i,j} + K^A_{i,j} = \begin{pmatrix} K_{\parallel} & 0 & 0 \\ 0 & K_{\perp} & K_A \\ 0 & -K_A & K_{\perp} \end{pmatrix} \tag{4.9}$$

which includes all the diffusive and drift terms, that can now be contracted in one single term in the transport equation $K \cdot \nabla f$.

The diffusion tensor 4.9 is written in a coordinate system connected to the magnetic field. This coordinate system will be called the *magnetic coordinate system.*

In this system (fig. 4.2), there is one axis $e_{\parallel}$, parallel to the average magnetic field in the $r\phi$ - plane, a second axis e_1 in the polar direction e_θ, and a third one e_2 also in the $r\phi$ - plane .

$$e_{\parallel} = \cos\Psi e_r - \sin\Psi e_\phi \tag{4.10}$$

$$e_1 = e_\theta \tag{4.11}$$

$$e_2 = e_{\parallel} \times e_1 = \sin\Psi e_r + \cos\Psi e_\theta \tag{4.12}$$

However, in equation 4.1, the diffusion tensor is written in spherical coordinates, and so a transformation matrix R must be applied

$$R = \begin{pmatrix} \cos\Psi & 0 & \sin\Psi \\ 0 & 1 & 0 \\ -\sin\Psi & 0 & \cos\Psi \end{pmatrix} \tag{4.13}$$

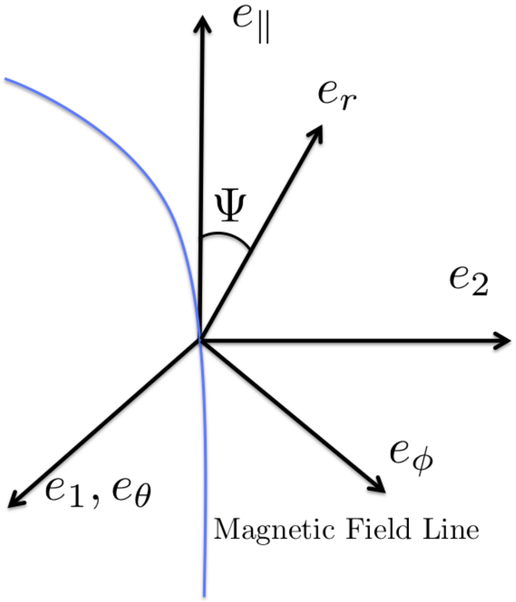

Figure 4.2: The magnetic coordinate system.

$$\begin{aligned}
\begin{pmatrix} K_{rr} & K_{r\theta} & K_{r\phi} \\ K_{\theta r} & K_{\theta\theta} & K_{\theta\phi} \\ K_{\phi r} & K_{\phi\theta} & K_{\phi\phi} \end{pmatrix} &= RKR^T \qquad (4.14) \\
&= \begin{pmatrix} \cos\Psi & 0 & \sin\Psi \\ 0 & 1 & 0 \\ -\sin\Psi & 0 & \cos\Psi \end{pmatrix} \begin{pmatrix} K_\parallel & 0 & 0 \\ 0 & K_\perp & K_A \\ 0 & -K_A & K_\perp \end{pmatrix} \begin{pmatrix} \cos\Psi & 0 & -\sin\Psi \\ 0 & 1 & 0 \\ \sin\Psi & 0 & \cos\Psi \end{pmatrix} \\
&= \begin{pmatrix} K_\parallel \cos^2\Psi + K_\perp \sin^2\Psi & -K_A \sin\Psi & (K_\perp - K_\parallel)\cos\Psi\sin\Psi \\ K_A \sin\Psi & K_\perp & K_A \cos\Psi \\ (K_\perp - K_\parallel)\cos\Psi\sin\Psi & -K_A\cos\Psi & K_\parallel \sin^2\Psi + K_\perp \cos^2\Psi \end{pmatrix}
\end{aligned}$$

4.2 Force Field Approximation

The transport equation can only be solved numerically. However, by doing many approximations, Gleeson and Axford (1968) [26] reduced the problem to a 1D spherically symmetric case that can be solved analytically. This is the so called force field approximation and today it is still the simplest and most used model for studying the effects of solar modulation.

It is assumed that:

- The Solar Wind is radially moving with constant speed V
- The diffusion tensor in eq. 4.5 is isotropic ($K \parallel = K \perp$) and constant with radius
- The density distribution function is spherically symmetric
- There is no drift (the antisymmetric part of K is neglected)
- The system is in quasi-stationary conditions $\frac{\partial f}{\partial t} = 0$

The steady-state condition means that the relaxation time of the distribution is short with respect to the solar cycle duration (11 years), so that one can assume that the time derivative of f is zero.

Using the previous assumptions, the majority of the terms in equation 4.1 vanish, and a simplified TPE is obtained

$$\frac{\partial f}{\partial t} = -V\frac{\partial f}{\partial r} + \frac{1}{r^2}\frac{\partial}{\partial r}\left(r^2 k\frac{\partial f}{\partial r}\right) + \frac{1}{r^2}\frac{\partial}{\partial r}(r^2 V)\frac{R}{3}\frac{\partial f}{\partial R} \tag{4.15}$$

where R is the particle rigidity and k the contracted diffusion tensor. It can be proved that, in case there are no sources or sinks at $r = 0$ and the system is in stationary conditions $\frac{\partial f}{\partial t} = 0$, it can be assumed that the diffusive flux is equal to the convective flux, for particles with energy above 400 MeV/nucleon [26] .

$$k\frac{\partial f}{\partial r} = Vf \tag{4.16}$$

Inserting 4.16 in 4.15, a new differential equation arises, called *force field approximation*

$$\frac{\partial f}{\partial r} + \frac{VR}{3k}\frac{\partial f}{\partial R} = 0 \tag{4.17}$$

The name "force field" comes from the fact that the second term has the dimensions of potential per unit lenght, or a field. The solutions of 4.17 are characteristic curves, where f is a constant in the (r,R) plane:

$$\frac{df}{dr} = \frac{\partial f}{\partial r} + \frac{\partial f}{\partial R}\frac{dR}{dr} \tag{4.18}$$

From 4.17 and 4.18 it can concluded that

$$\frac{dR}{dr} = \frac{VR}{3k} \tag{4.19}$$

Using $k = k_0\beta R$ from the QLT

$$\frac{dR}{dr} = \frac{VR}{3k_0\beta R} \tag{4.20}$$

and so

$$\beta dR = \frac{V}{3k_0}dr \tag{4.21}$$

The last expression can also be written in terms of E, since $E = \sqrt{p^2 + m^2}$ and $\beta dR = dE$.

$$dE = \frac{V}{3k_0}dr \tag{4.22}$$

Such expression has the following solution

$$E(r_H) - E(r) = \Phi_{SM}\frac{r_H - r}{r_H - 1} \tag{4.23}$$

where $E(r_H)$ and $E(r)$ are, respectively, the energies at the external boundary of the heliosphere and the observation point at Earth, and Φ_{SM} is

$$\Phi_{SM} = \int_{r_{1AU}}^{r_H} \frac{V}{3k_0}dr = \frac{V(r_H - 1)}{3k_0} \tag{4.24}$$

Since f is constant along the characteristic curve

$$f(1AU, E(r_H) - \Phi_{SM}) = f(r_H, E(r_H)) \tag{4.25}$$

it is possible to use the identity $p^2 = E^2 - m^2$ to calculate the differential flux $J_T = p^2 f$ that reaches Earth

$$J_T(1AU, E(r_H) - \Phi_{SM}) = J_T(r_H, E(r_H)) \frac{E(r_H)^2 - m^2}{E(1AU)^2 - m^2} \tag{4.26}$$

where the *Solar modulation parameter* ϕ_{SM} is defined by the relation $\Phi_{SM} = |Z|e\phi_{SM}$.

The Solar modulation parameter can be seen as an average potential, felt by a particle when crossing the heliosphere, causing an adiabatic deceleration[1].

$$E(1AU) = E(r_H) - |Z|e\phi_{SM} \tag{4.27}$$

The typical values for it range from 0.5 to 1.2 GeV. The flux at the boundaries of the outer heliosphere $J_T(r_H)$ can be taken as the local interstellar flux J_{LIS}.

Notice that originally it was assumed that the adiabatic energy losses were negligible when compared to the two spatial streaming terms. However, the Force Field formalism ends up with a parameter Φ_{SM}, which causes energy losses. This is due to the fact that the coefficient $\frac{VR}{3k}$ was interpreted as a field. There is no physical explanation that relates this field/energy loss to the true adiabatic energy loss, although it seems quite an unusual coincidence that this energy loss is a good approximation of the adiabatic energy losses in certain circumstances. In fact, Gleeson and Urch [1971] [27] showed that the force field energy loss is an upper limit of the true adiabatic loss.

In figure 4.3 it is shown the flux dependence on the parameter ϕ_{SM}, and in figure 4.4 it is possible to see how does the ϕ_{SM} changes within one Solar cycle (the parameter was obtained using the NM network data).

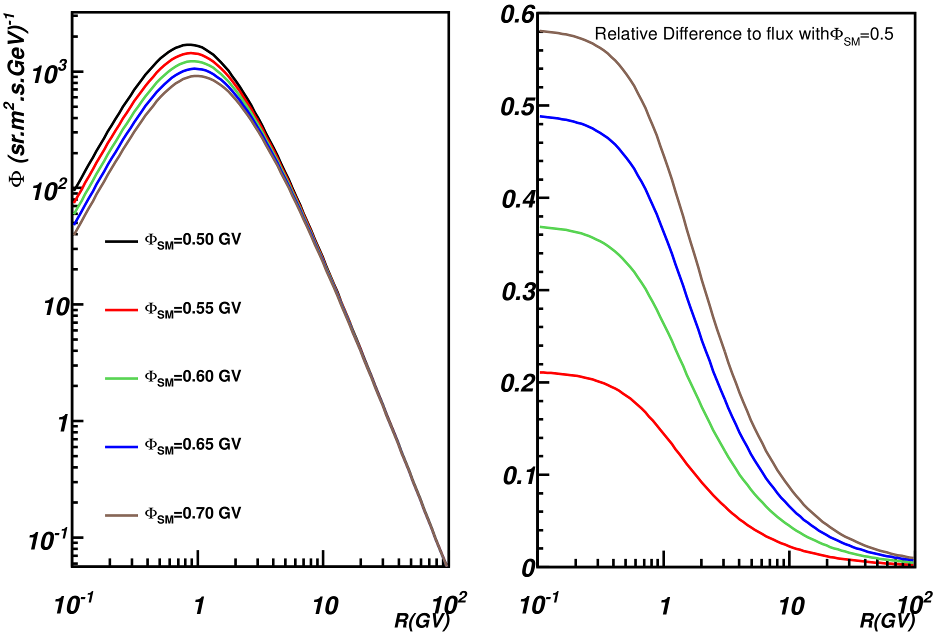

Figure 4.3: Sensibility of the flux for different Solar modulation parameters (LIS: Usoskin).

---

[1] The parameter can only be seen as an energy loss because $k \propto R$.

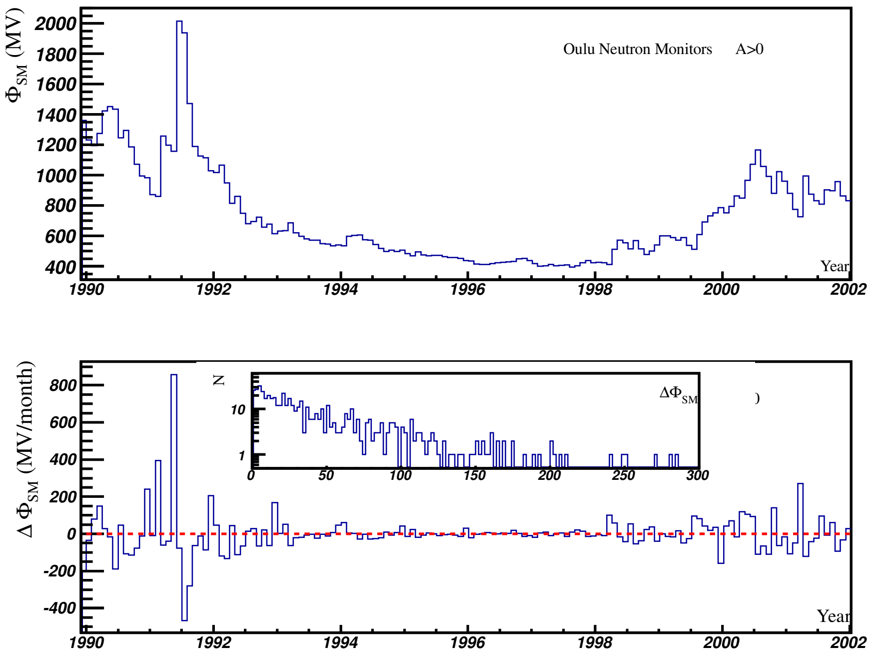

Figure 4.4: Top plot: Solar modulation parameter from 1990 to 2002 (NM network). Bottom plot: Monthly variations of ϕ_{SM} and respective distribution. Next to a Solar maximum, the variations of the Solar modulation parameter can be very high (few hundred MV per month).

4.3 The LIS Spectra

The interstellar flux is quite peculiar, since it has never been directly measured before. In fact, in the 15^{th} of June 2012, NASA announced that Voyager 1, launched in 1977, was entering the interstellar space at a distance where radio signals from the craft required 16 hours and 38 minutes to reach the antennas of NASA's Deep Space Network. Some of the detectors inside Voyager 1 are still active and one of them is even responsible for measuring fluxes of CRs. The fluxes detected, although restricted to a short energy range, will give a first experimental hint about the shape of the LIS spectra.

The absence of experimental data about the Local Interstellar Flux (LIS) spectra didn't stop physicists from making predictions about its structure. Many of these predictions were done using Monte Carlo simulations, such as the Monte Carlo Diffusion Model (MCDM) and other GCR propagation models, such as the one from Moskalenko et al.

As seen in the last section, the Force Field approximation depends on the choice of the interstellar flux, J_{LIS}. The following proton LIS fluxes (published in the literature) will be analyzed in order to understand the influence of a specific LIS flux on the Solar modulation parameter [33]. For the next parametrizations, the proton flux will be given in particles per m^2 s sr (GeV/nucleon), T represents the kinetic energy in GeV/nucleon and m the rest mass in GeV.

Usoskin et al. (2005) parametrization [28]

$$J_{USO5} = \frac{a}{b[T(T+2m)]^{1.39} + c[T(T+2m)]^{0.135}} \tag{4.28}$$

with $a = 4.157 \times 10^5$, $b = 21.9$ and $c = 10.6$

Garcia-Munoz et al. (1975) parametrization [29]

$$J_{GM75} = a[10^3 T + be^{cT}]^{-2.65} \tag{4.29}$$

with $a = 9.9 \times 10^{11}$, $b = 780$, and $c = -0.25$

Webber and Higbie (2003) parametrization [30]

$$J_{WH03} = \frac{10^3}{aT^{2.8} + bT^{1.58} + cT^{0.26}} \tag{4.30}$$

with $a = 4.75 \times 10^{-2}$, $b = 0.278$ and $c = 5.62 \times 10^{-2}$

Langner et al. (2003) parametrization [31]

$$J_{LA03} = \begin{cases} 10^3 exp(a - b\ln^2(10^3T) + \ln 10^3T - d\sqrt{10^3T}) & \text{if } T \geq 1\text{GeV/nucl} \\ exp(e - f\ln(10^3T) + \frac{g}{T}) & \text{if } T < 1\text{GeV/nucl} \end{cases} \tag{4.31}$$

with $a = 0.823$, $b = 0.08$, $c = 1.105$, $d = 9.202 \times 10^{-2}$, $e = 22.976$, $f = 2.86$ and $g = 1.5$.

Webber and Higbie (2009) parametrization [32]

$$J_{WH09} = 10^3 exp[a + b\ln^2(\ln(10^3T)) + c\sqrt{\ln(10^3T)} + d\ln^{-1}(10^3T) + e\ln^{-2}(10^3T)] \tag{4.32}$$

For $T < 1$GeV/nucl the parameters are $a = -124.5$, $b = -51.8$, $c = 131.6$, $d = -241.7$, $e = 376.7$, whereas for $T \geq 1$GeV/nucl, $a = 0$, $b = -51.7$, $c = 103.6$, $d = -709.7$ and $e = 1161.6$.

In figure 4.5 , all the above LIS fluxes are ploted as a function of the kinetic energy. As can be seen in the ratio plot, the difference between some of the fluxes is quite significant in the low energy region, whereas in the high energy region the agreement is substancially better. Dispite the differences, all the LIS fluxes can parametrize the flux in the vicinity of the Earth by using a modulation parameter - ϕ_{SM}. As shown by Herbst and Heber [33], all the LIS fluxes can represent fairly well the modulated flux with their individual modulation parameter. It is possible to find relations between all these model-dependent ϕ_{SM}, which was firstly done by Usoskin et al [2005] [28], who found a set of linear relations between the modulation parameters.

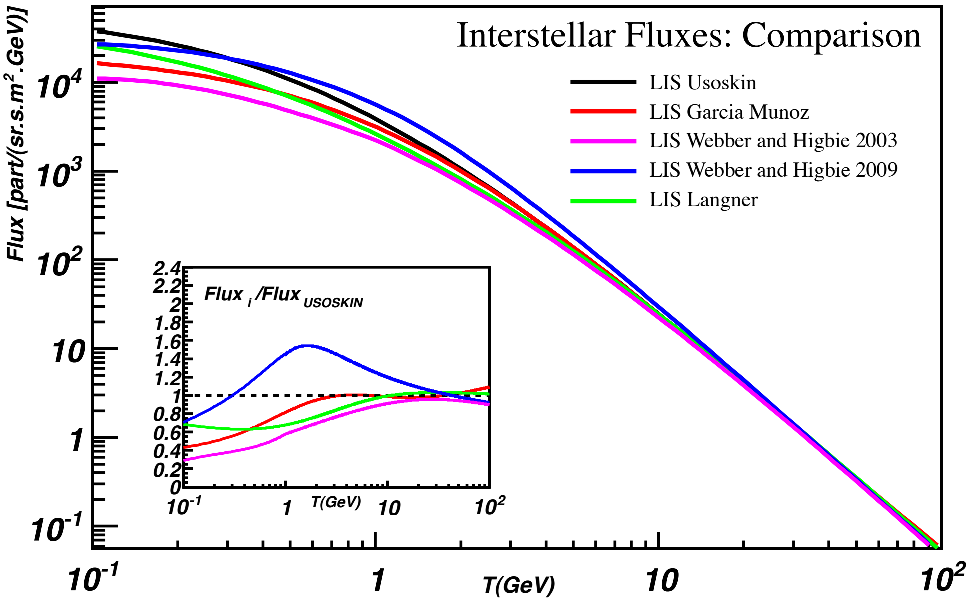

Figure 4.5: LIS proton fluxes as a function of energy. The sub-plot is the ratio between each of the J_{LIS} proton fluxes and J_{USO5}.

4.4 The 1D numerical solution

In the 1D numerical solution, the assumptions are the same as in the Force Field approximation, except for the fact that the adiabatic energy losses are kept, i.e, equation 4.16 is not used, and the Solar Wind speed can be space dependent.

The objective is to solve 4.15 and determine f in the region $r_0 \leq r \leq r_H$, where r_H is the outer boundary of the heliosphere. The functions $V(r)$, $k(r,T)$ and also the unmodulated spectrum at the boundary of the heliosphere, are known.

Since 4.15 is a parabolic Partial Differential Equation (PDE) that is second order in space and only first order in energy - there should exist two boundary conditions and one initial condition. The first boundary condition is at r_0 (Sun's radius), where the absence of any sources or sinks is assumed, since only GCR are being concerned. Mathematically speaking, this is assured by requiring that the differential current density - $\vec{S}$ in equation 2.56 vanishes at the origin.

$$\vec{S} = 4\pi p^2 \left(CV_{SW} - k\frac{\partial f}{\partial r} \right) \tag{4.33}$$

One way of accomplishing this requirement is if

$$V_{SW}|_{r=r_0} = 0 \tag{4.34}$$

$$\left.\frac{\partial f}{\partial r}\right|_{r=r_0} = 0 \tag{4.35}$$

The other boundary condition is just requiring that the flux of GCR at the boundary of the heliosphere is equal to the interstellar flux

$$J_T\Big|_{r=r_H} = p^2 f = J_{LIS} \tag{4.36}$$

The initial condition results from the fact that at sufficient high energies, the flux inside the heliosphere is equal to the interstellar flux.

$$J_T(r,p') = J_{LIS}(p') \text{ for all } r_0 < \text{r} < r_H \tag{4.37}$$

The general method to solve this equation is using finite differences. The domain will be divided in a rectangular grid, with r ranging from r_0 to r_H and $\ln p$ ranging from $\ln p_{min}$ to $\ln p_{max}$.

$$r = r_0 + ih \tag{4.38}$$

$$\ln p = \ln p_{min} + nk \tag{4.39}$$

It begans with the initial condition at $\ln p_{max}$ and then proceeds to lower energies in a iterative way.

For the finite difference treatment it is convinient to rewrite the transport equation 4.15 in the form

$$a\frac{\partial^2 f}{\partial r^2} + b\frac{\partial f}{\partial r} + c\frac{\partial f}{\partial \ln p} = 0 \tag{4.40}$$

After some algebra, it is possible to obtain some expressions for the coefficients a,b and c:

$$a = k \tag{4.41}$$

$$b = -V + \frac{2k}{r} + \frac{\partial k}{\partial r} \tag{4.42}$$

$$c = \frac{2}{3}\frac{V}{r} + \frac{1}{3}\frac{\partial V}{\partial r} \tag{4.43}$$

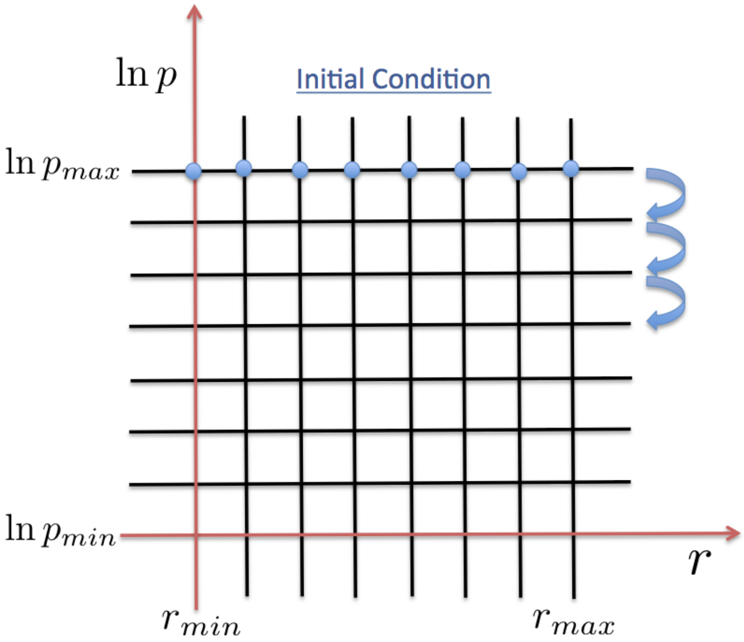

Figure 4.6: Rectangular grid.

When dealing with numerical problems, it is always recommendable to rewrite the equation in a non-dimensional form, by defining some typical momentum and space scales - P_S and L_S.

$$\tilde{r} = \frac{r}{L_S},\ \tilde{p} = \frac{p}{P_S} \tag{4.44}$$

From now on, the use of $\tilde{r}$ or $\tilde{p}$ will be avoided in order to simplify the notation, and every time an r or p appears, its meaning is the non-dimensional variable.

The next step - and this is what makes this procedure a finite difference method - is to approximate the partial derivatives as differences in near grid points.

$$\begin{aligned} \frac{\partial f}{\partial \ln p} &= \frac{f_i^{n+1} - f_i^n}{k} \\ \frac{\partial f}{\partial r} &= \frac{f_{i+1}^{n+1} - f_{i-1}^{n+1}}{2h} \\ \frac{\partial^2 f}{\partial r^2} &= \frac{f_{i+1}^{n+1} - 2f_i^{n+1} + f_{i-1}^{n+1}}{h^2} \\ f_i^n &= f(r_{min} + ih, \ln p_{min} + nk) \end{aligned} \tag{4.45}$$

In the space direction, the differences have been centered about the point $(i, n+1)$ to give second order accuracy to the approximation. These expressions could then be substituted into the transport equation, giving the following solution

$$f_i^n = \left(-\frac{ka}{h^2} + \frac{kb}{2h}\right) f_{i-1}^{n+1} + \left(\frac{2kc}{h^2} + 1 - kc\right) f_i^{n+1} + \left(-\frac{ka}{h^2} - \frac{kb}{2h}\right) f_{i+1}^{n+1} \tag{4.46}$$

Now, it is possible to compute all the f_i^n from the f_i^{n+1} and obtain f for the entire grid. Note that at each iteration the boundary conditions must be verified.

The solution to this equation is second order accurate in space, but only first order accurate in $\ln p$, and very easy to implement. However there are some drawbacks, mainly because the numerical solution is unstable unless the ratio k/h^2 is sufficiently small. Instability means that small errors due, either to arithmetic inaccuracies, or to the approximate nature of the derivative expressions will tend to accumulate and grow as one proceeds rather than dampen out (see Lapidus and Pinder 1982 [36] for a careful discussion of stability issues).

The instability problem can be solved if an implicit finite difference scheme is used, in this case the Cranck Nicholson (CN) algorithm. The CN has the advantage of being unconditionally stable, regardless of the value of k/h^2, and also is second order accurate in both the space and momentum directions. The key difference in this kind of algorithm is that the partial derivatives are averages for momentum n and $n+1$:

$$\begin{aligned}
\frac{\partial f}{\partial \ln p} &= \frac{f_i^{n+1} - f_i^n}{k} \\
\frac{\partial f}{\partial r} &= \frac{f_{i+1}^{n+1} - f_{i-1}^{n+1} + f_{i+1}^n - f_{i-1}^n}{4h} \\
\frac{\partial^2 f}{\partial r^2} &= \frac{f_{i+1}^n - 2f_i^n + f_{i-1}^n + f_{i+1}^{n+1} - 2f_i^{n+1} + f_{i-1}^{n+1}}{2h^2}
\end{aligned} \tag{4.47}$$

Substituting the last expressions in the transport equation

$$\begin{aligned}
&\overbrace{\left(\frac{c}{k} + \frac{a}{h^2}\right)}^{B_i} f_i^n + \overbrace{\left(\frac{b}{4h} - \frac{a}{h^2}\right)}^{A_i} f_{i-1}^n + \overbrace{\left(-\frac{b}{4h} - \frac{a}{h^2}\right)}^{C_i} f_{i+1}^n = \\
&\underbrace{\left(\frac{c}{k} - \frac{a}{h^2}\right) f_i^{n+1} + \left(-\frac{b}{4h} + \frac{a}{h^2}\right) f_{i-1}^{n+1} + \left(\frac{b}{4h} + \frac{a}{h^2}\right) f_{i+1}^{n+1}}_{D_i}
\end{aligned} \tag{4.48}$$

The f_i^n cannot be calculated as a simple linear combination of f_i^{n+1}, but are rather the solution of a system of linear equations. This system forms a matrix with a particular shape

$$\begin{pmatrix}
B_0 & C_0 & 0 & 0 & 0 & \cdots & 0 \\
A_1 & B_1 & C_1 & 0 & 0 & \cdots & 0 \\
0 & A_2 & B_2 & C_2 & 0 & \cdots & 0 \\
\vdots & \ddots & \ddots & \ddots & 0 & \cdots & 0 \\
0 & \cdots & \cdots & \cdots & 0 & A_I & B_I
\end{pmatrix}
\begin{pmatrix} f_0^n \\ f_1^n \\ f_2^n \\ \vdots \\ f_I^n \end{pmatrix}
=
\begin{pmatrix} D_0 \\ D_1 \\ D_2 \\ \vdots \\ D_I \end{pmatrix}$$

After inverting this matrix, the expression for f^n at all space points is obtained. Repeating the procedure several times it is possible to determine f for all grid points.

4.5 Force Field and 1D comparison

The purpose of this section is to compare the Force Field and the 1D solutions and see how they differ. To do so, the data from the AMS-01 flight and from IMP 1987 and 1997 was used.

The GCR LIS fluxes used were the ones from Webber and Lockwood [2001] [37]

$$J_{LIS}(H) = \frac{21.1(10^3T)^{-2.8}}{1 + 5.85(10^3T)^{-1.22} + 1.18(10^3T)^{-2.54}} \tag{4.49}$$

$$J_{LIS}(He) = \frac{1.075(10^3T)^{-2.8}}{1 + 3.91(10^3T)^{-1.09} + 0.9(10^3T)^{-2.54}} \tag{4.50}$$

in particles/m^2.sr.s.MeV and T is the kinetic energy in GeV.

The value used for the boundary of the Heliosphere was $r_H = 90$ AU, the diffusion coefficient and the solar wind radial velocity were set to

Table 4.1: Solar Wind and diffusion coefficient for AMS-01, IMP87, IMP97

Variable	AMS-02	IMP87	IMP97
$\mathrm{k_0[cm^2/s]}$	3.6×10^{22}	4.38×10^{22}	4.38×10^{22}
$\mathrm{V_0[km/s]}$	430	400	400

For the 1D solution, the Solar Wind velocity expression used was

$$V(r) = V_0(1 - e^{-13r}) \tag{4.51}$$

which is in accord with experimental measurements of the Solar Wind velocity [49]

For the IMP87 and IMP97, the fluxes are calculated at 1,20,60 and 80 AU (fig. 5.7), and are offset by factors of $\sqrt{10}$, so that the lines can be clearly visible. The first aspect to notice in fig. 5.7 is that, both the 1D and the Force Field solutions (although not considering drift terms), can fit reasonably well experimental data in solar minimum periods with opposite drift states. It is also evident that the Force Field solution diverges from the 1D solution at low energies (this phenomenon gets worse as the distance increases), proving that the energy losses estimated by the Solar modulation parameter are not the true adiabatic losses.

Another quantity that was also calculated for the two solutions was the radial intensity gradient, defined as

$$g_r = \frac{1}{J_T}\frac{\partial J_T}{\partial r} \tag{4.52}$$

Figures 4.8(a) and 4.8(b) show averages of g_r

$$g_r \approx \frac{\ln(J_{T1}/J_{T2})}{r_2 - r_1} \tag{4.53}$$

for four different space intervals: [1;20] AU, [20;40] AU, [40;60] AU and [60;80] AU. The quantity g_r gives information about flux variations with distance in different regions. The full line solutions in figure 4.8 indicate the well-known behavior that the gradients peak between 20 and 200 MeV, and that they recede to zero at low energies due to adiabatic energy losses. The dashed lines are the force field gradients, which show again that the true adiabatic energy losses are not being taken into account.

Figure 4.9 shows that it is difficult to distinguish between the Force Field and 1D numerical solution in the rigidity region covered by the AMS-01 experiment. As the AMS-02 detector operates in approximately the same rigidity region as AMS-01, it will also be hard to see any discrepancies between the Force Field and 1D solutions using the AMS-02 data, even with the huge amount of statistics.

The Force Field and the 1D are both approximate solutions of the transport equation. They assume that there is no dependence of the flux on the θ and ϕ coordinates, disregarding all the effects related, for instance, with the rotation of the Sun. This of course leads to the neglection of the HMF and the HCS structures and the drift terms.

For this reason, in these kind of models, it only makes sense to study variations on a monthly basis (approximately over one Solar rotation ~ 27 days).

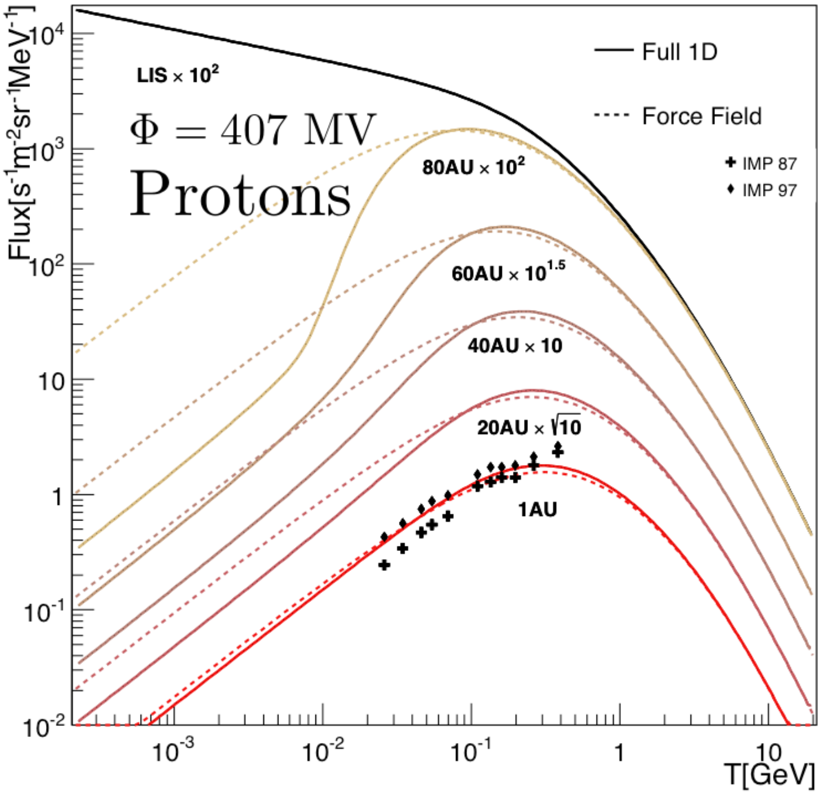

(a)

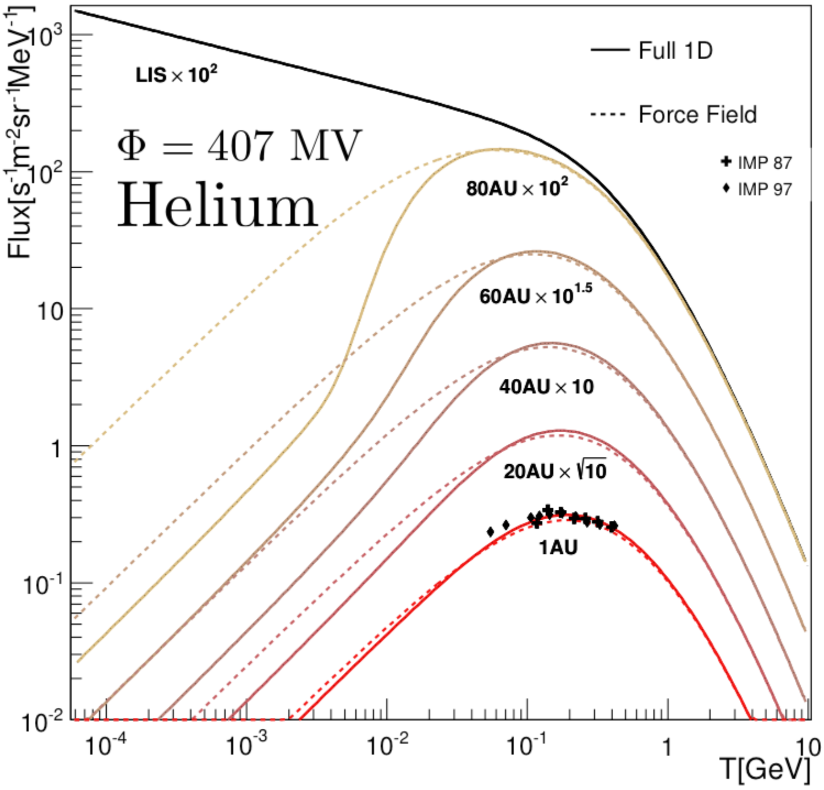

(b)

Figure 4.7: a) Proton fluxes at various distances from the Sun . b) Helium fluxes at various distances from the Sun. IMP data are from Goddard Medium Energy Detector (MED) (P.I.: R. E. McGuire).

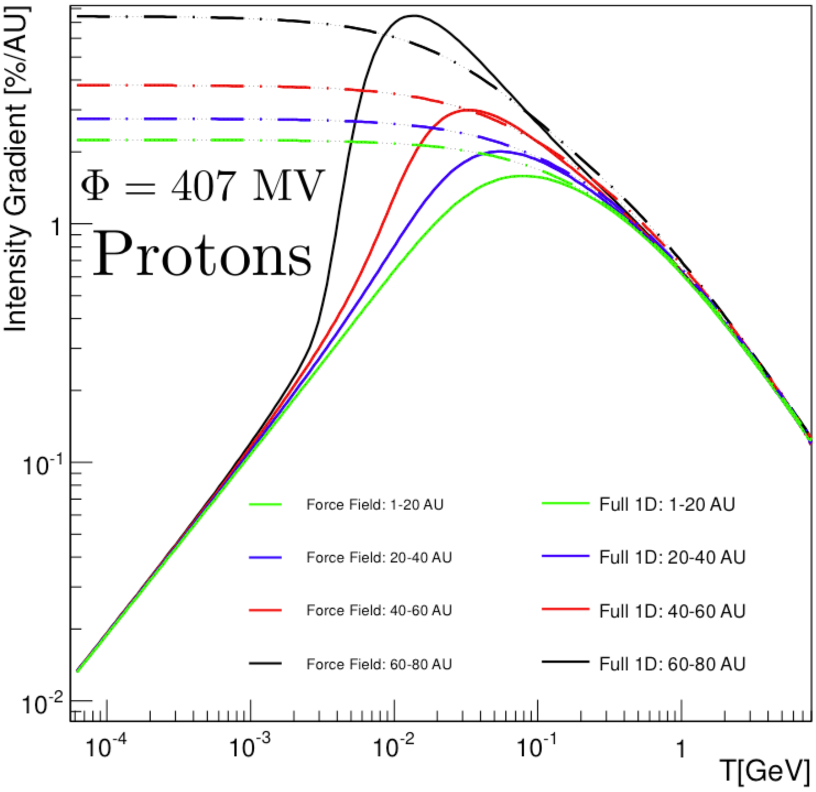

(a)

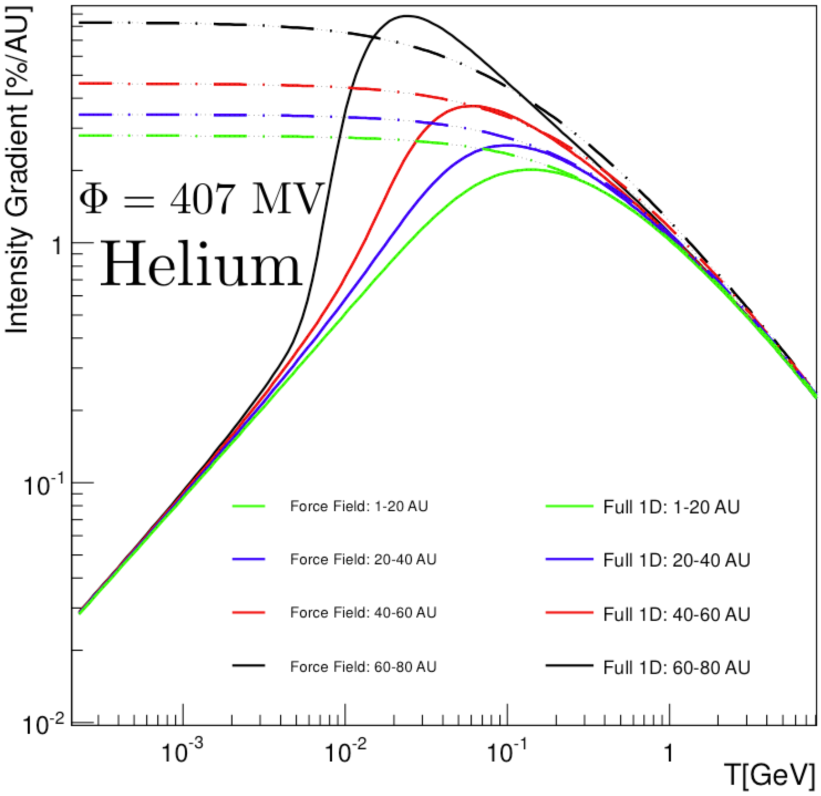

(b)

Figure 4.8: a) Radial Intensity Gradients for Protons at various distances from the Sun . b) Radial Intensity Gradients for Helium at various distances from the Sun. Experimental Data from IMP 1987 and 1997

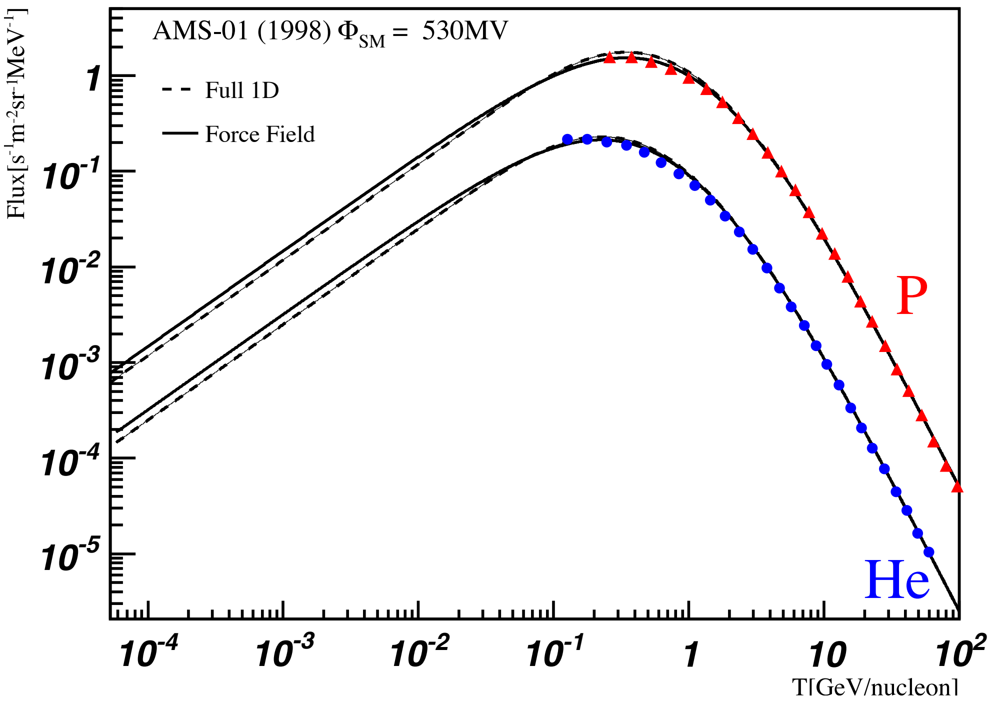

(a)

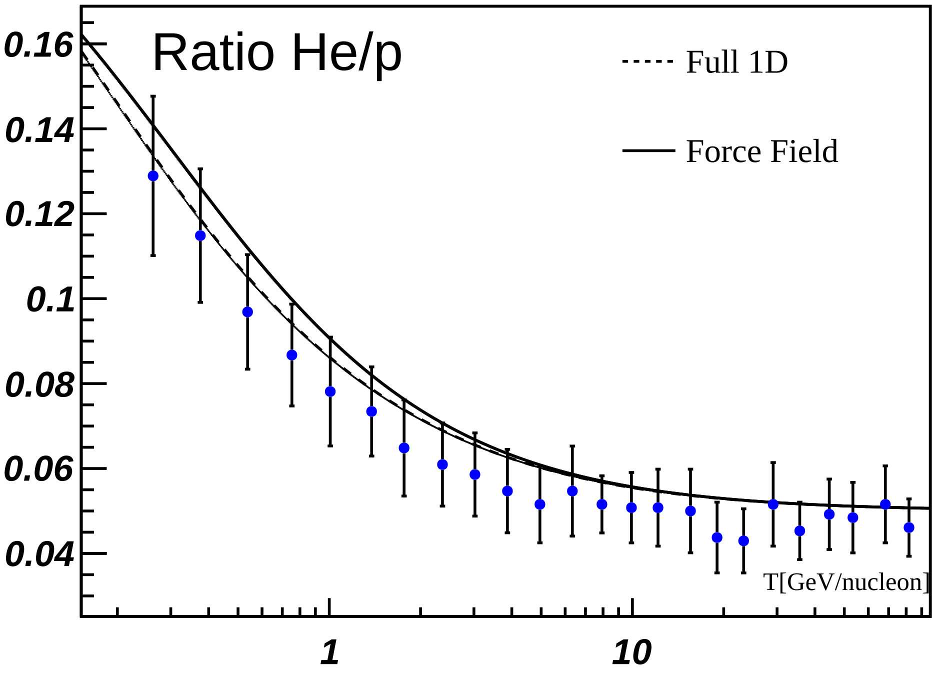

(b)

Figure 4.9: a) Proton and Helium calculated with Force Field and 1D . b) Ratio p/He calculated with Force Field and 1D. Experimental points from AMS-01 [34] [35]

4.6 The 2D numerical solution

If in equation 4.1, azimuthal symmetry is assumed ($\partial/\partial\phi$=0), the new expression for the TPE is

$$\begin{aligned}
\frac{\partial f}{\partial t} &= \overbrace{\frac{1}{r^2}\frac{\partial}{\partial r}(r^2K_{rr})\frac{\partial f}{\partial r}+\frac{1}{r^2\sin\theta}\frac{\partial}{\partial\theta}(K_{\theta\theta}\sin\theta)\frac{\partial f}{\partial\theta}}^{diffusion} \\
&+ \overbrace{K_{rr}\frac{\partial^2 f}{\partial r^2}+\frac{K_{\theta\theta}}{r^2}\frac{\partial^2 f}{\partial\theta^2}}^{diffusion}+\overbrace{\frac{1}{r^2}\frac{\partial}{\partial r}(rK_{r\theta})\frac{\partial f}{\partial\theta}+\frac{1}{r\sin\theta}\frac{\partial}{\partial\theta}(K_{\theta r}\sin\theta)\frac{\partial f}{\partial r}}^{drifts} \\
&- \overbrace{V\frac{\partial f}{\partial r}}^{convection}+\overbrace{\frac{1}{3r^2}\frac{1}{\partial r}(r^2V)\frac{\partial f}{\partial\ln p}}^{adiabatic\ losses}
\end{aligned} \tag{4.54}$$

The drift terms can be written in terms of the drift velocities $\vec{v}_{dr}=\nabla\times(K_Ae_B)$

$$\langle v_{dr}\rangle_r = -sign(qA)\frac{1}{r\sin\theta}\frac{\partial}{\partial\theta}(K_{\theta r}\sin\theta) \tag{4.55}$$

$$\langle v_{dr}\rangle_\theta = -sign(qA)\frac{1}{r^2}\frac{\partial}{\partial r}(rK_{r\theta}) \tag{4.56}$$

where $sign(qA)$ determines the drift direction of the particle in the heliosphere (q is the charge and A is the magnetic field polarity).

The diffusion coefficients $K_{rr}=K_\parallel\cos^2\Psi+K_\perp\sin^2\Psi$ and $K_{\theta\theta}=K_\perp$ (as deduced in the transformation 4.15) are just the diagonal elements of the diffusion tensor, where $K_\perp$ and $K_\parallel$ represent, respectively, the diffusion coefficients perpendicular and parallel to the average HMF. Ψ is the angle between the radial and mean HMF directions. The coefficients $K_{r\theta}$ and $K_{\theta r}$ are the off diagonal elements and can be expressed as $K_{r\theta}=-K_{\theta r}=-K_A\sin\Psi$, where K_A is the antisymmetric element of the diffusion tensor, describing the effects of particle gradient and curvature drifts in the large-scale HMF.

The drift velocity, as mentioned in equation 4.8 is

$$\begin{aligned}
\vec{v}_{dr} &= \nabla\times(K_Ae_B[1-2H(\theta-\theta')]) \\
&= \nabla\times(K_Ae_B)[1-2H(\theta-\theta')]+2\delta(\theta-\theta')K_Ae_B\times\nabla(\theta-\theta') \\
&= \vec{v}_D[1-2H(\theta-\theta')]+\vec{v}_{HCS}\delta(\theta-\theta')
\end{aligned} \tag{4.57}$$

where $[1-2H(\theta-\theta')]$ was introduced to take into account the fact that the field changes polarity when crossing the HCS, e_B is the HMF direction and θ' is just the HCS expression (equation 2.25).

The first term in the last equation describes the gradient and curvature drifts, which are caused by the global magnetic field, and the second term describes the drifts along the HCS. A particle in an external magnetic field $\vec{B}$ gyrates in a plane perpendicular to the field direction. If a particle is moving within two gyroradii from HCS it will be affected by it. The effect is showed in figure 4.10, for a flat HCS.

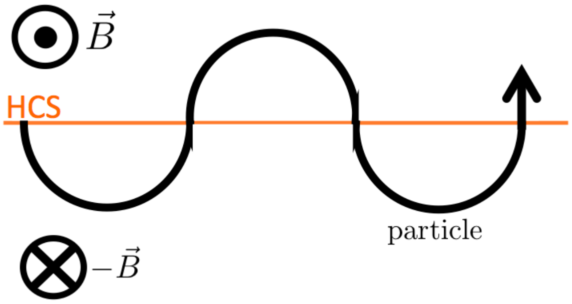

Figure 4.10: An illustration of the trajectory of a particle along a flat HCS.The wavy curves represent the trajectory of the particle.

In order to separate the effect of the HCS drift from other drift effects at a certain latitude, it is necessary to define the region swept out by particles drifting along the HCS in one solar rotation. This region (figure 4.11) is known as the HCS region and is defined by the latitude θ such that,

$$\frac{\pi}{2} - \alpha - \Delta\theta_{HCS} < \theta < \frac{\pi}{2} + \alpha + \Delta\theta_{HCS} \tag{4.58}$$

where α is the tilt angle and $\Delta\theta_{HCS}$ is the angle spanned by two gyroradii of a particle at a radial distance r from the Sun, i.e.$\Delta\theta_{HCS} = \sin^{-1}(r_g/r)$, or $\Delta\theta_{HCS} = 2r_g/r$ when the gyroradius $r_g << r$.

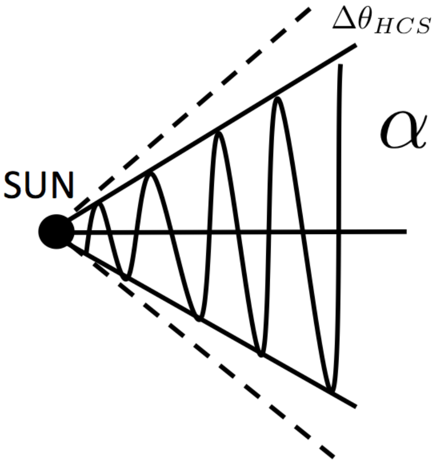

Figure 4.11: Scheme of the HCS region.

The expressions $\vec{v}_D = \nabla \times (K_A e_B)$ and $\vec{v}_{HCS} = 2K_A e_B \times \nabla(\theta - \theta')$, can be computed, since K_A, e_B and θ' are known. The projections of $\vec{v}_D$ and $\vec{v}_{HCS}$ in the meridional plane are shown in figure 4.12, for positive charges and for $A > 0$ and $A < 0$.

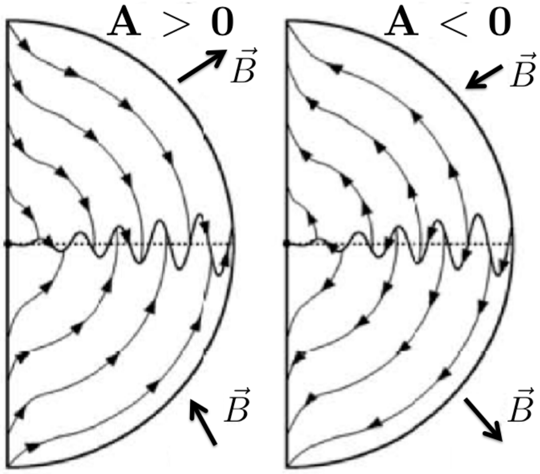

Figure 4.12: The projections of drift directions onto the meridional plane for positively-charged particles in a Parker HMF during an A>0 and A<0 epoch [47].

Structures like the HCS depend on r, θ and ϕ, which means they are three dimensional. Potgieter and Moraal [48] showed that a way of including the HCS drift effects in a 2D model was to assume an antisymmetric diffusion coefficient of the form $K'_A = K_A\, F(\theta)$, with

$$F(\theta) = \begin{cases} (1/a)\arctan(1 - 2\theta/\pi)\tan a & \text{if } c < \pi/2 \\ 1 - 2H[\theta - \pi/2] & \text{if } c = \pi/2 \end{cases} \tag{4.59}$$

$$a = arcos\left(\frac{\pi}{2c} - 1\right) \tag{4.60}$$

$$c = \frac{\pi}{2} - \frac{\sin(\alpha + \Delta\theta_{HCS})}{2} \tag{4.61}$$

The resulting drift velocity in a 2D model is

$$\vec{v}_{dr} = F(\theta)\nabla \times (K_A e_B) + \frac{\partial F}{\partial \theta}\frac{K_A}{r} e_\theta \times e_B \tag{4.62}$$

The method that will be used to solve equation 4.54 is the Alternating Direction Implicit (ADI) method, in particular the Peaceman-Rachford scheme. The ADI method is an extension of the CN, used to solve the 1D TPE. It preserves the trigonal nature of the matrices to be inverted by employing an operator splitting technique that produces two independent differential equations.

In this particular case the equation has the form (assuming the steady state condition $\partial f/\partial t = 0$)

$$\frac{\partial f}{\partial \ln p} + L_r f + L_\theta f = 0 \tag{4.63}$$

with

$$L_r = a_1(r,\theta)\frac{\partial}{\partial r} + a_2(r,\theta)\frac{\partial}{\partial r^2} \tag{4.64}$$

$$L_\theta = b_1(r,\theta)\frac{\partial}{\partial \theta} + b_2(r,\theta)\frac{\partial}{\partial \theta^2} \tag{4.65}$$

L_θ and L_r are differential operators. In the 1D case, the way to solve the equation was to transform the domain in a rectangular grid (r, $\ln p$) and use finite differences. The problem is that in the 2D case there are three variables $r \in [\ln p_{min}, \ln p_{max}]$, $r \in [r_0, r_H]$ and $\theta \in [0, \pi/2]$ in the equation. What the ADI does is to solve the equation in two steps.

$$\begin{aligned} &\textbf{1.} \quad \frac{f^n - f^{n-1/2}}{(\Delta \ln p)/2} + \mathfrak{L}_r f^{n-1/2} + \mathfrak{L}_\theta f^n = 0 \\ &\textbf{2.} \quad \frac{f^{n-1/2} - f^{n-1}}{(\Delta \ln p)/2} + \mathfrak{L}_r f^{n-1/2} + \mathfrak{L}_\theta f^{n-1} = 0 \end{aligned} \tag{4.66}$$

where $\mathfrak{L}_r$ and $\mathfrak{L}_\theta$ are now the discretized operators L_θ and L_r, i. e., written using finite differences. The first step is used to solve implicitly in r for all θ, in order to obtain a solution at a half momentum step $f^{n-1/2}$, using f^n as an initial condition. A second solution is now obtained by solving implicitly in θ for all r to get the solution at a full momentum step f^{n-1}, by using the previously calculated solution at half a momentum step $f^{n-1/2}$. That is why it is called an alternating method, because in the first step the equation is solved implicitly for r and in the second step is solved implicitly for θ.

Just like in the 1D case, it is important to assure that the boundary conditions are always being respected. In the 2D model, besides the boundary conditions at $r = r_0$ and $r = r_H$, there are two additional ones:

$$\left.\frac{\partial f}{\partial \theta}\right|_{\theta=0} = \left.\frac{\partial f}{\partial \theta}\right|_{\theta=\pi/2} = 0 \tag{4.67}$$

which result from the fact that the heliosphere is assumed to be symmetrical about the poles and the equatorial plane. Repeating the procedure in 4.66, it is possible to calculate f for all θ and r.

As can be easily seen, the complexity changes abruptly when considering two dimensions. The diffusion is now treated as a complex tensor, with symmetric components, accounting for the perpendicular and parallel diffusion, and antisymmetric components, responsible for the drifts. Some of these quantities, like $K_\perp$ are still not completely understood, which means that a lot of work is still needed to fully comprehend its effects on the flux. The purpose of this section was not to study in detail the 2D solution, but rather to give an outline on how to solve it. There are a lot of parameters that enter the 2D equation, which have to be carefully analyzed in order to understand its effects. The Peaceman-Rachford scheme, described above, was implemented using a C++ classes framework (integrated in the analysis sofware chain - **LxSoft**).

5

SOLAR MODULATION EFFECTS ON AMS-02 PROTON FLUXES

The first part of this chapter describe all the procedures related to the calculation of the primary proton flux. Protons correspond to approximately 90% of the 40 million events that reach the AMS-02 detector every day, and so, contamination from other species is not a major problem. Given that, all the particle selection procedures are more focused on having a high efficiency, rather than a perfectly clean sample.

The second part of this chapter is about the monitorization of Solar Events,a periodic survey of fluxes variations and the application of a Solar modulation model. The results are also compared with the NM network data.

5.1 Measuring Proton Fluxes

The flux of particles that reaches the detector are influenced by two physical phenomena: Solar Modulation and the Geomagnetic Cut-off. The goal is to select primary protons, i.e, protons with rigidity above the cut-off rigidity.

The flux of primary protons can be expressed by:

$$J_p(R) \quad = \quad \frac{1}{Acc(R)\Delta t(R)} \cdot \frac{\Delta N_p(R)}{\Delta R} \tag{5.1}$$

The various terms are:

- ΔN_p - The number of primary protons between [R;R+ΔR].
- ΔR - The width of the rigidity bin.
- Δt - The exposure time of the detector between [R;R+ΔR].
- *Acc* - The Acceptance of the detector as a function of rigidity (which includes the geometrical acceptance and the selection efficiencies)

5.1.1 Proton Selection

The main goal of the selection was to distinguish protons from the other particles that constitute the flux of cosmic rays, mainly heliums (11%) and electrons (2%) without reducing too much the proton sample, i.e., with high efficiency.

As seen in Chapter 3 some of the AMS-02 subdetectors, such as the TRD and the ECAL, were built to separate e^+/e^- from $p/\bar{p}$. However, there are some characteristics of these subdetectors, such as the low geometrical acceptance of the ECAL, that reduce dramatically the selection efficiencies, i.e, the number of protons in the sample, and so these detectors will not be used in the selection.

The proton selection was divided in two parts: **general data selection** and **particle selection**. The general data selection assured that the events analyzed passed the quality cuts necessary for a proper particle identification (analyzing the rigidity and velocity measurements). The particle selection was focused in selecting a specific particle, in this case the proton.

The data selection cuts (DS) were applied as follows:

DS1 *One particle and one track per event.*
The aim of this cut was to exclude events with multiple particles transversing the detector.

DS2 *One hit with X and Y coordinates per pair of inner Tracker planes (3/4, 5/6 and 7/8).*
This assures a minimal number of hits required for a good measurement of the rigidity in the Tracker. The rigidity is calculated interpolating the track.

DS3 $\chi^2_y < 10$.
Tracker track quality in the bending direction.

DS4 *At least one hit on every* TOF *plane (4/4)*

DS5 *Matching between the Tracker track and the* TOF *hits position.*
The fitted track was extrapolated to the TOF and the compatibility was checked by computing the distance between the trace and the TOF hits position.

DS6 $\chi^2_\beta < 4$.
β_{TOF} quality

DS7 $\beta > 0$.
This cut rejects all particles that entered the detector from the bottom position. The majority of these particles are secondaries, created below the detector via interactions of the primary particle with the atmosphere.

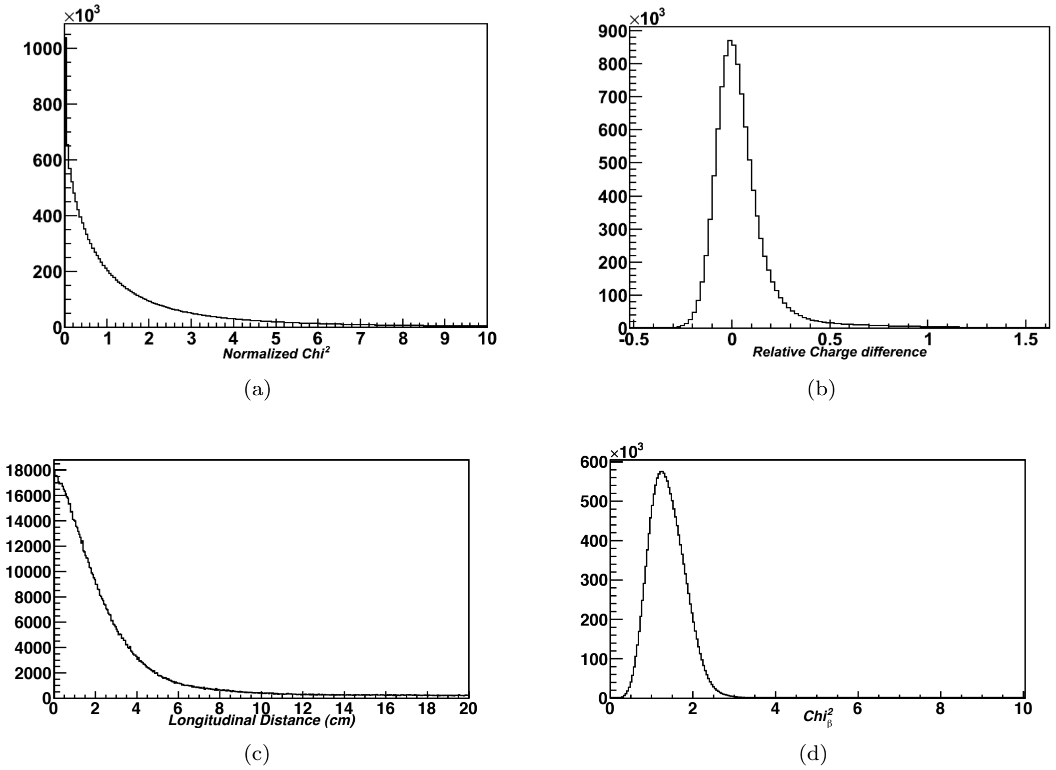

(a) (b)

(c) (d)

Figure 5.1: a) Normalized χ^2 in the bending direction. b) Distribution of the relative differences between TOF and TRK reconstructed charges. c) Distribution of longitudinal distance between TOF hits position and track, for bar 1 of layer 3. d) χ^2_β distribution. All these plots correspond to one day of data acquisition.

The Particle Selection cuts (PS) were based on the charge measurements given by the TOF and Tracker, and on the rigidity measurements given by the Tracker. In this case, for proton selection, the cuts were:

PS1 *Positive Rigidity.*
Choosing particles with positive charge.

PS2 *Charge Compatibility between* TOF *and Tracker (relative difference must be lower than* 30%*)*

PS3 *Q=1.*
Choosing particles with absolute charge equal to 1.

Table 5.1: Cuts efficiencies

Cut	average efficiency	Description
DS1	50%	$N_{part} = 1$ and $N_{TRK} = 1$
DS2	41%	Number of track hits
DS3	39%	Track Quality
DS4	37%	TOF hits
DS5	30%	Matching Tracker-TOF
DS6	28%	Velocity quality
DS7	26%	Downward particles
PS1	24%	Positive rigidity
PS2	20%	Charge compatibility Tracker-TOF
PS3	16%	Charge = 1

After these cuts, the sample was mainly constituted by particles with positive unit charge, but it was not a primary proton sample. In order to accomplish that, all the particles with rigidity below the cut-off rigidity were rejected.

Yet, the rejection of particles below the cut-off must be dealt with some precautions. As showed in section 2.5.4, the Stöermer cut-off rigidity depends not only on the detector position, but also on the direction of the particle. However, even if the particles direction, rigidity (R) and cut-off (R_{CUT}) are known, the inequality that tells if the particle is primary is not as simple as

$$R > R_{CUT} \tag{5.2}$$

This is due to the fact that Earth's magnetic field has a more complex shape than a dipole [1], and so the formula 2.67 is not exact . As a consequence, for each position and incoming direction, a penumbra region is created. This penumbra region is bounded by two rigidity limits: R^U, above which all trajectories of the galactic particle are allowed, and a lower rigidity R^L, below which no trajectory of the galactic particle is allowed; the Stöermer cut-off rigidity R_{CUT} is a value between R^L and R^U. Figure 5.2 shows this concept for an arbitrary position and incoming direction of the galactic particle. Using numerical methods to solve the motion equation in the magnetic field, it is possible to back-trace a measured particle (of known rigidity and incoming direction). As can be seen there are regions below R_{CUT}, where the particle is galactic, and regions above the R_{CUT} is not galactic, which show the limitations of the Stöermer's formula.

---

[1] The Earth's magnetic field is usually expressed as a truncated series expansion whose coefficients are periodically measured - the International Geomagnetic Reference Field (IGRF)

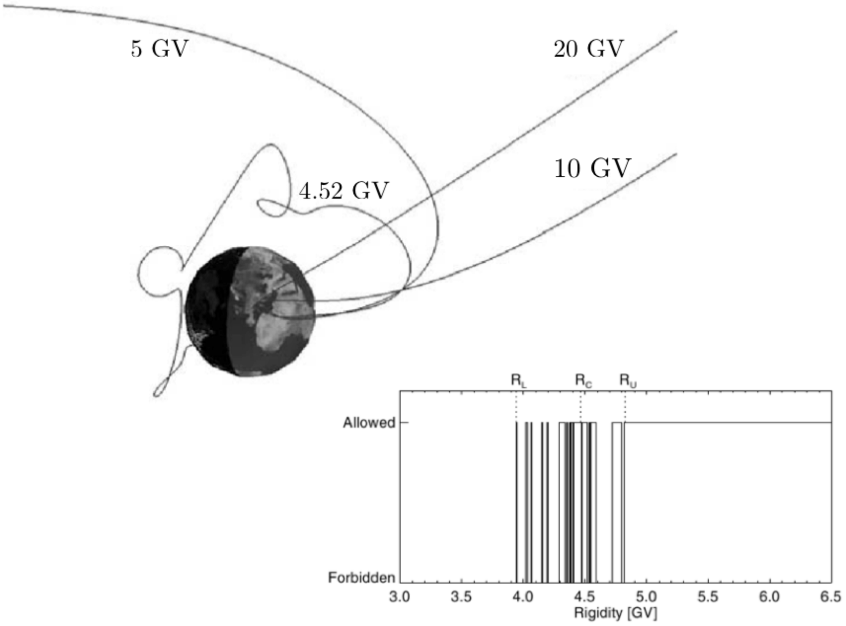

Figure 5.2: Schematic representation of the penumbra region [43] [51].

Additionally, Stöermer's formula shows that two particles, with the same rigidity, can be classified differently (primary or secondary), depending on their direction. So being, for each position of the detector in space, equation 2.67 says that there is not an unique cut-off rigidity but rather a rigidity interval $[R_{CUT}^{min}; R_{CUT}^{max}]$.

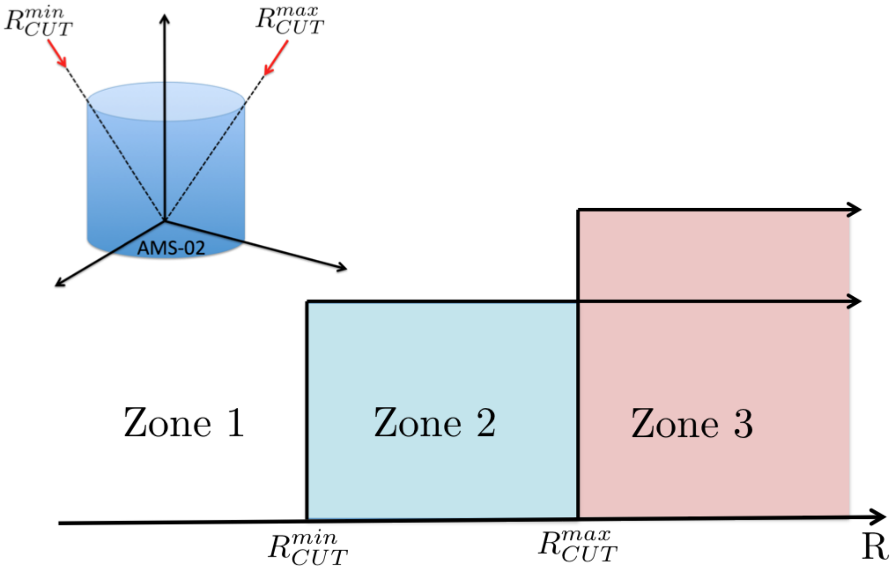

Figure 5.3: Schematic representation of the different regions created by the geomagnetic cut-off.

In figure 5.3, all particles falling into zone 1 are secondaries,whereas all particles inside zone 3 are primaries. However, for particles with rigidities between $[R_{CUT}^{min}; R_{CUT}^{max}]$ the distinction is not so obvious, because the cut-off depends on the direction.

Since between $[R^{min}_{CUT}; R^{max}_{CUT}]$ not all trajectories are allowed, the galactic protons are not isotropic in that region. It was therefore necessary to avoid it and only particles with rigidities above R^{max}_{CUT}, in a zone of rigidities where all detected particles are galactic, were selected. In order to stay clear from any penumbra effects, a "safe margin" was adopted and the decision about the origin of the particle was based on the inequality

$$R > C \cdot R^{max}_{CUT} \tag{5.3}$$

with C=1.3

Finally, a mass cut was applied to exclude particles with Q=1, other than protons, that were contaminating the sample. Figure 5.4 shows the mass plot, before and after the band cut. This cut was only effective for low energies where the $1/\beta$ curves of the particles are considerably different.

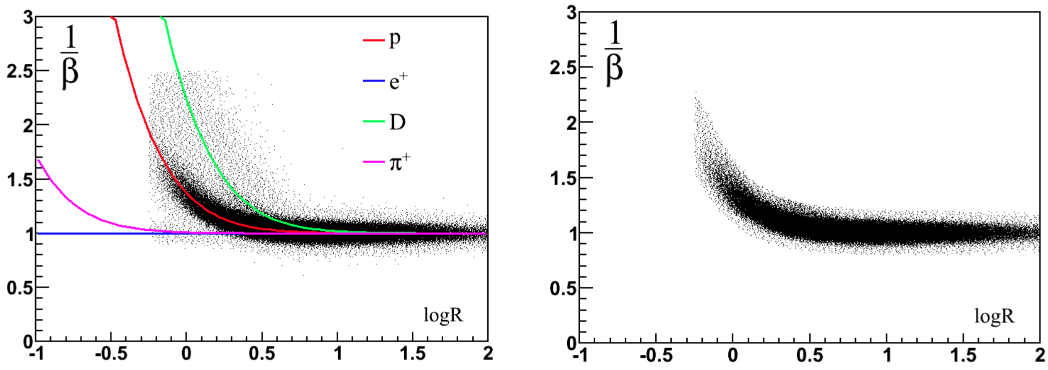

(a)

(b)

Figure 5.4: a)Inverse β versus momentum before the mass cut . b)Inverse β versus momentum after the mass cut .

5.1.2 Exposure Time and Livetime

The computation of the flux requires, as seen before, the calculation of the exposure time for each rigidity bin, i.e., the time the detector is "able" to measure particles in a certain rigidity interval. For instance, near the equator, the cut-off rigidity is around a few tens of GV, which doesn't allow particles to fill up low rigidity bins. As a consequence, the time is counted only for bins above the cut-off.

Using the same "safe" factor - C, the bin time is counted, if and only if

$$R^{min}_{bin} > C \cdot R^{max}_{CUT} \tag{5.4}$$

where R^{min}_{bin} is the lower boundary of the rigidity bin.

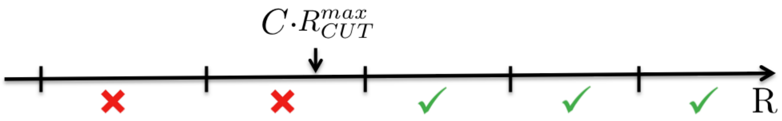

Figure 5.5: Schematic representation of exposure time counting.

Another important aspect regarding time counting is the livetime. By definition, dead time is the time required by the electronics and acquisition system of the apparatus to register each event. During this time (200 μs for the AMS-02 detector), the apparatus cannot register any particle reaching it.

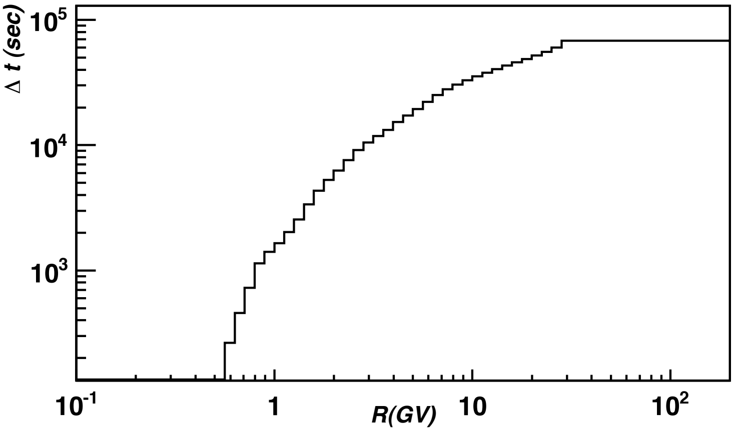

Figure 5.6: Exposure Time during one day of acquisition.For rigidities above ≈ 50 GV, the detector is always able to count times.

The payback is that the rate at which the events are reaching the detector, R_0, is not equal to the rate at which the events are being registered - R. Therefore, the number of events in a certain rigidity bin i must be corrected by the livetime

$$\Delta N_i = R_0 \cdot \Delta t_i = \frac{R}{L} \cdot \Delta t_i \tag{5.5}$$

where

$$L = \frac{R}{R_0} \tag{5.6}$$

is the livetime.

If the rates are very high, the livetime can be excessively low, and the detector "loses" a lot of events during the event processing time. In AMS-02, the highest rates (≈ 1500 Hz) occur at the poles and when the detector passes through the South Atlantic Anomaly (SAA)[2]. Figure 5.7(a) shows the livetime increasing with the geomagnetic latitude. All the events having livetimes lower than 0.65 were rejected. Figure 5.7(b) shows the orbit of the detector during one day and excluding the SAA.

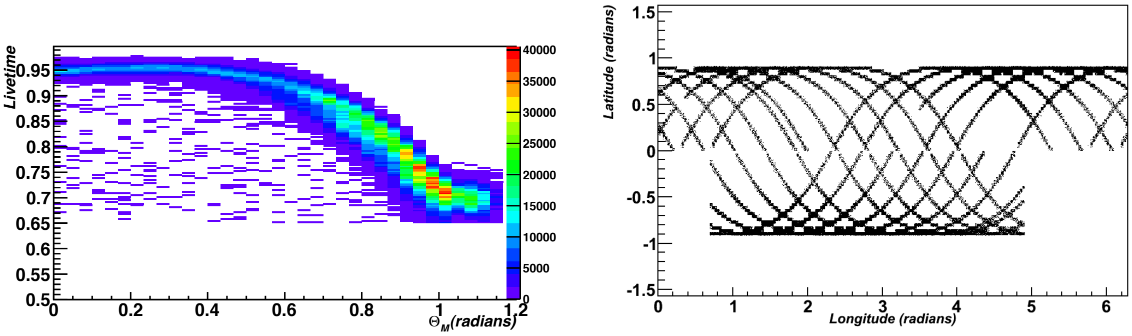

(a)

(b)

Figure 5.7: a)Livetime versus geomagnetic latitude for 1 day of events . b) Orbits for 1 day, excluding the SAA.

---

[2] The SAA is the area where the Earth's magnetic field has its lowest value, allowing that the inner Van Allen radiation belt comes closely to the Earth's surface. The effect is caused by the non-concentricity of the Earth's dipole.

5.1.3 Acceptance

The detector's acceptance was computed using a Monte Carlo proton sample. The acceptance can be grouped in one single expression, which includes the generation acceptance and the efficiencies

$$Acc(R) = Acc_0 \cdot \epsilon_{trigger}(R) \cdot \epsilon_{Sel}(R) \tag{5.7}$$

where Acc_0 is the generation acceptance, $\epsilon_{trigger}(R)$ is the trigger efficiency and $\epsilon_{Sel}(R)$ is the selection efficiency. Each set of selections for the flux sample under study, also called cuts, must be evaluated over a subset of events, representative of the galactic flux aiming to measure. This subset is called efficiency sample.

The efficiency of a generic set of selections is defined as:

$$\epsilon(R) = \frac{N(R)}{N_0(R)} \tag{5.8}$$

where $N_0(R)$ is the number of events distributed in rigidity in the efficiency sample, and $N(R)$ is the subset of events that passed the cuts.

The trigger efficiency is defined as the number of protons that passed the AMS-02 Level 1 trigger divided by number of generated protons. The Level 1 proton trigger consists of two conditions :

- *The particle must cross all the 4* TOF *planes.*
- *No* ACC *signal.*
  This rejects events having a particle interaction occurring inside the inner Tracker, which leads to a deficient rigidity measurement.

The selection efficiency is the ratio of particles that, having passed the trigger, passed all the data selection and particle selection cuts.

In the Monte Carlo, the detector is simulated inside a cube of $(3.9)^3$ m^3. The events are generated isotropically on the faces of the cube, and distributed uniformly in $\log p$. The generation acceptance in each face is:

$$Acc_0 = \int_S dS_\perp \int_\Omega d\Omega = S_0 \int_{cos\theta} \int_\phi \cos\theta \; d\cos\theta d\phi \tag{5.9}$$

Since the events are generated with a random $0<\phi<2\pi$ and $\cos\theta_{min} < \cos\theta < \cos\pi$, the last expression is just

$$Acc_0 = \pi S_0 (1 - \cos^2\theta_{min}) \tag{5.10}$$

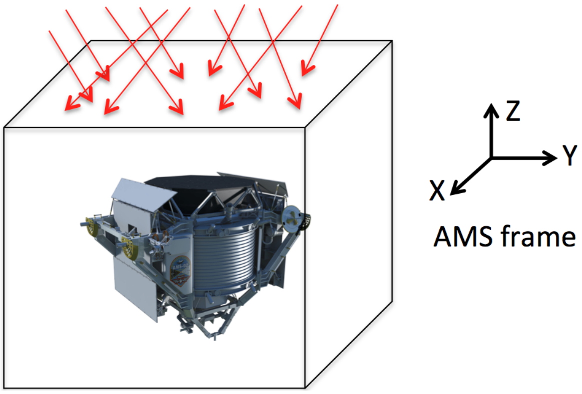

Figure 5.8: Schematic representation of the Monte Carlo generation method on the top face of the cube.

In this work, the acceptance was calculated using a sample of 6×10^6 protons, generated isotropically on the top face, and uniformly distributed in $\log p$ between 0.5 GV and 200 GV.

The acceptance after trigger and after selection, i.e,

$$Acc_{Trig}(R) = Acc_0 \cdot \epsilon_{trigger}(R) \tag{5.11}$$

$$Acc(R) = Acc_0 \cdot \epsilon_{trigger}(R) \cdot \epsilon_{Sel}(R) \tag{5.12}$$

are ploted in figure 5.9.

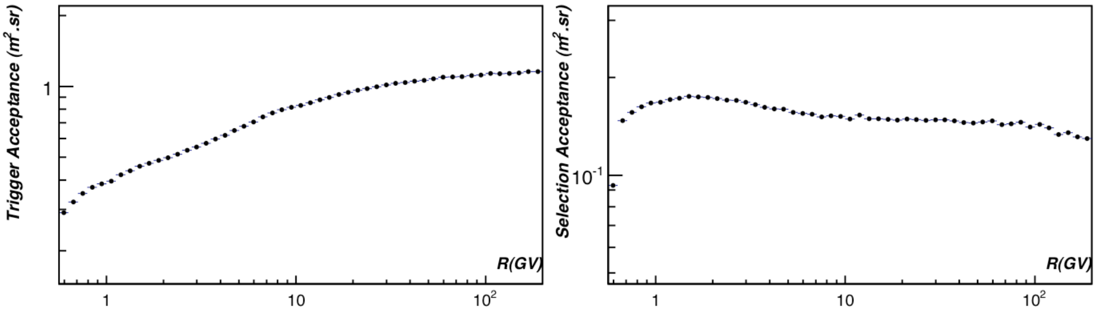

Figure 5.9: Selection and Trigger Acceptances.

5.1.4 Results

All the steps towards the determination of the flux are now completed, and so it is possible to calculate the AMS-02 primary proton flux. The AMS-02 computed flux is displayed in 5.10 together with data from several other experiments. Since these experiments were performed under different Solar activity conditions, the low rigidity region of the flux is substantially different among them. The AMS-02 flux is "folded", i.e, the rigidity distribution of selected protons was not corrected for the effects of rigidity displacement due to the finite spectrometer resolution. For events above 50 GV, the rigidity uncertainties can result in a wrong assignment of the particle's rigidity. As a result, the slope of the proton flux, for rigidities above 50 GV, can be slightly affected.

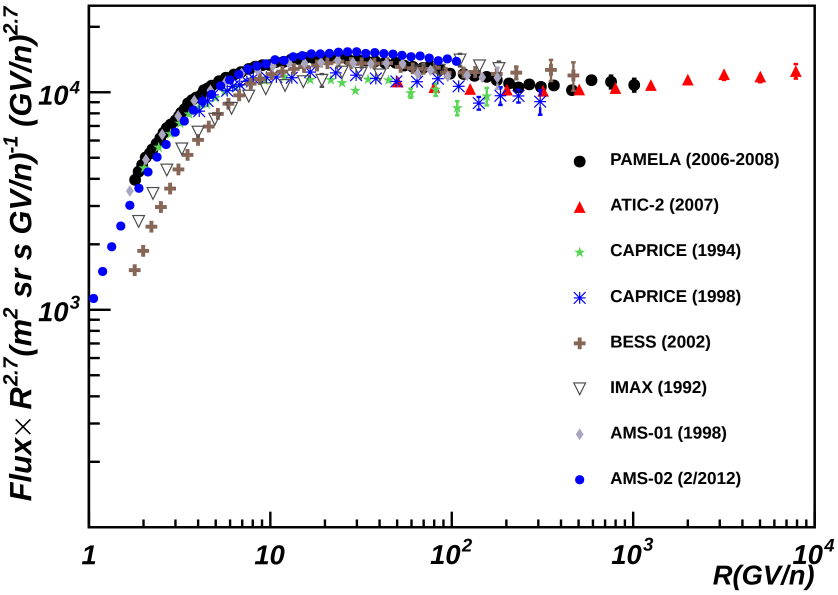

Figure 5.10: Proton flux from several experiments.

5.2 Solar effects on fluxes

This section serves the purpose of monitoring and studying the effects of the Sun on the AMS-02 primary proton flux, both the sporadic, caused by Solar Flares or CME, and the long term Solar modulation. This will be done by integrating the proton flux at low rigidities (2 to 30 GV) and high rigidities (30 - 100 GV) and studying its variations.

5.2.1 Observation of Solar Events

As described in Chapter 2, SCR or SEP, which are originated due to Solar phenomena, constitute a percentage of the total cosmic ray flux reaching Earth. The origin of these Solar particles is normally associated with events like Solar flares and CME, which also influence the flux of GCR.

Solar Flares are huge explosions on Sun's surface, usually occuring near sunspots. When the tangled magnetic fields, coming out of the surface, reach a "breaking point", like a rubber band that snaps when wound too tight, huge bursts of energy are released as the field lines reconnect. This can lead to the formation of a Solar flare, as depicted in figure 5.11.

In the magnetic reconnection process, a huge amount of magnetic energy is rapidly released and transformed to thermal and kinetic energy of the particles. Reconnection can accelerate particles to a high energy (few GeV) within a short time, as required by the very impulsive SEP events. Ejected particles may either remain trapped, or escape into the interplanetary space, if the upper magnetic configuration becomes open.

The particles emitted during these kind of events are mainly photons (γ-rays and X-rays), protons and electrons.

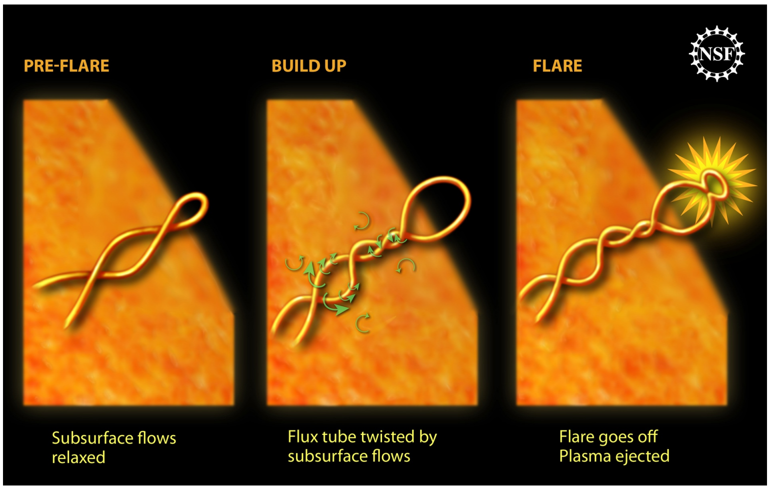

Figure 5.11: Schematic representation of the formation of a Solar flare (Credit: NSF).

Solar flares can be classified by their brightness, i. e., the peak flux (in watts per square meter, W/m^2) of 100 to 800 picometer X-rays.

Classification	peak flux (W/m^2)
X	$\geq 10^{-4}$
M	10^{-5} - 10^{-4}
C	10^{-6} - 10^{-5}
B	10^{-7} - 10^{-6}
A	$\leq 10^{-7}$

Table 5.2: Solar flares Classification

Within a class there is a linear scale from 1 to 9 (apart from X), so an M2 flare is twice as powerful as an M1 flare.

CME are quite common during periods of high Solar Activity and are characterized by being spatially larger and temporarily slower than Solar flares. During a CME, huge quantities of plasma, initially trapped in closed coronal magnetic field lines, are ejected into interplanetary space (involving typically 10^{12} to 10^{13} kg of mass, and kinetic energies of 10^{24} to 10^{25} J).

The disruption of a large, stable, magnetically closed structure still poses fundamental questions for the MHD theory. However, it is probable that large-scale magnetic reconnection is involved in the formation of a CME. It is also worth noting that, although flares and CME are often connected, this is not always true.

A CME often leads to a huge hot plasmoid (a closed magnetic structure) moving with a high speed in the interplanetary space, and to an interplanetary shock located at the front edge of the plasmoid (the shock can also accelerate particles by Fermi-acceleration).

Thus, a Solar flare or a CME can generate a shock that propagates through the Heliosphere. This shock will reduce the flux of GCR that reaches Earth, originating what is called a Forbush decrease [44]. The causes of the Forbush decrease are still not completely understood, but it is believed that the shock increases the magnetic field as it passes through the Heliosphere, creating an effective barrier for the cosmic ray particles. Usually, the shock front also "collects" and accelerates particles, which are seen as a small intensification of the flux before the Forbush decrease.

In order to monitor variations, the AMS-02 proton flux was integrated between [2 ; 30] GV, which corresponds to the rigidity zone where the flux is sensible to these kind of effects.The Oulu NM's counting rates were also analyzed.

The most intense Solar flares between 8/2011 and 4/2012 are listed in table 5.3.

Table 5.3: Solar flares' list between 8/2011 and 4/2012 [45]

Classification	Date	Sunspot Region
X6.9	August 9 2011	1263
X5.4	March 7 2012	1429
X2.1	September 6 2011	1283
X1.9	November 3 2011	1339
X1.9	September 24 2011	1302
X1.8	September 7 2011	1283
X1.7	January 27 2012	1402
X1.4	September 22 2011	1302
X1.3	March 7 2012	1429
X1.1	March 4 2012	1429
M9.3	August 4 2011	1261
M8.7	January 23 2012	1402
M8.4	March 10 2012	1429
M7.9	March 13 2012	1429

Note that the majority of these Solar flares were accompanied by a CME.

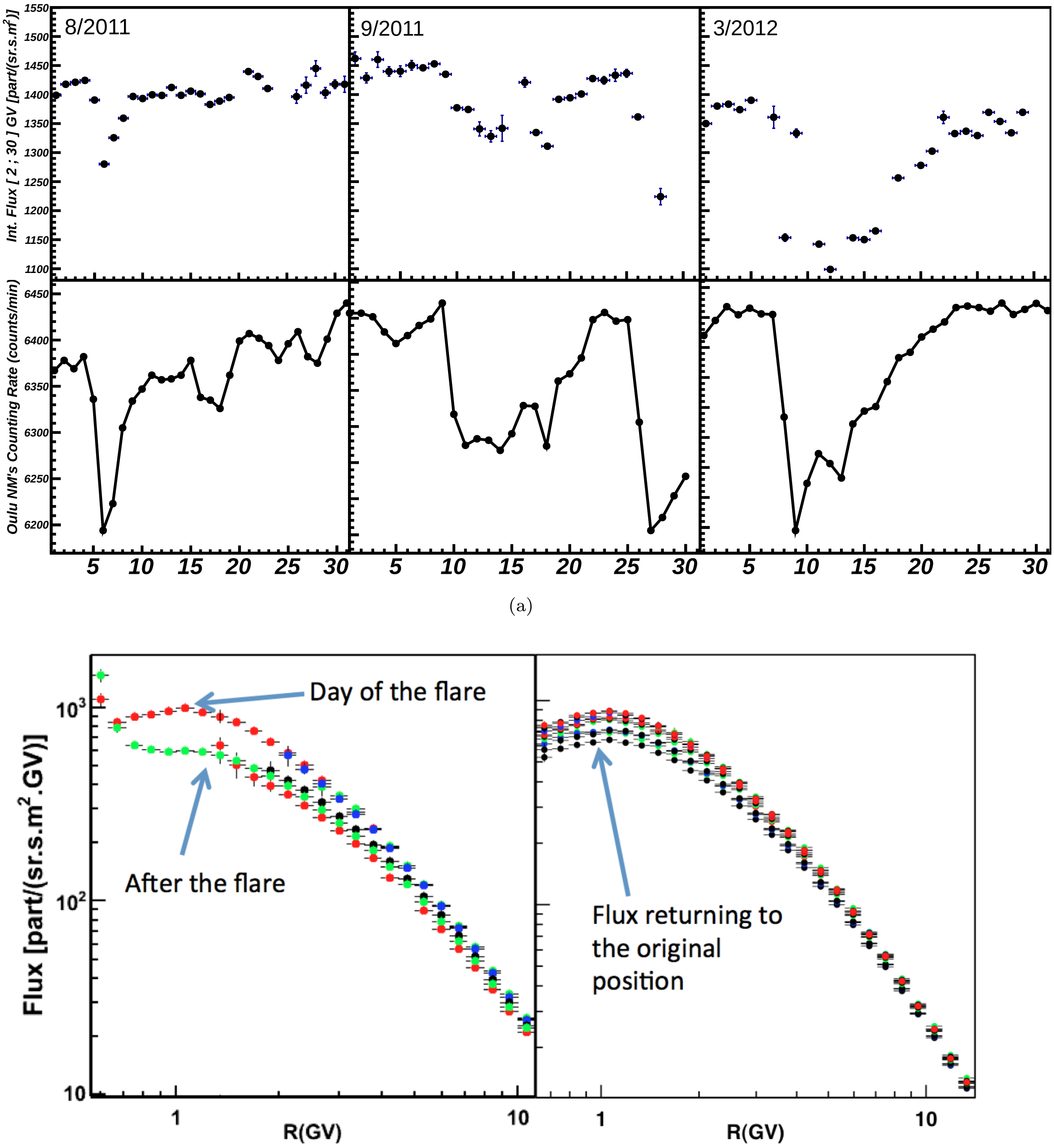

(a)

(b)

Figure 5.12: a) Integrated proton flux [2 ; 30] GV and Oulu NM's rates in a daily basis (days of the month in the X-axis), for the months with the most powerful Solar flares (August 2011 September 2011 and March 2012). The plots reveal the expected reduction of the low energy proton flux during a flare. Additionally, they show a strong temporal correlation between the variation of the integrated flux and the number of neutrons reaching Earth's surface. b) This figure shows the several phases of 7th March flare. The first one is the arrival of the SEP protons, which were accelerated in the shock front, and will increase the proton flux at low rigidities. After the passage of the shock front, there is a sudden decrease in the flux due to the enhancement of the magnetic field.Finally, the flux takes almost 20 days to return to its original form.

5.2.2 Stability of the fluxes

A detailed study of the daily integrated fluxes, at low and high energies, was performed with the AMS-02 proton data. Figure 5.13 shows the integrated fluxes for data between August 2011 and April 2012. The low energy integrated flux in 5.13(a) reveals relative flux variations up to $\sim 30\%$, due to Solar events, whereas the high energy integrated flux in 5.13(b) is stable within 2% to 3%.

In the first days of December, 6 ladders of the Tracker, measuring the X-coordinate (non bending coo.) were lost. The ladders caused a drop on the acceptance in the order of 10%. Monte Carlo proton samples are needed to accurately evaluate the new acceptance. Since no Monte Carlo was available including this effect, an average correction was applied to acceptance from December on. Nevertheless, this correction is still preliminary and more studies need to be done in order to understand all the impacts of the lost.

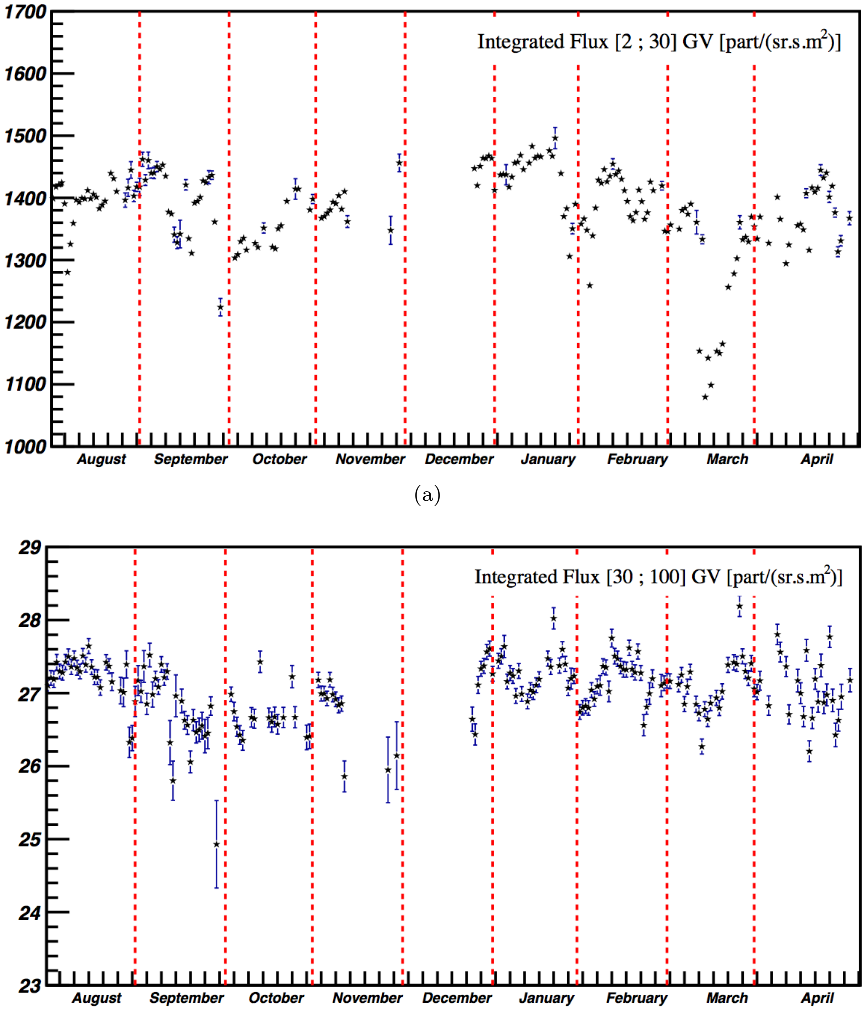

(a)

(b)

Figure 5.13: a) Integrated proton flux (low energy) between 8/2011 and 4/2012 . b) Integrated proton flux (high energy) between 8/2011 and 4/2012.

5.2.3 Solar modulation parameter analysis

The study of the Solar modulation with AMS-02 proton fluxes was done using the Force Field approximation. As seen in the last chapter, the Solar modulation parameter - ϕ_{SM} - depends on the form of the LIS used. The expression for the modulated flux in $\frac{\text{particles}}{\text{m}^2\ \text{s}\ \text{GeV}\ \text{sr}}$ is given by 4.26. However, the units of the measured flux are $\frac{\text{particles}}{\text{m}^2\ \text{s}\ \text{GV}\ \text{sr}}$ and so, expression 4.26 must be multiplied by the correspondent jacobian, in order to be dimensionally equivalent. The modulated flux per unit of rigidity is

$$J_R = J_T \frac{dT}{dR} = A \frac{R}{E} \frac{E^2 - m^2}{(E + Z\phi_{SM})^2 - m^2} J_{LIS_T} \tag{5.13}$$

where

- R is the particle rigidity in GV
- T is the kinetic energy in GeV
- E is the kinetic energy in GeV
- ϕ_{SM} is the solar modulation parameter in GV
- Z is the charge of the particle
- m is the mass of the particle in GeV
- A is a normalization constant, to account for slight variations in absolute fluxes between the observations
- J_{LIS_T} is the interstellar flux in $\frac{\text{particles}}{\text{m}^2\ \text{s}\ \text{GeV}\ \text{sr}}$

The procedure to determine the Solar modulation parameter is to fit the measured fluxes with expression 5.13. Since the fluxes under study are primary proton fluxes, some of the parameters were fixed: m = 0.938 GeV and Z = 1.

As previously discussed in section 4.5, the Force Field is a simplistic approximation that neglects some terms of the transport equation, like the drifts, and fails to estimate the correct adiabatic losses at low energies. As a consequence, there is a possibility that the Force Field is not able to reproduce the observed flux at some energy regions where this terms cannot be neglected and have an important impact on the flux. In order to detect these kind of effects, a study of the optimal fitting region, i.e., the rigidity region where the model explains the modulated flux most accurately, was done. The AMS-02 primary proton fluxes were fitted in a daily basis, between [R_{min}; 50] GV using the expression 5.13. With the daily ϕ_{SM} obtained between August 2011 and December 2011, a monthly average was calculated, and the results are shown in figure 5.14 for two different LIS models. Note that, all days corresponding to periods of Solar events (Solar flares and CME) were excluded from this analysis. During these days, the flux is deformed at low energies, influencing the value of the Solar modulation parameter. The reason to choose 50 GV and not an higher value, as the upper fitting boundary, has to do with two issues. The first one is because there is not much interest in fitting the flux at high rigidities, where the Solar modulation effects are negligible, and the event statistics is low. Secondly, because the unfolding of the flux was not performed, and so, at high rigidities, the flux may be partially distorted.

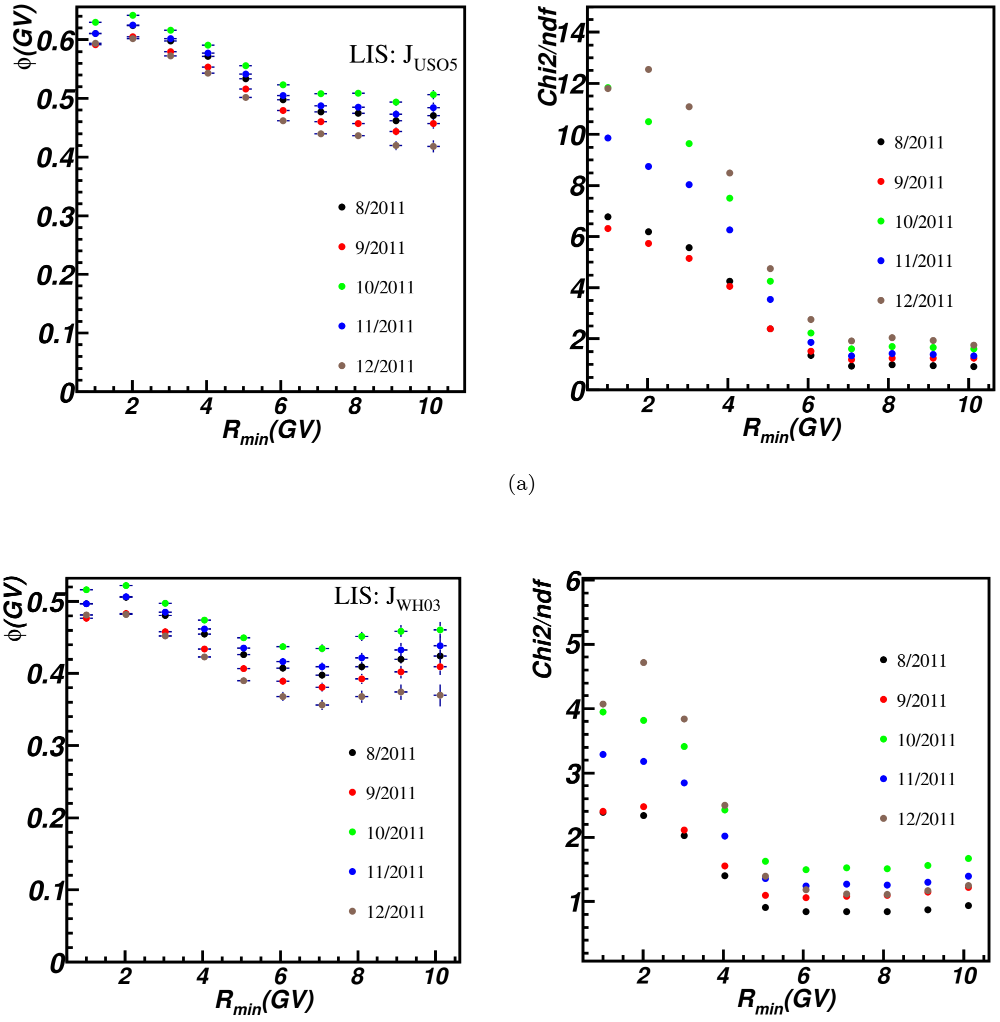

(a)

(b)

Figure 5.14: a) Monthly Solar modulation parameter between 8/2011 and 4/2012 as function of R_{min}, using the Usoskin LIS . b) Monthly Solar modulation parameter between 8/2011 and 4/2012 as function of R_{min}, using the Weber and Higbie 2003 LIS.

The plots in 5.14 show a degradation of the Force Field parameter for lower fitting boundaries below $\sim$ 6 GV. This effect is independent of the LIS model used. Additionally, the χ^2/ndf of the fit visibly degrades if $R_{min} <$ 6 GV (as can be seen in figure 5.15 for a particular day). This can indicate that the flux, for low rigidities, cannot be properly explained by the Force Field approximation. However, for rigidities above 6 GV, the Force Field is able to reproduce the corresponding modulation. With this in mind, the calculation of the AMS-02 Solar modulation parameter from August 2011 to April 2012 was performed using the J_{USO5} LIS model (figure 5.16).

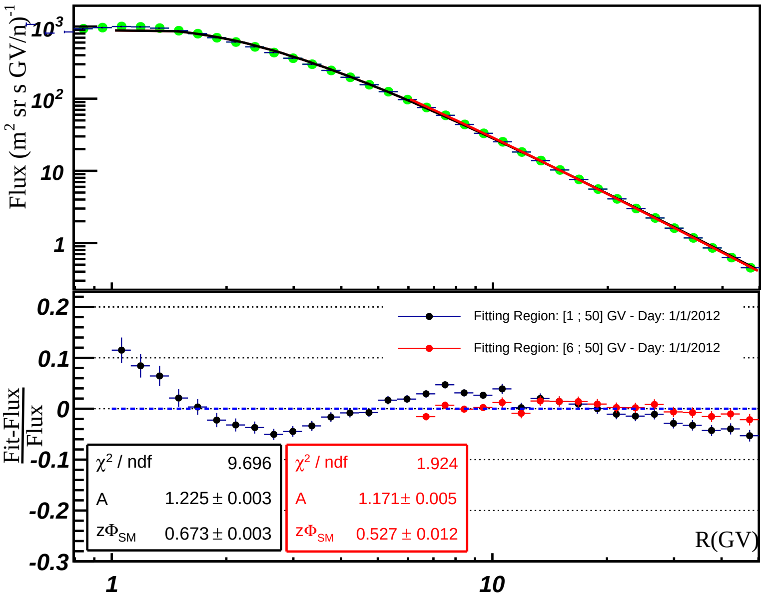

Figure 5.15: Solar modulation parameter derived from the AMS-02 proton fluxes (1^{st} January 2012) for R$_{min}$ = 1 GV and R$_{min}$ = 6GV using the J_{USO5} LIS model. As can be seen, for R$_{min}$=1 GV, the Force Field cannot fit properly the measured flux.

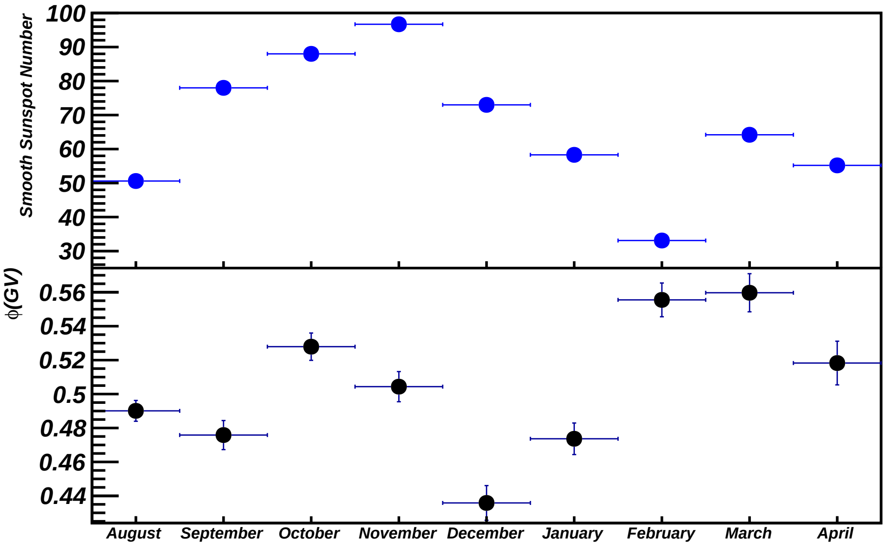

Figure 5.16: Smooth Sunspot number between August 2011 and April 2012 (SIDC Belgium).Solar modulation parameter derived from the AMS-02 proton fluxes between August 2011 and April 2012, using the J_{USO5} LIS model.

The evolution of the Solar modulation parameter from August 2011 to April 2012 (figure 5.16) does not show a specific trend, even considering that presently we are near a Solar maximum and the modulation effects are increasing very rapidly. This behavior is also present in the Sunspot number from the Solar Influences Data Analysis Center (SIDC). In fact, as can be seen in figure 2.6 that shows the solar parameter derived using NM values since 1960, data analysis of 9 months periods are sometimes insufficient to spot a general increasing or decreasing trend. As a consequence, the expected increasing tendency will only be visible with some more months of data.

5.2.4 Compatibility with NM

As mentioned before in section 2.5.1, the flux on the top of the atmosphere can be calculated using the neutron rates, and the specific yield function of each station. Given this, the Solar modulation parameter can be derived using the NM network data. The interstellar flux normally used to compute the NM's Solar modulation parameter is J_{USO5} [46]. As a result, the parameters extracted from the NM and the AMS-02 proton fluxes are directly comparable, since both used the same LIS model. Unfortunately, the NM modulation parameters for the year 2012 haven't yet been published, and the comparison can only be done with the values between August 2011 and December 2011 [50]. This comparison is shown in figure 5.17, where the dashed line is just a guiding line of slope equal to one. As can be seen, all the points, except one, have an error compatible with the line of unity slope. This proves that a relatively good agreement exists between the Solar modulation parameter derived independently from AMS-02 and NM data.

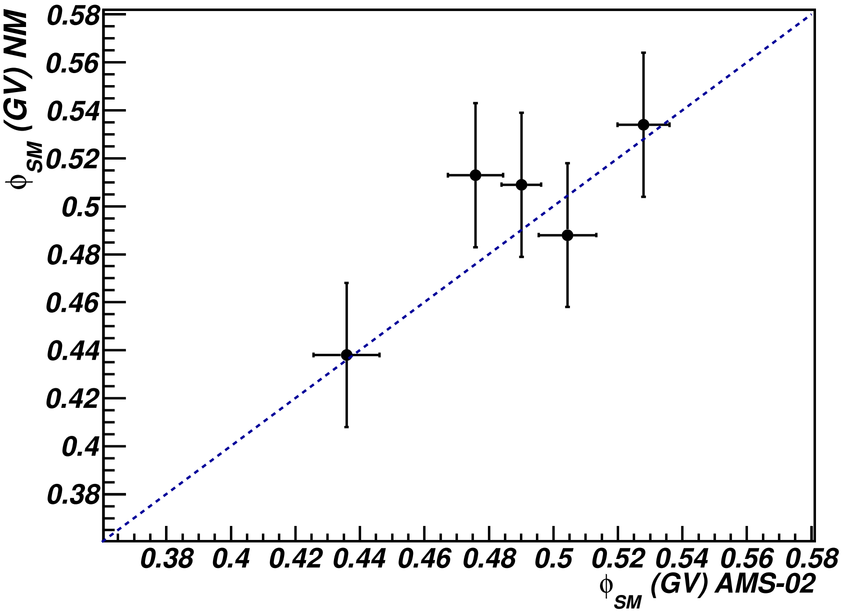

Figure 5.17: The plot shows the correlation between the Solar modulation parameter obtained from AMS-02 and the NM network. The dashed line has slope equal to 1.

Figure 5.18 shows a comparison between the NM ϕ_{SM} from August 2010 to April 2011 and the AMS-02 ϕ_{SM} from August 2011 to April 2012. Although it is not possible to see a distinctive increasing tendency in the evolution of the AMS-02 modulation parameter from August 2011 to April 2012, when compared to the values obtained from the NM network one year before, from August 2010 to April 2011, an average increase is observed.

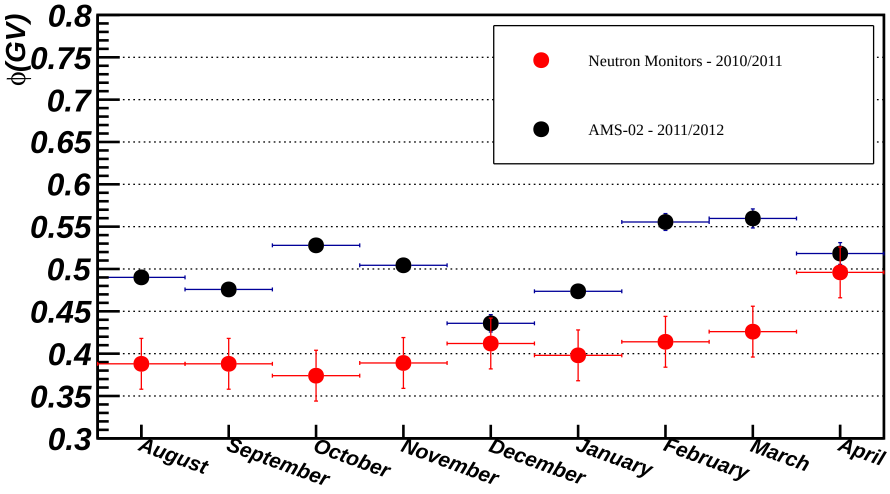

Figure 5.18: The plot shows a comparison between the NM ϕ_{SM} from August 2010 to April 2011 and the AMS-02 ϕ_{SM} from August 2011 to April 2012.

Additionally, figure 5.19 shows the correlation between the number of neutrons reaching the Oulu NM station and the low rigidity integrated proton flux, from August 2011 to April 2012. There is an evident correlation between the integrated flux and the neutron rates. The correlation factor obtained was $r = 0.79$.

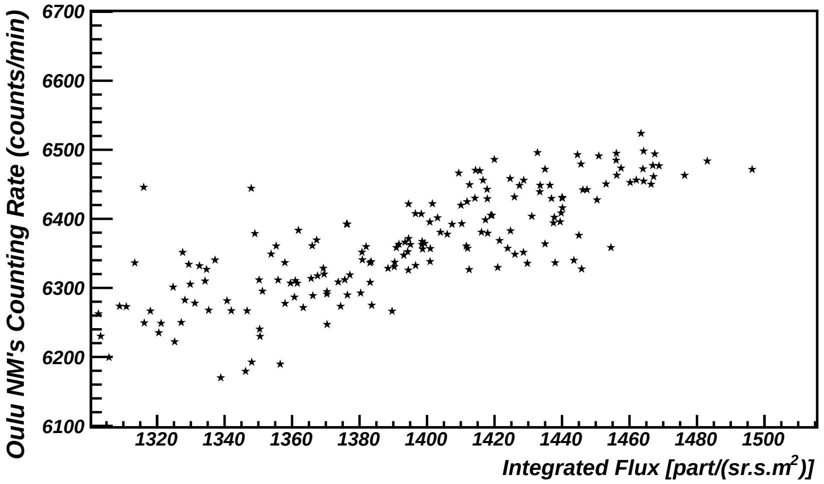

Figure 5.19: Correlation between the number of neutrons reaching the Oulu NM station and the low rigidity integrated proton flux. Each point corresponds to 1 day, beginning in August 2011 and ending in April 2012. The total number of points is 183.

6

CONCLUSIONS AND PROSPECTS

The installation of AMS on the ISS, on May 2011, constituted a milestone in cosmic rays physics. For the first time, a long term cosmic ray observatory of intermediate energies is in permanent operation in the outer space. Due to the large acceptance of the detector it is possible to collect data at an unprecedented statistical precision, which associated with the continuous operation, makes it a privileged monitor of any cosmic ray perturbation event, like a Solar occurrence.

The aim of this thesis was to study the Solar modulation models and the characterization of the effects of the Sun on the AMS-02 data. The first part of this work was dedicated to study of the several approaches to solve the TPE in the Heliosphere. Three solutions were derived: the Force Field approximation, which is the most widely used solution to study the solar modulation effects, 1D and 2D numerical solutions. All the three solutions depend on the choice of the interstellar flux. The Force Field and the 1D solution are very similar for energies above 0.1 GeV, which reduces the chances of distinguishing them using the AMS-02 proton fluxes, since the detector is not able to measure proton fluxes below 0.1 GeV. The Force Field and the 1D solution assume a spherically symmetric Heliosphere, disregarding the effects related to the drifts in the HMF and the HCS. The 2D solution is by far the most complex of the three and depends on a lot of parameters, when compared with the other two. It also takes into account the drift effects and perpendicular diffusion, which were neglected before. Numerical methods were developed to solve the 1D and 2D solutions.

The analysis of AMS-02 data was based on the measurement of the primary proton fluxes on a daily basis. The proton fluxes were determined using all the available data, since AMS-02 started collecting data last year, which is approximately 20 billion events. The variations of the integrated fluxes for low [2;30] GV and high [30;100] GV rigidities were also systematically studied. As expected, the low energy portion of the flux is sensible to Solar events, showing 20% to 30% decreases (Forbush decreases) during the most intense Solar flares. The low energy integrated proton fluxes were compared with the rate of neutrons that reach Earth's surface using the data from the Oulu NM station, and a clear correlation was found. The high energy integrated fluxes show variations of only 2% to 3%.The Force Field modulation parameter was calculated using the AMS-02 proton fluxes for all the months, between August 2011 and April 2012. For rigidities below 6 GV the Force Field parameter is consecutively degraded, as the model seems to have difficulties in fitting the observed flux. However, for rigidities above 6 GV, the model seems to fit correctly the data. The Force Field parameter, calculated using AMS-02 proton fluxes (above 6 GV), was compared with the one obtained independently from the NM network available data, and a relatively good agreement was found.

The apparent difficulty of the Force Field to fit the fluxes below 6 GV might be related to the fact that the model is neglecting terms in the transport equation that cannot be discarded, such as the drift terms. This might indicate that a more complex model, such as the 2D model, must be used in order to explain the observed fluxes below 6 GV. The complete study of the 2D model is out of the scope of this thesis. There are a lot of parameters that enter the 2D equation, which have to be carefully analyzed in order to understand its effects. However, the numerical method to solve the 2D equation, explained in chapter 3, and developed using a C++ classes framework (integrated in the analysis sofware chain - **LxSoft**), is available and can serve as a starting point to a complete data analysis using the 2D model.

BIBLIOGRAPHY

[1] Gaisser, Cosmic Rays at the Knee, p.45-55. 2007

[2] *http : //www.perdaix.de/solar_modulation*

[3] V. Formato, PhD Thesis: Measurements of p and He spectra and isotopic ratios in cosmic rays with the PAMELA experiment (2009).

[4] V. L. Ginzburg and S. I. Syrovatskii, 1964. The Origin of Cosmic Rays

[5] Zatsepin and Sokolskaya. Three component model of cosmic ray spectra from 10 GeV to 100 PeV. Astronomy and Astrophysics, **458**:1–5, October 2006.

[6] E. Fermi. On the Origin of the Cosmic Radiation. Physical Review, **75**:1169–1174, April 1949.

[7] Bell, A. R. (1978), The acceleration of cosmic rays in shock fronts. II, Monthly Notices of the Royal Astronomical Society, **182**, 443–455.

[8] Blandford, R. D., and J. P. Ostriker (1980), Supernova shock acceleration of cosmic rays in the galaxy, The Astrophysical Journal, **237**, 793–808.

[9] SIDC Belgium - *http : //sidc.oma.be/*

[10] Parker, E. N., "Dynamics of the interplanetary gas and magnetic fields," Ast- phys. J., 128, 664, 1958.

[11] http://science.nasa.gov/ssl/pad/solar/suess

[12] Jokipii, J. R., E. H. Levy, and W. B. Hubbard (1977b), Effects of particle drift on cosmic ray transport, i. general properties, application to solar modulation, APJ, **213**, 861–868.

[13] Parker, E. N., "The passage of energetic charged particles through interplanetary space" Planet. Space Sci. 1965. Vol. **13**

[14] Webb, G. M. and Gleeson, L. J. Cosmic-ray flow lines and energy changes. Astrophysics and Space Science, vol. **70**, no. 1, June 1980, p. 3-31.

[15] Forman, Jokipii and Owens. Cosmic-Ray Streaming Perpendicular to the Mean Magnetic Field. Astrophysical Journal, Vol. **192**, pp. 535-540 (1974)

[16] Forman and Jokipii.Cosmic-ray streaming perpendicular to the mean magnetic field. II - The gyrophase distribution function. Astrophysics and Space Science, vol. **53**, no. 2, Feb. 1978, p. 507-513

[17] http://hpamsmi2.mi.infn.it/∼wwwams/geo.html

[18] F.Barao "AMS a large acceptance detector on ISS" IDPASC 2010

[19] Kota and Jokipii. Effects of drift on the transport of cosmic rays. VI - A three-dimensional model including diffusion.Astrophysical Journal, Part 1, vol. **265**, Feb. 1, 1983, p. 573-581

[20] H. Moraal. Cosmic-Ray Modulation Equations. Space Science Review DOI 10.1007/s11214-011-9819-3

[21] Jokipii. Cosmic-Ray Propagation. I. Charged Particles in a Random Magnetic Field. Astrophysical Journal, vol. **146**, p.480 1966

[22] Potgieter and Le Roux. Apj **423** 817 1994

[23] W. H. Matthaeus ,G. Qin ,J. W. Bieber and G. P. Zank. Nonlinear Collisionless Perpendicular Diffusion of Charged Particles. The Astrophysical Journal, **590**:L53-L56, 2003

[24] Moraal and Potgieter. A drift model for the modulation of galactic cosmic rays. ApJ, **294**:425-440, 1985.

[25] Parker, E. N. Astrophys. J. Supp., **25**, 51, 1957.

[26] Gleeson and Axford. Astrophysics.J. **154**, 1011, 1968

[27] Gleeson, L. J., and I. A. Urch (1971), Energy losses and modulation of galactic cosmic rays, Astrophys. Space Sci., **11**, 288–308.

[28] Usoskin,Alanko,Kovaltsov and K. Mursula (2005). Heliospheric modulation of cosmic rays:Monthly reconstruction for 1951–2004, J. Geophys. Res **110** ,A12108, doi:10.1029/2005JA011250.

[29] Garcia Munoz, Mason and J. A. Simpson (1975). The anomalous 4He component in the cosmic ray spectrum at $\leq$ 50 MeV per nucleon during 1972–1974, Astrophys. J., **202**, 265–275.

[30] Webber, W. R., and P. R. Higbie (2003), Production of cosmogenic Be nuclei in the Earth's atmosphere by cosmic rays: Its dependence on solar modulation and the interstellar cosmic ray spectrum, J. Geophys. Res., **108(A9)**, 1355, doi:10.1029/2003JA009863.

[31] Langner, U. W., M. S. Potgieter, and W. R. Webber (2003), Modulation of cosmic ray protons in the heliosheath, J. Geophys. Res., **108(A10)**, 8039, doi:10.1029/2003JA009934.

[32] Webber, W. R., and P. R. Higbie (2009), Galactic propagation of cosmic ray nuclei in a model with an increasing diffusion coefficent at low rigid- ities: A comparision of the new interstellar spectra with Voyager data in the outer heliosphere, J. Geophys. Res., **114**, A02103, doi:10.1029/ 2008JA013689.

[33] Herbst and Heber.On the importance of the local interstellar spectrum for the solar modulation parameter.JGR, vol. **115**, D00I20, doi:10.1029/2009JD012557, 2010

[34] Alcaraz, J., et al. (2000b), Helium in near Earth orbit, Phys. Lett. B, 494,193.

[35] Alcaraz, J., et al. (2000a), Cosmic protons, Phys. Lett. B, 490, 27.

[36] Lapidus and Leon.Numerical solution of partial differential equations in science and engineering. Wiley 1982

[37] Webber, W. R., and J. A. Lockwood (2001), Voyager and Pioneer spacecraft measurements of cosmic ray intensities in the outer heliosphere: Toward a new paradigm for understanding the global modulation process: 1. Minimum solar modulation (1987 and 1997), J. Geophys. Res., **106**, 29,323.

[38] Caballero Lopez, R., and H. Moraal (2004), Limitations of the force field equation to describe cosmic ray modulation, J. Geophys. Res., **109**.

[39] http://www.ams02.org/multimedia/

[40] Rui Pereira. PhD Thesis. Reconstruction methods and tests of the AMS RICH detector: Sensitivity to light isotope measurements and dark matter searches. 2010

[41] Luisa Arruda. PhD Thesis. Charge and velocity reconstruction with the RICH detector of the AMS experiment: Analysis of the RICH prototype data. 2008

[42] The AMS Collaboration. AMS on ISS Construction of a particle physics detector on the International Space Station.

[43] Vainio et al. (2009). Dynamics of the earth's particle radiation environment. Space Science Reviews, **147**, 187–231.

[44] Forbush .On the Effects in Cosmic-Ray Intensity Observed During the Recent Magnetic Storm, Phys. Rev., **51**, 1108–1109, 1937.

[45] http://www.solarham.net/top10.txt

[46] Usoskin et al. Solar modulation parameter for cosmic rays since 1936 reconstructed from ground-based neutron monitors and ionization chambers. JGR **116** 2011

[47] Jokipii, J. R., and B. Thomas, Effects of drift on the transport of cosmlc rays. IV - Modulation by a wavy interplanetary current sheet. Astrophys J. **243** 1981

[48] Potgieter and Moraal. A drift model for the modulation of galactic cosmic rays. Apj, **294**, July 15, 1985

[49] Collard, Milhalov and Wolfe. JGR **87**, 2203.1982

[50] http://cosmicrays.oulu.fi/phi/Phi_mon.txt

[51] Smart and Shea. A review of geomagnetic cutoff rigidities for earth-orbiting spacecraft. Advances in Space Research **36** 2005.

A MAGNETIC FIELD FROZEN IN A PLASMA

The plasma formed by the solar wind has a high electric conductivity which allows the Solar magnetic field to be "frozen" and transported throughout the heliosphere. The goal of this section is to demonstrate how this mechanism takes place.

Considering a volume of plasma with surface area S, moving with velocity V, there are two frames

- O' - that is moving with the plasma
- O - that is fixed

Ohm's law in O' is just

$$\vec{J'} = \sigma \vec{E'} \tag{1}$$

Using Lorentz transformations, it becomes easy to calculate the electric field in the moving frame

$$\vec{E'} = \vec{E} + \vec{V} \times \vec{B} \tag{2}$$

where $\vec{V}$ is the velocity of the plasma, and so

$$\vec{J'} = \sigma(\vec{E} + \vec{V} \times \vec{B}) \Leftrightarrow \frac{\vec{J'}}{\sigma} = (\vec{E} + \vec{V} \times \vec{B}) \tag{3}$$

Since the plasma has a very high conductivity $\sigma \to \infty$, the last expression can be approximated by

$$\vec{E} = -\vec{V} \times \vec{B} \tag{4}$$

Making use of Faraday's law

$$\frac{\partial B}{\partial t} = -\nabla \times \vec{E} = \nabla \times [\vec{V} \times \vec{B}] \tag{5}$$

To fully understand the consequences of the last equation, let us look at the temporal change in the flux through a surface of the plasma.

$$\frac{d\phi}{dt} = \frac{d}{dt}\int_S \vec{B} \cdot \vec{n}\; dS = \underbrace{\int_S \frac{\partial \vec{B}}{\partial t} \cdot \vec{n}\; dS}_{\vec{B} \text{ changing over time}} + \underbrace{\int_L \vec{B} \cdot (\vec{V} \times \vec{dl})}_{\text{motion of the surface}} \tag{6}$$

where L is the boundary of S. The first term represents the variations of the magnetic field over time, and the second term is the flux changes due to the motion of the surface.

The second term can be rewritten using Stoke's theorem

$$\int_L \vec{B}\cdot(\vec{V}\times\vec{dl}) = -\int_L (\vec{B}\times\vec{V})\cdot\vec{dl} = -\int_S \nabla\times(\vec{B}\times\vec{V})\cdot\vec{n}\ dS \tag{7}$$

Finally,

$$\frac{d\phi}{dt} = \int_S \left(\frac{\partial\vec{B}}{\partial t} - \nabla\times(\vec{B}\times\vec{V})\right)\cdot\vec{n}\ dS = 0 \tag{8}$$

$$\phi = cte \tag{9}$$

The flux through the surface moving with the plasma remains constant, which implies that the magnetic field is frozen in the motion of the plasma. Figure 1 illustrates two situations where the last result can be applied.

In the first one, a plasma is created in a magnetic field (a) and so, as it begins to move, the frozen-in condition will lead to the bending of the magnetic field lines (b). In the second one, the plasma is created in a region without any magnetic field (c) and so, as it moves to a zone with a magnetic field, the field lines are repelled in order to keep the initial flux condition $\phi = 0$ (d).

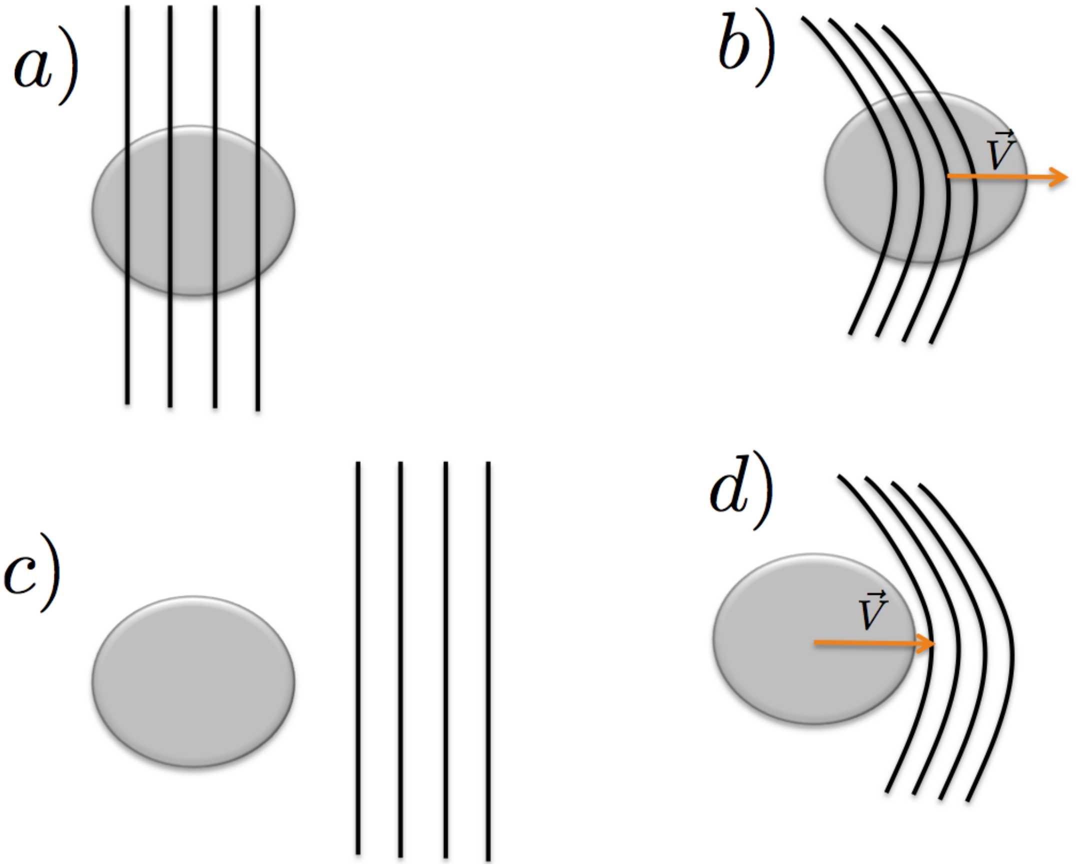

Figure 1: Plasma with high electric conductivity interacting with a magnetic field.

B THE ARCHIMEDEAN SPIRAL

The solar wind flows radially off the Sun with velocity $\vec{V}_{SW}$ as it rotates, creating a spiral pattern known as the Archimedean spiral. Considering a portion of plasma that is emitted from a point at the solar equator and with longitude ϕ_0. After a time t, the polar coordinates of the plasma portion in the rotating frame will be

$$\begin{aligned} r &= V \cdot t + r_0 && (10) \\ \phi &= \Omega \cdot t + \phi_0 && (11) \end{aligned}$$

where $\Omega = \frac{2\pi}{26}$ days^{-1} is the angular velocity of the Sun. Plugging the two last expressions it is possible to find a relation between radial distance and longitude, which characterizes an Archimedean spiral.

$$r = V \cdot \frac{\phi - \phi_0}{\Omega} + r_0 \tag{12}$$

As seen in the previous appendix, the high electric conductivity of the plasma ejected from the Sun leads to the transport of the Solar magnetic field throughout the heliosphere. In this appendix, the expression of the HMF will be derived.

Remaining still in the equatorial plane for simplicity, the velocity vector and the magnetic field only have the r and ϕ components:

$$\begin{aligned} \vec{V}_{SW} &= (V_r, 0, V_\phi) && (13) \\ \vec{B} &= (B_r, 0, B_\phi) && (14) \end{aligned}$$

Note that the components of $\vec{V}_{SW}$ are just

$$\begin{aligned} V_r &= V && (15) \\ V_\phi &= \Omega(r - r_0)\sin\theta && (16) \end{aligned}$$

The absolute value of $\vec{V}_{SW}$ and $\vec{B}$ only depends on the r and θ coordinates

$$\begin{aligned} |\vec{V}_{SW}| &= V_{SW}(r, \theta) && (17) \\ |\vec{B}| &= B(r, \theta) && (18) \end{aligned}$$

The magnetic field must also obey Maxwell's law

$$\nabla \cdot \vec{B} = 0 \tag{19}$$

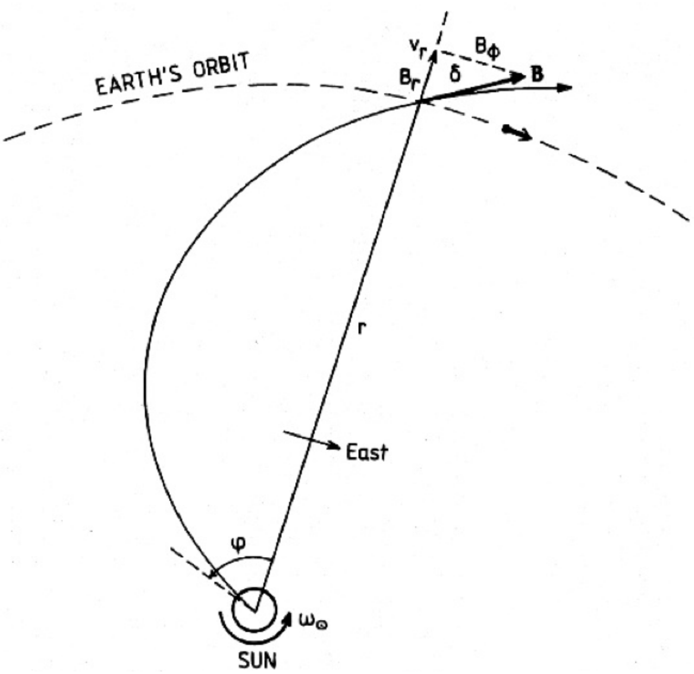

Figure 2: Archimedean Spiral.

or in spherical coordinates

$$\nabla \cdot B = \frac{1}{r^2}\frac{\partial}{\partial r}(r^2 B_r) + \frac{1}{rsin\theta}\frac{\partial}{\partial \theta}(B_\theta sin\theta) + \frac{1}{rsin\theta}\frac{\partial B_\phi}{\partial \phi} \tag{20}$$

Since the field is axially symmetric and $B_\theta = 0$, the only remaining term is

$$\frac{1}{r^2}\frac{\partial}{\partial r}(r^2 B_r) = 0 \Leftrightarrow r^2 B_r = r_0^2 B_0 = cte \tag{21}$$

Solving for B_r,

$$B_r = B_0 \left(\frac{r_0}{r}\right)^2 \tag{22}$$

In a steady flow (temporally constant)

$$\frac{\partial \vec{B}}{\partial t} = 0 \tag{23}$$

and so the frozen-in field equation attains the form

$$\nabla \times (\vec{V}_{SW} \times \vec{B}) = 0 \tag{24}$$

$$\vec{V}_{SW} \times \vec{B} = (0, V_\phi B_r - V_r B_\phi, 0) \tag{25}$$

Writing the curl in spherical coordinates

$$\frac{1}{r}\frac{\partial}{\partial r}[r(V_\phi B_r - V_r B_\phi)] = 0 \tag{26}$$

Integrating

$$r(V_\phi B_r - V_r B_\phi) = cte \tag{27}$$

Making use of the initial conditions $B_{\phi_0} = 0$ and $B_{r_0} = B_0$, the last expression can be rewritten

$$r(V_\phi B_r - V_r B_\phi) = r_0 V_{\phi_0} B_0 \tag{28}$$

The initial azimuthal velocity is just

$$V_{\phi_0} = r_0 \Omega \tag{29}$$

And so equation 28 becomes

$$r_0^2 \Omega B_0 = r V_\phi B_r - r V_r B_\phi \tag{30}$$

Solving for B_ϕ

$$B_\phi = \frac{r V_\phi B_r - r_0^2 \Omega B_0}{r V_r} = \frac{V_\phi B_r - r\Omega(\frac{r_0}{r})^2 B_0}{V_r} = \frac{V_\phi - r\Omega}{V_r} B_r \tag{31}$$

Far from the Sun $r\Omega >> V_\phi$, whence

$$B_\phi \simeq -\frac{r\Omega}{V_r} B_r = -\frac{r_0^2 \Omega}{r V_r} B_0 \tag{32}$$

Assuming that V_r is approximately constant over distance, equation 31 shows that B_ϕ decreases much slower than B_r.

$$B_\phi \propto \frac{1}{r} \tag{33}$$

$$B_r \propto \frac{1}{r^2} \tag{34}$$

Far from the Sun, the azimuthal component of the magnetic field dominates over the radial component.

Another interesting quantity to calculate is the angle Ψ, between the radial and azimuthal component of the magnetic field

$$\tan\,\Psi = \frac{r_0^2 \Omega}{r V_r} B_0 \cdot \frac{r^2}{B_0 r_0^2} = \frac{r\Omega}{V_r} \tag{35}$$

At large distances, $\tan\,\Psi \to \infty$ and $\Psi \to 90°$. At Earth, $\tan\,\Psi \simeq 1$ and $\Psi \simeq 45°$, which is in good agreement with the average observed angle.

It is also worth noting that knowing the radial dependences and average values of the several components of the magnetic field as well as the angle Ψ at Earth is sufficient to calculate the values of the HMF at any distance from the Sun.

The final expression for the HMF, also known as the Parker Field [1], is

$$\begin{aligned} \vec{B} &= \frac{A}{r^2}(\vec{e_r} - \tan\Psi\vec{e_\phi})\left[1 - 2H\left(\theta - \frac{\pi}{2}\right)\right] \\ |\vec{B}| &= \frac{A}{r^2}\sqrt{1+\tan^2\Psi}\left[1 - 2H\left(\theta - \frac{\pi}{2}\right)\right] \end{aligned} \tag{36}$$

where H is the Heaviside step function and A is a normalization constant which is choosen so that $|\vec{B}(r = r_e)|$ equals the average HMF on Earth (around 5 nT for periods of low Solar activity).

$$A = (1\text{AU})^2 \frac{B_{1AU}}{\sqrt{1+\tan^2\Psi}} \tag{37}$$

---

[1] since it was first derived by Parker in 1958